December 2021

Parametric Study of Orthogonal Pantographic Lattice with Non-Linear Torsional Resistance at Pivots

Mahendra Singh Bisht
Clemson University, mbisht@clemson.edu

PARAMETRIC STUDY OF ORTHOGONAL PANTOGRAPHIC LATTICE WITH NON-LINEAR TORSIONAL RESISTANCE AT PIVOTS

A Thesis
Presented to
the Graduate School of
Clemson University

In Partial Fulfillment
of the Requirements for the Degree
Master of Science
Mechanical Engineering

---

by
Mahendra Singh Bisht
December 2021

Accepted by:
Dr. Lonny Thompson, Committee Chair
Dr. Gang Li
Dr. Garett Pataky

ABSTRACT

Pantographic lattices are cellular solids comprised of continuous beam fibers intersecting at periodically spaced pivots. The pivots are simulated in the discrete finite element beam model as torsional springs with varied torsional stiffness across orders of magnitude. An important functional performance feature of pantographic lattices is their ability to undergo large deformation without inducing large stresses at the pivots. There is a need for predictive models of this nonlinear behavior. In this study, parameter studies on the order of magnitude and nonlinear material behavior of the torsional stiffness at the pivots, combined with and without nonlinear geometric beam kinematic behavior is investigated. In this study, the mechanical response of pantographic lattice is analyzed for a series of elongation tests based on a set of kinematic assumptions. Finite element numerical results are presented for the axial bias test for in-plane stretch along the bisector of the beam fiber orientations. Strain energy distributions are used to analyze the stiffness of the deformed geometry behavior. Geometric nonlinearity is introduced to study the response for large deformation while a non-linear torsional spring expressed as a cubic polynomial function of relative beam rotations at connection nodes is utilized to model local pivot softening and stiffening effects. One use of the discrete frame model presented in the study is to serve as a validation tool for homogenized pantographic sheet models based on second gradient field theory in the case of light spring stiffness relative to the beam lengths and section properties, of order epsilon squared, where epsilon is a small-scale parameter measuring the ratio of a repeating unit cell size to the overall lattice size. For epsilon of order one, the discrete beam model serves to validate homogenized models

based on the first gradient classical elasticity theory. The discrete beam model of an orthogonally oriented lattice is constituted by torsional springs at intersection points which dictate the internal moments. At a joint, displacements of the nodes are rigidly constrained while rotational degrees of freedom are proportional to a local torsional stiffness for the lattice pivots. The torsional stiffness of the spring is varied from (perfect) zero to infinite limits to replicate a free and rigid connection respectively between the intersecting beams joints. For the nonlinear torsional pivot spring model, the torsional stiffness is not constant, instead of being a function of the magnitude of pivot rotations. The linear torsional springs are generated at the lattice pivots in the discrete mathematical model using constraints setup using Lagrange multipliers. Geometric nonlinearity has been introduced using the large deformation beam kinematics implemented within ABAQUS finite element software. The pantographic lattice is constituted by Euler Bernoulli beams connecting nodes along the designated fibers. A nonlinear relationship between moment and angle of rotation is utilized in Abaqus python scripting to develop nonlinear torsional spring behavior at the pivots. The effective material non-linearity considered is a function of two parameters and is driven by the relative angle of rotation of two beams connecting at the pivot. A predictive model for the total energy of the lattice during a small stretch is also developed and verified in the case of the nonlinear material spring model at the pivots.

In order to help understand the effects of different aspects of nonlinearity during lattice stretch, including, deformed shape, reaction force resultant, total strain, and energy distribution, several combinations are studied; small stretch, comparing linear vs.

nonlinear torsional spring stiffness at pivots, with and without beam geometric nonlinear kinematics, and large stretch, comparing linear vs. nonlinear pivot stiffness, with and without geometric nonlinearity. The analysis has also been extended to a 3D pantographic lattice where each pivot is constituted by three torsional springs connecting the three combinations of beam fiber pairs at each intersection joint.

DEDICATION

I would like to dedicate this thesis to my family and friends, who are my best supports and constant motivation in my graduate studies.

ACKNOWLEDGEMENT

My sincere thanks to my advisor and Committee Chair Dr. Lonny Thompson, for his constant help and advice throughout my graduate study. I would like to thank my committee members Dr. Gang Li & Dr. Garrett Pataky for being part of my research committee and also helping me in this process to graduate here at Clemson University. I would also thank and acknowledge the support of Clemson University for all the resources that helped me during my learnings. I would also like to thank my colleagues and friends at Clemson University for their support and advice.

TABLE OF CONTENTS

LIST OF FIGURES

LIST OF TABLES

Chapter 1 Introduction

Periodic lattices are composed of a large number of small-sized unit cells sharing the same physical properties individually. The behavior of the lattice is dependent on the number, orientation, and size of the unit cells. Often the mechanical behavior of the unit cells is different from that of the overall lattice. Techniques have been developed to understand the micro and macro behavior of these periodic structures in simple, yet effective models. An aspect of the analysis of periodic lattice structures that is not as well understood is the correct model for the connection where the structures intersect. One objective of the present study is to verify the mechanical response of a pantographic lattice with different orders of torsional stiffness at beam intersections compared with simplified geometric linear and linear stiffness homogenized continuum models. Another objective is to generalize and predict the lattice behavior to include geometric and material stiffness nonlinearity undergoing large lattice stretch and beam deformation. To tool used for this analysis will be a discrete finite element frame model that accounts for material stiffness and geometric nonlinearities. The models and analysis will also be extended from 2D planar lattices to 3D lattices.

In the following, a literature review giving a brief overview of models developed for periodic lattice structures, and in particular, pantographic lattice structures with non-rigid beam connections is given in order to identify gaps in the literature and motivation the present study.

1.1 Literature Review

Engineering solutions have been inculcating novel design solutions by the application of heterogeneous cellular solids characterized by lightweight structures with constructions of thin-walled members with open and/or closed cellular geometry; the cells are typically ordered but can also have a more random distribution. In 3D, foams are often characterized as cellular solids. Traditional homogeneous materials often have been successfully utilized to sustainably satisfy engineering needs in the past. However, the need for nonconventional solutions often necessitates material properties that can help deliver the required response. Materials with microscopic periodic structures are one class of cellular solid materials that have a wide range of applications. In order to simplify the modeling and use continuum elasticity theories, analysis of cellular solids using various homogenization techniques has been utilized by many researchers, e.g. [1]–[3], [6]-[14].

The cellular solids studied in the work are materials with microscopic beams composed of periodic unit cells constituted by thin-walled members interconnected at edges or pivots. One of the simpler examples of these periodic lattices is honeycomb materials composed of thin-walled prismatic cells with a hexagonal shape. Figure 1-1 illustrates honeycomb and some of the other simple 2D periodic lattices that are possible.

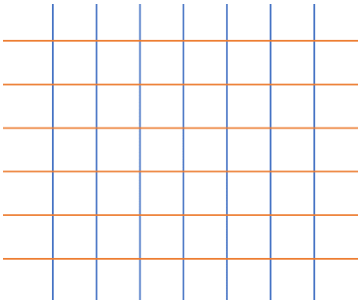

(a) Orthogonal lattice

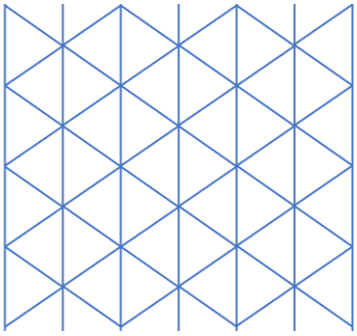

(b) Triangular lattice

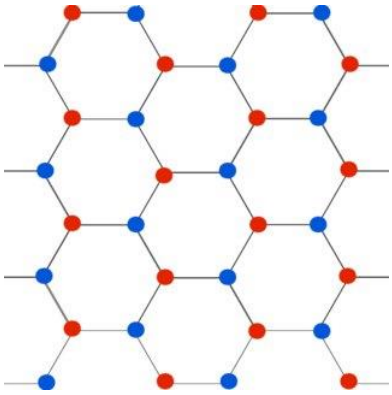

(c) Honeycomb lattice

Figure 1-1 Different periodic lattice structures

The applications of cellular materials are dependent on attributes such as geometry, size, and connection. Cellular solids are also capable of producing unconventional mechanical properties such as negative Poisson's ratio [4]. The shape of the cells can be permutated with a variety of geometric orientations to produce such different characteristic features. However, the most influential property of cellular materials is relative mass density, which is defined as the ratio of the density of the

cellular structure to the density of the material that constitutes the cell walls [5]. The relative density can be varied depending upon the material and the lattice geometry. Due to their lightweight relative density, structure cellular solids also have found applications in fields of buoyancy and thermal insulations in lightweight applications.

The mechanical behavior of the periodic lattices modeled with rigid node connections where both displacements and rotations of connected beams are assumed to be the same has been studied extensively in the literature. However, when the behavior of a material evaluated from examining the properties on a microscopic scale is significantly of a different order than the macroscopic scale, models based only on macroscale effects can diverge from the macroscopic behavior of the material under load. The heterogeneities in the material properties present in the microscopic scale often need to be homogenized or averaged accordingly to portray the macroscopic behavior accurately in a model based on a macroscopic continuum theory [1]. The heterogeneities arise due to the atypical local behavior in the microscopic scale. The macroscale properties of the lattice are not only a function of material properties, lattice size, and shape, but also depend on the local behavior of the interconnected fiber nodes at the microscale.

Homogenized models can be understood as equivalent continuum models of the periodic lattices with a large number of unit cells and hence are the approximate mathematical models. On the other hand, discrete beam frame models of the periodic lattices are highly accurate and have been successfully devised to study the elastic and plastic behavior [6] within the beams and at their connections. Discrete material models although accurate, can be computationally expensive [7], requiring large data memory

and compute times. The homogenized material model approach has made progress as these models are simpler to solve as compared to the discrete models with local heterogeneities. Consistent approximation model can be developed by introducing a small asymptotic parameter ε. The small length scale parameter, ε is the ratio of the characteristic length of the unit cell to the characteristic length of the lattice. The number of unit cells in the periodic structure dictates the length of each unit cell. For a fixed lattice size, as the number of unit cells increases, ε decreases, and as epsilon becomes smaller, in the limit $\varepsilon \to 0$, the discrete beam lattice model can be accurately replaced by the homogenized continuum model for all the points in the domain. Alternatively, ε is a parameter to visualize the separation of scales in a periodic lattice. The small-scale parameter ε has also been defined with some variations in the literature [8]–[10].

Homogenized material constitutive equations are developed by relating stress to strain to obtain relations between the microscopic parameters and the macroscopic behavior of the structure. For example, homogenized stiffness for a particular periodic domain can be obtained in terms of unit cell geometry and its parameters. Homogenization techniques can be categorized as either computational or analytical in nature. Representative Volume Element (RVE) based analysis is one of the computational-based approaches utilized to extract relations between macroscopic output behavior with the input cell boundary conditions of the RVE. RVE can be considered as the smallest volume element that can describe all the microstructural heterogeneities [1], [11]. The repetitive unit cell in a periodic lattice can be conveniently considered as an RVE. Traditional RVE methods for homogenization assume the macroscopic behavior

can be represented by classical elasticity continuum theory. However, it is possible to generalize RVE methods to generalized theories including micropolar theory.

Similarly, an asymptotic analytical method is a homogenization technique that has been utilized with variations in many works of literature for periodic beam lattices [9], [12], [13]. When the lattice cell walls are considered to be comprised of beam elements, analytical formulas can then be derived in terms of the beam material properties such as Young's Modulus, beam length, and beam section properties such as second area moment of inertia. In most of the studies found in the literature, standard beam connections are assumed rigid in nature, where the beams connecting at a node share the same bending moment and rotations.

Besides the aforementioned techniques, several other techniques exist in the literature for homogenization, e.g., the Fourier Bloch wave method, energy method, two-scale convergence method, etc. [14], [15]. Most of the RVE and these other homogenization techniques try to equate to classical elasticity theory but can also be generalized to include other continuum models such as micropolar theory.

In order to better model the section rotation of the beams, homogenization for periodic lattices using the micropolar continuum model has also been studied extensively. In [6], 2D honeycomb cell topologies are studied by equating the micropolar continuum strain energy with the strain energy from the continuum approximation of the discrete beam model, utilizing the Taylor series of a central node to connected nodes in a patch of unit cells, to obtain micropolar elastic constants for Euler Bernoulli and Timoshenko

beam models. However, the stiffness constants obtained were limited to cell geometry that allowed for only a single joint type. In [12], asymptotic homogenization was performed to obtain homogenized moduli for a micropolar equivalent continuum limited to centrosymmetric lattices subjected to bending. Homogenization techniques have also been explored for estimating mechanical properties for auxetic cellular solids, e.g. the development of a compact framework that allows for varying complexity and geometry which can also be applied for wave-propagation problems [16].

As evidenced by a wide range of literature for periodic solids, the asymptotic homogenization technique has provided reliable results for the estimation of the mechanical properties and has been considered more reliable than other techniques that rely on averaging. In the comparison of different homogenization techniques [5], relative density was used as a criterion to compare strength and stiffness properties to suggest the best homogenization technique alternatives for different cell topologies.

One of the explored periodic structures, pantographic lattices, have been studied because of their high local heterogeneity, and because the corresponding homogenized models do not fit within classical or other generalized theories such as micropolar theory. In [17], the authors describe how many of the existing cellular models capture the lattice shape deformations well but not as well in capturing the net stored elastic energy, attributing the cause to be the assumptions of beams' inextensibility in previous work. Inextensible beams fail to capture the energy stored due to the large deformations and hence require a very high-resolution small-scale model based on the first gradient approach that would be computationally very expensive. An improved approach utilizing

higher gradient theory considering torsion-free pivots to be infinitesimally small in dimensions was implemented by the authors for a planar extension bias test. Besides bending and extensional stiffness, the energy stored in these micro-pivots can be attributed to another elastic constant at the macroscale, the shear stiffness of the lattice. The study also remarks on the use of both geometric and material non-linearities concluding the inaccuracy of classical Cauchy models when non-linearities occur at microlevels. The convergence of the numerical and the experimental results confirms the confidence in the homogenization technique utilized for the large-scale non-linear beam deformations but also highlights the lack of experimental and numerical results for a variety of other tests. Research on the buckling and post-buckling phenomenon of the lattice and out-of-plane loading was presented in [18] under the assumption of pivots being able to undergo only torsional deformation. The study utilizing COMSOL Multiphysics FEA showed equivalence when the strain energy density for the beam frame model compared with the 2D continuum model developed. Similarly, a discrete model of pantographic lattices was developed to study the planar deformations and serve as a validation tool for the corresponding homogenized models [19].

In [1], the RVE of a chiral auxetic lattice was decomposed to estimate stiffness parameters based on micropolar continuum theory. The presence of rotational stiffness at the lattice joints simulated as rotational springs was studied to relate the stiffness to the auxeticity of the lattice. The study also reflects the effect of rotational stiffness was also studied on the modulus of elasticity and the Poisson's ratio of the lattice.

A 2D pantographic lattice is a periodic lattice composed of two continuous beam fibers along multiple directions; typically, the fibers are orthogonal in the undeformed configuration, but can also be skewed. Each set of fibers is connected to the other set of beam fibers through a pivot with a rotational spring connecting the rotational degrees of freedom. Figure 1-2 [20] shows a traditional pantograph hinged at the intersecting nodes by a pin that may have torsional resistance due to the presence of friction between the pin and beam holes.

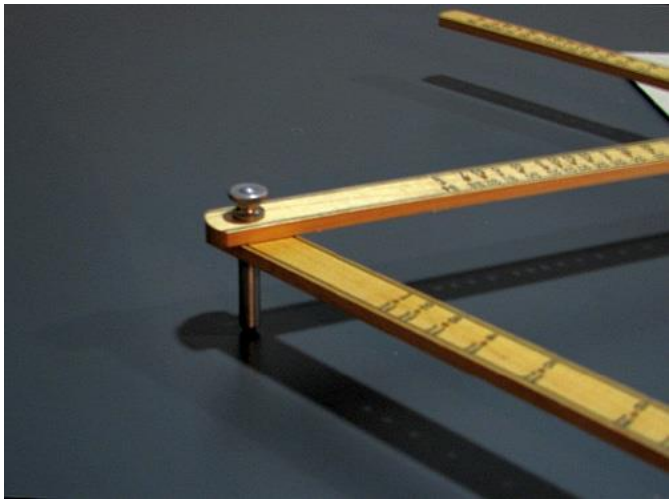

Figure 1-2 Joints of a pantograph at intersection of fibers

In the case of a frictionless pin, the pivot can be approximated as two-dimensional by assuming the rotational springs at pivots to be infinitesimally small. The nodes constituting a joint are constrained to have equal displacements. The rotational degrees of freedom of the nodes are related to the rotational stiffness of the springs. For a hypothetical spring with zero stiffness, the rotational degree of freedom of the beams at the nodes of a joint would be independent of each other. Moreover, if the nodes share

infinite rotational stiffness, the joints are assumed to be rigid in nature, sharing the same rotation. As discussed earlier, homogenized models have been developed to study large in-plane deformations for nonlinear beam models [17] of pantographic lattices assuming the limit of zero or very small torsional stiffness at the joints. These homogenized models employ second gradient (alternatively called strain gradient) theory to include local effects at the joints. For these conditions, classical and micropolar homogenized equations cannot correctly model the behavior of the lattice.

In the recent work of [8], asymptotic homogenization was used to develop a continuum model for 2D pantographic lattices with varying orders of rotational resistance for small deformation planar load. The 2D linear pantographic sheet model was studied for orthogonally oriented fibers with free rotations at the lattice joints as in [9], but now generalized to different orders of torsional stiffness at the joints. Four different cases were considered, for small torsional stiffness of order epsilon squared, where epsilon is the small asymptotic parameter measuring the ratio of cell size to lattice size, the homogenized equations are consistent with second-gradient theory, similar to [9,15]. The authors developed a formulation for dimensionless torsional resistance as the ratio of torsional stiffness of the springs to the beam stiffness. The torsional resistance for the joints is then related to the small-scale parameter ε, to generate formulation for different scales of homogeneity. By systematically increasing the pivot stiffness to order one, and higher-order, without any other assumptions on beam rotations, it is shown that the consistent equations fit within classical first-gradient elasticity theory, and in the limit of infinite torsional stiffness, asymptotes to the rigid beam connection model. Discrete

finite element based beam frame models are used and compared with experimental results reported in the literature to validate the homogenized continuum models. Although the study covers low and high order of torsional resistance, the linear model is limited to small beam deformation. The torsional springs which vary from a low order to a high order of rotational resistance are also limited to a linear mechanical response between beam node moments and rotations at pivots. In general, material behavior of the rotational resistance may be nonlinear, even under loading producing for small deformations. A nonlinear material stiffness of the torsional stiffness of the pivots has not been studied previously in the literature.

In this research, the homogenized continuum model for 2D pantographic lattice is validated by developing discrete frame linear FEM models in MATLAB and Abaqus Implicit. The 2D discrete models developed in MATLAB and Abaqus are based on Bernoulli beam theory undergoing small strains. Since the intersecting fibers constitute a joint with nonrigid behavior, the nodes are constrained to replicate the behavior of a torsional spring with a definite stiffness, k_θ. The constraints are set up utilizing Lagrange multiplier in MATLAB based discrete model. The same constraints are achieved in Abaqus Implicit using parametrized pre-existing set of PIN and spring constraints which are explained in detail in later sections. Nonlinear torsional springs with a magnitude of similar orders modeled in [8] for linear torsional springs are introduced at the lattice joints to study the material response under both small and large beam deformation under lattice elongation.

In [21], the 2D asymptotic homogenization has been extended to a 3D pantographic lattice modeled with three coincident pivots connecting the three combinations of beam rotation pairs. This linear model assumes small strains and constant torsional spring stiffness at the three pivots and has been validated with a linear discrete beam frame model using MATLAB and Lagrange multipliers to enforce constraints at the beam node connections of the lattice.

In the present work, the presented 2D discrete frame Abaqus finite element beam model is extended to a three-dimensional in Abaqus Implicit which accommodates both a linear torsional spring as well as nonlinear spring model and includes either geometrically linear beam kinematic assumption or geometrically nonlinear beam deformation. For these studies, all unidirectional beam arrays are oriented orthogonal to each other. A joint in the 3D pantographic lattice comprises of three pivot nodes, assumed coincident, from the three different continuous beam fibers intersecting at a point. Hence, a joint comprises of three torsional springs each relating a pair of beam rotations at nodes. The discrete 3D pantographic lattice model is subjected to both small and large in-plane elongation with material linear torsional springs.

As discussed in the Conclusions, the current research can be extended in the future by developing homogenized continuum models, similar to [8], [9], and elsewhere, for pantographic sheets with nonlinear torsional springs. The results produced in this research also serve as a validation tool for the homogenized continuum techniques for three-dimensional pantographic lattice models.

1.2 Motivation for Present Work and Goals

As discussed in the literature review, a variety of homogenization techniques have been utilized in the past for a range of 2D pantographic models to study the elastic properties of the lattice and develop simplified continuum models representing the discrete beam lattice. In [8] asymptotic homogenization was developed for pantographic lattices with varying order of torsional resistance at the lattice pivots and assuming linear deformation. These models were validated with discrete beam pantographic lattice finite element models subjected to linear in-plane deformations. Motivated by this work and others, there is a need to understand the behavior of pantographic lattices with variable and nonlinear torsional stiffness at pivots, combined with, and without, large deformation beam kinematics. Hence, the goals for this research are to help answer the following research questions that have not been studied sufficiently in the literature:

Question 1) How does including nonlinear geometry influence lattice behavior under the small and large deformation loads for pantographic lattice?

Question 2) What is the change to total strain energy of the lattice of altering constant spring stiffness to a nonlinear spring stiffness dependent on the angle of rotation with different orders of magnitude? Can a simple analytical model for total lattice strain energy be developed for a 3rd order polynomial nonlinear material torsional spring model?

Question 3) How much nonlinear behavior is attributed from geometric and material nonlinearity as reproduced to the global stiffness as indicated by the nonconstant slope of

the reaction force resultant to lattice elongation, and as indicated by the varying total strain energy curve from a quadratic curve in the linear case?

Question 4) How do different orders of torsional stiffness impact the global stiffness and deformation energy as studied with the geometrically nonlinear and linear geometry model, for both linear and nonlinear torsional stiffness at pivots?

Question 5) Can the 2D pantographic lattice model be extended to a similar 3D model?

1.3 Thesis Overview

Chapter 1 gives an introduction to the modeling of periodic lattices and their studies supported in the present literature. Pantographic lattices are introduced which include non-rigid beam connections.

Chapter 2 provides a descriptive model of the pantographic lattice defining the small scale parameter as the ratio of cell size to overall lattice size. The beam model and the heterogeneous behavior of the lattice pivot torsional stiffness of different orders of the small scaling parameter relative to the beam properties, and limiting cases are discussed. The general boundary conditions for the simulated elongation tests and kinematic constraints at the lattice pivots are explained.

Chapter 3 deals with linear static analysis of the discrete pantographic lattice model in 2D for small deformation and the linear torsional model relating beam moments and rotations at connecting nodes with constant torsional stiffness at different orders. The model is developed independently in MATLAB and Abaqus Standard. The chapter gives details of

the development of each model. The work also serves as a validation tool between the MATLAB model developed and the Abaqus model and also for the corresponding homogenized continuum models developed in [8] for the linear analysis.

Chapter 4 studies the nonlinear response of the 2D pantographic sheets for both small and large beam deformation. Nonlinear spring behavior is also introduced to study the nonlinear material response of the lattice pivots interacting with nonlinear geometry.

Chapter 5 further generalizes the effects of varying torsional stiffness for a discrete 3D pantographic model. The model is developed in Abaqus Standard and also implements nonlinear geometry. In the special case of linear geometry assumption, the Abaqus model is also used to verify discrete frame models coded in MATLAB and corresponding homogenized second-gradient models developed in [21] for linear analysis.

Chapter 2 Pantographic Lattice

2.1 The lattice model

Pantographic Lattices consist of a network of two or more sets of continuous beam fibers which intersect at joints called pivots. In this study, the pantographic lattice is constituted by two sets of fibers for the 2D planar model, hence each pivot is modeled with two overlapping nodes tied by constraints. The nodes compromising the pivots will always share the same translational degrees of freedom but can independent rotations. The overall mechanical behavior of the pantographic lattice depends upon the kinematic constraints applied at the pivots. To model variable pivot torsional stiffness, a varying magnitude torsional resistance between the two sets of fibers is introduced. In the limit of infinite torsional stiffness, the two coincident nodes rotate together and model a rigid connection. At the other limit of zero torsional stiffness, the beam fibers remain continuous, but now represent connections with resistance-free pivots. It is to be noted that the lattice beam material properties are isotropic in nature.

In general, the beam fibers can intersect at a variety of angles; however, in this study, the original angles prior to loading are 90 degrees representing 2D and 3D orthogonal pantographic lattice. In order to load the lattice network across the bisector of the orthogonal beam fibers, the overall lattice is oriented to an angle of 45 degrees to the horizontal axis. Essential displacement boundary conditions are established on the lattice edges for different loadings which are discussed in later sections.

The figure below shows horizontal and vertical orthogonal fiber arrays as developed in a discrete MATLAB beam model.

Figure 2-1 Horizontal and Vertical fibers overlay to constitute the pantographic lattice

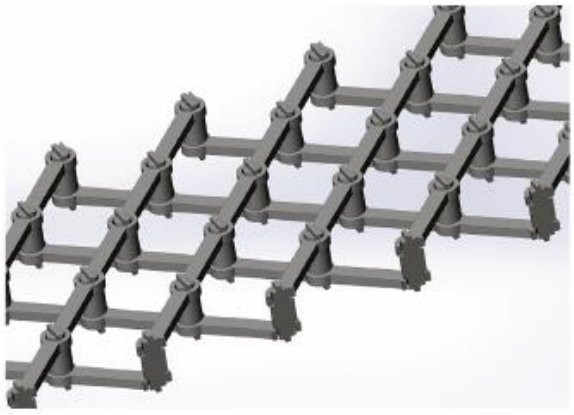

Figure 2-2 3D representation of pivots connecting the beam fibers

The pivot connections are established via various techniques in MATLAB and Abaqus Standard as will be discussed later. In general, a pivot can be considered to be comprised of a torsional spring that allows or restricts the rotational degree of freedom between two or more participating node pairs.

Using a linear assumption of small deformation and linear material properties, torsional resistance for the pivots has been studied [8] for a wide range of magnitude and can be categorized into four cases depending upon the order of the pivot torsional stiffness magnitudes, relative to the beam dimensions, material properties, and ratio of repeating unit cell size to overall lattice domain size. As discussed earlier, in [8], asymptotic homogenized models for the four cases are developed. For all the cases discussed, it is to be assumed that the beams are extensible in nature and are thin relative to their lengths such that small Bernoulli-Euler beam bending model assumptions on deformation is assumed valid. For small or zero limit torsional resistance at the pivots, it was shown that the homogenized equations fit within a generalized elasticity theory called second-order gradient or also called strain gradient theory. When the torsional resistance at pivots is increased to order one, or order one divided by epsilon squared, where epsilon is a small parameter defined by the ratio of the repeating unit cell to the larger overall lattice size, the asymptotic homogenized models fit within classical elasticity theory equations. In [cite Sai dissertation]; it is shown that when epsilon is small, corresponding to a large number of small unit cells, the homogenized models are accurate surrogate models compared to a discrete beam model of the lattice.

Following the assumption used in [8], the pantographic lattice is modeled by beams based on the Euler Bernoulli beam theory. While the beams will have a thickness that is small relative to beam length, the beam stiffness is slightly overestimated compared to Timoshenko models which also account for transverse shear deformation of the beam section or general elasticity models for the beams.

Torsional resistance as obtained from the homogenized lattice model is defined relative to the beam stiffness properties and small-scale parameter, ε.

$$K_\theta = Ebn^3 K^* \varepsilon^{2p} l^2 \tag{2.1}$$

where E is the Modulus of Elasticity, K^* is the dimensionless torsional resistance assumed order one, $n = h/l$ is the slenderness ratio of beam thickness over length, h is the in-plane beam thickness, and b is the out of plane thickness assuming a rectangular cross-section, and l is the length of the beam element between pivots. The above parameters are obtained from [8]. The beam section properties for the rectangular beams used are E = 1600 MPa, b = 1.6 mm, $n = \frac{h}{l}$ = 0.1, l = 4.95 mm, h = 0.495 mm.

In the above, p, an integer ranging from negative to positive integers, is changed to define a different order of scale epsilon. Small parameter, ε relates the characteristic length of the unit cell to that of the lattice. The figure below represents the lattice dimensions compared to that of a unit cell.

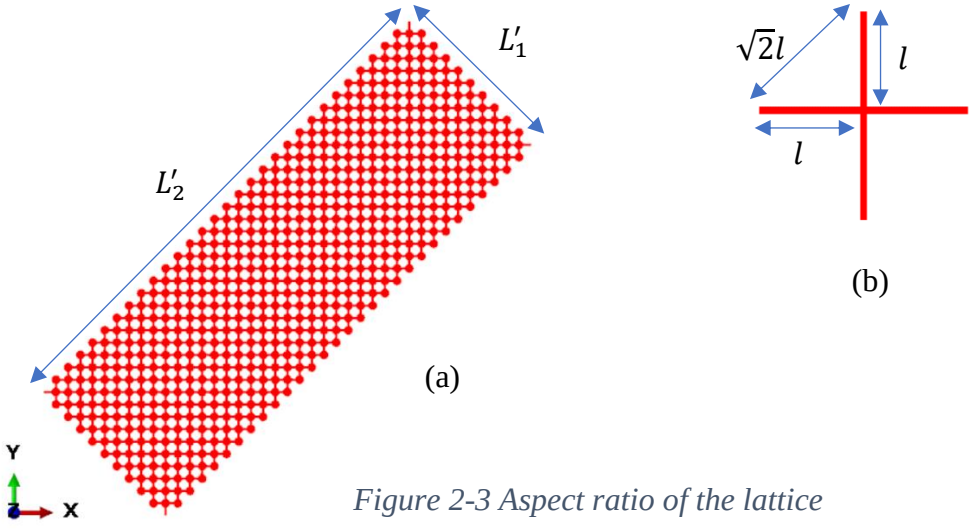

Figure 2-3 Aspect ratio of the lattice

Each side of the unit cell has a dimension of $l' = \sqrt{2}l$ units as depicted in Figure 2-3 (b). From the model dimensions of the problem considered the aspect ratio of the pantographic lattice, length: width is therefore 3:1. The lattice is $L_1' = 10\sqrt{2}l$ units wide and $L_2' = 30\sqrt{2}l$ units long. The smaller dimension $L' = \min(L_1', L_2')$ of the lattice is used as the characteristic length for defining the small parameter, $\varepsilon = \frac{l'}{L'}$

Hence for the pantographic lattice studied, the small parameter,

$$\varepsilon = \frac{l'}{L'} = \frac{\sqrt{2}l}{10\sqrt{2}l} = 0.1 \tag{2.2}$$

To estimate the behavior of the continuum model to a very fine resolution, $\varepsilon \to 0$, implying a greater number of unit cells in the same sample dimensions.

The different orders of torsional resistance can be primarily based on the parameter p from the equation (2.1); where p =1 and 0 for denoted case 2 and case 3, respectively. The 4 cases of different orders of torsional stiffness can be varied with K^*.

These cases can be described as follows:

1) For Case 1 p >1, implying the absence of any torsional resistance at the pivots signifying that the pivots do not share the rotational degree of freedom and are independent. Hence, $K_\theta \to 0$
2) Case 2 implies a low magnitude of torsional resistance at the pivots. The torsional resistance can be calculated over a range using the below formula as p =1,

$$K_\theta = Ebn^3K^*\varepsilon^2l^2 \tag{2.3}$$

For small epsilon = 0.1, the torsional stiffness is small since for this case, proportional to epsilon squared.

3) Case 3 implies a much higher magnitude of torsional resistance at the pivots. The torsional resistance can be calculated over a range of K^* of order 1, using the below formula as p = 0,

$$K_\theta = Ebn^3K^*l^2 \tag{2.4}$$

4) For Case 4, p <1 in the equation (2.1). Case 4 is of the order of $\lim_{\varepsilon\to 0}\frac{1}{\varepsilon^2}$ and thus for small epsilon, the torsional stiffness at the node connections is very large, and in the limit of epsilon tends to zero, implying an infinite torsional resistance at the pivots are constrained along the rotational degree of freedom. The pivots can be considered as a rigid joint connection. Hence, $K_\theta \to \infty$

It is to be noted that Case 1 and Case 4 are the extreme cases of Case 2 and Case 3, respectively.

2.2 Kinematic Constraints at of Pivots

The torsional resistance at pivots provides structural stiffness to the pantographic lattice. Implementation of these pivots and attributing stiffness at these joints can be achieved via a variety of means in both, MATLAB and Abaqus. As discussed earlier, a pivot is a joint at the intersection point of the orthogonal beam fibers. Each fiber node consists of three degrees of freedom (two translational DOF, and one rotational DOF). The overlapping nodes are kinematically constrained as dictated by the order of resistance that is desired to achieve. Hence these pivots constituted by 2 nodes share the translational degrees of freedom and some torsional resistance across the rotational degrees of freedom. Since our 2D model is in the x-y plane, we are concerned about rotation along the z-axis only for a planar loading.

For 3D pantographic sheets, 3 orthogonally oriented beam fibers constitute a pivot at the point of intersection. The pivot hence consists of interactions between 3 node pairs corresponding to the 3 continuous beam fibers connecting to the pivot, and each connected with a rotational spring of stiffness orders defined by the discussed four cases. In a finite element model coded in for example MATLAB, multi-point constraints can be set up for pivots using Lagrange multipliers to achieve Pin-like behavior with an added torsional stiffness element connecting coincident nodes. While the same is accomplished in Abaqus Standard commercial finite element software using a combination of MPC-Pin and spring elements.

2.3 Constraint equations at pivots

In the following a linear beam finite element stiffness model is described assuming small deformation and linear material properties to develop a finite model in MATLAB and also show the underlying equations used in a model in an Abaqus model. The MATLAB finite element model and Abaqus model will be compared in the linear analysis to validate modeling procedures.

Figure 2-4 Representation of local displacements and rotations for a 2D frame element

It is necessary to understand the 2D frame element before discussing the applied constraints at the intersection of the frame elements. A 2D frame element comprises of 2 nodes, each with 3 degrees of freedom. Hence, for each element, the six degrees of freedom (DOF) vector can be described as

$$dof = [u_1 \quad v_1 \quad \theta_{z1} \quad u_2 \quad v_2 \quad \theta_{z2}]$$

Each node has 2 translational degrees of freedom and one rotational degree of freedom. For pantographic lattices, the displacement for the overlapping nodes at each pivot is constrained as

$$u_1^1 - u_1^2 = 0$$

$$v_1^1 - v_1^2 = 0$$

In the above, the superscripts refer to the nodes from the two different beam fibers across which torsional spring is set up. The moment at the nodes at a pivot with a torsional stiffness, k_θ can be described by the following relation:

$$\begin{bmatrix} M_1 \\ M_2 \end{bmatrix} = k_\theta \begin{bmatrix} 1 & -1 \\ -1 & 1 \end{bmatrix} \begin{bmatrix} \theta_1 \\ \theta_2 \end{bmatrix} \tag{2.5}$$

For Case 1 with zero torsional resistance, $k_\theta \rightarrow 0$

Case 2 and 3 deal with some torsional resistance k_θ and Moment at the pivots can be described as

$$M = k_\theta(\theta_1 - \theta_2) = k_\theta \Delta\theta \tag{2.6}$$

For the linear models studied in [8], the torsional spring k_θ is assumed constant with changes in rotation. In this work, we will study both a linear spring k_θ, as well as a non-linear torsion spring model that changes stiffness with magnitude of beam rotation at the pivot nodes.

For Case 4 with infinite torsional resistance,

$$k_\theta \to \infty$$

Then,

$$\theta_1 - \theta_2 = \Delta\theta = 0$$

The above shows that the Case 4 limit enforces the beam nodes to rotate with the same rotation and corresponds to the rigid connections at pivots.

2.4 Boundary Conditions and loadings

The 45-degree inclined lattice is constrained to two sets of boundary conditions along its longitudinal ends. The nodes at the edge of the southwest of the lattice are rigidly constrained by fixing all 6 degrees of freedom. Meanwhile, the opposite end is subjected to a series of linearly ramped displacement loads along the longer edge of the lattice as shown in Figure 2-4. The loaded edge is represented in blue while the rigidly constrained edge is represented in red.

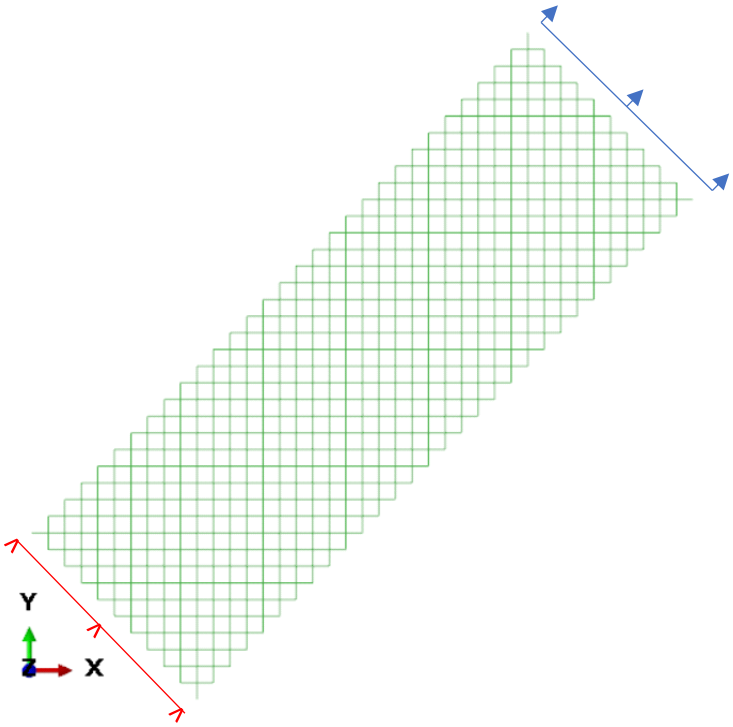

Figure 2-5 Essential boundary conditions on the edges of the lattice

The following essential boundary conditions are defined at the loaded edge,

$$u_x = d$$

$$u_y = d$$

$$u_z = 0$$

$$\theta_x = \theta_y = \theta_z = 0$$

The essential boundary conditions at the rigid ends are defined as

$$u_x = u_y = u_z = 0$$

$$\theta_x = \theta_y = \theta_z = 0$$

The applied displacement along the lattice is thus given by $\sqrt{2}d$. The essential boundary conditions at the rigid ends are defined as

$$u_x = u_y = u_z = 0$$

$$\theta_x = \theta_y = \theta_z = 0$$

The amplitude of applied stretch along the bisector of the lattice beam fibers for the overall lattice defined by the applied displacement magnitude divided by lattice length L_2' is varied according to the small and large deformation tests performed. For the linear and nonlinear analysis for 2D and 3D pantographic lattice, the lattice stretch is varied from 0.33% to 19% to observe the behavior of lattice via energy contour plots of beam strain energy distribution.

Chapter 3 Linear Static Analysis of Pantographic Sheets in 2D

The linear static analysis of the beam model is done in Abaqus and MATLAB, both the studies are utilized to validate the modeling procedures used compared with each other, and with the homogenized continuum model as in [8].

3.1 MATLAB Frame Model

Analysis of pantographic lattice consisting of orthogonally oriented fibers is performed using a 2D finite element frame model in MATLAB. Frame elements based on Euler – Bernoulli beam theory are used for the purpose; hence, the transverse shear strain is assumed to be negligible as thin beams are used. As discussed earlier, to simulate small-linear deformation, a displacement load is applied along with one of the lattice edges along the bisector of the beam fibers. The opposite edge is constrained on all six degrees of freedom in the plane.

3.1.1 Stiffness Matrix and Strain Energy

For an elastic beam model with linear deformation, strain deformation energy for each beam can be calculated as the sum of axial and flexural components,

$$\mathrm{U} = \frac{1}{2}\int_0^L EA{\varepsilon_0}^2\,dx + \int_0^L EIk^2\,dx \tag{3.1}$$

In the above, L is the beam length, and A and I are the beam section area and moment of inertia respectively, and ε_0 and k is the extension strain and bending curvature of the beams. Since the area of frame elements is considered to be constant throughout, EA and EI are constants in the above equation [22]. The stress-strain material behavior of the lattice beams is assumed to follow Hooke's law even for large lattice stretch.

The stiffness equations relating the nodal axial forces to nodal displacements for a beam are given by

$$\frac{EA}{l}\begin{bmatrix} 1 & -1 \\ -1 & 1 \end{bmatrix}\begin{pmatrix} {u_1}^e \\ {u_2}^e \end{pmatrix} = \begin{bmatrix} {F_1}^e \\ {F_2}^e \end{bmatrix} + \begin{bmatrix} {f_1}^e \\ {f_2}^e \end{bmatrix} \tag{3.2}$$

Where *l* is the element length, capital forces are internal, and small letter forces are any external applied nodal forces.

The beam bending stiffness equations for each beam element relates the nodal perpendicular displacement to the beam length dimension and rotations at nodes, related to nodal shear forces and moments.

$$\frac{EI}{l^3}\begin{bmatrix} 12 & 6l & -12 & 6l \\ 6l & 4l^2 & -6l & 2l^2 \\ -12 & -6l & 12 & -6l \\ 6l & 2l^2 & -6l & 4l^2 \end{bmatrix}\begin{Bmatrix} v_1^e \\ \theta_1^e \\ v_2^e \\ \theta_2^e \end{Bmatrix} = \begin{Bmatrix} V_1^e \\ \mathrm{M}_1^e \\ V_2^e \\ \mathrm{M}_2^e \end{Bmatrix} + \begin{Bmatrix} q_1^e \\ \mathrm{m}_1^e \\ q_2^e \\ \mathrm{m}_2^e \end{Bmatrix} \tag{3.3}$$

Combining the above two equations to form frame element stiffness relation accounting for both axial and bending stiffness defined in a local beam axis Cartesian coordinate system

$$K_f \begin{bmatrix} \frac{k_l}{K_f} & 0 & 0 & -\frac{k_l}{K_f} & 0 & 0 \\ 0 & 12 & 6l & 0 & -12 & 6l \\ 0 & 6l & 4l^2 & 0 & -6l & 2l^2 \\ -\frac{k_l}{K_f} & 0 & 0 & \frac{k_l}{K_f} & 0 & 0 \\ 0 & -12 & -6l & 0 & 12 & -6l \\ 0 & 6l & 2l^2 & 0 & -6l & 4l^2 \end{bmatrix} \begin{Bmatrix} u_1^e \\ v_1^e \\ \theta_1^e \\ u_2^e \\ v_2^e \\ \theta_2^e \end{Bmatrix} = \begin{Bmatrix} F_1^e \\ V_1^e \\ \mathrm{M}_1^e \\ F_2^e \\ V_2^e \\ \mathrm{M}_2^e \end{Bmatrix} + \begin{Bmatrix} f_1^e \\ q_1^e \\ \mathrm{m}_1^e \\ f_2^e \\ q_2^e \\ \mathrm{m}_2^e \end{Bmatrix} \quad (3.4)$$

$$K_f = \frac{EI}{l^3}$$

$$K_l = \frac{EA}{l}$$

The degree of freedom at each node can be grouped together to form the frame element stiffness relation, $K_e d_e = f_e$. In the above, K_f and K_l represents a measure of the flexural and axial stiffness of the beam element.

For our discrete beam model, we also need to consider the rotational strain energy stored in the torsional spring elements connecting the 2 nodes at the pivots. At any pivot, the fibre rotations are in general independent of each other and connected by torsional stiffness k_θ at coincident nodes in relation with the respective moment at each fiber at the coincident nodes as

$$\begin{bmatrix} M_1 \\ M_2 \end{bmatrix} = k_\theta \begin{bmatrix} 1 & -1 \\ -1 & 1 \end{bmatrix} \begin{bmatrix} \theta_1 \\ \theta_2 \end{bmatrix}$$

With a nonzero, but finite k_θ, as in Case 2 and Case 3, the total frame energy can be evaluated as a sum of strain energy stored in individual frames and the strain energy stored in the torsional springs.

$$U_{Spring} = \frac{1}{2} k_\theta (\theta_2 - \theta_1)^2$$

Summing over all frame elements, the strain energy of the beams is

$$\sum_e U^e_{frame} = \sum_e \frac{1}{2} d_e^T K^e d_e = \sum_e (U^e_{axial} + U^e_{flexural}) \tag{3.5}$$

Adding rotational spring energy for every spring element connecting coincident beam nodes at a pivot connection to obtain the new total strain energy for the deformed lattice,

$$U_{total} = \sum_e U^e_{axial} + \sum_e U^e_{flexural} + \sum_{se} U^{se}_{rotational} \tag{3.6}$$

$$U^e_{axial} = \frac{1}{2} [u_1^e \quad u_2^e] k^e_{axial} \begin{bmatrix} u_1^e \\ u_2^e \end{bmatrix} \tag{3.7}$$

$$U^e_{flexural} = \frac{1}{2} [v_1^e \quad \theta_1^e \quad v_2^e \quad \theta_2^e] k^e_{flexural} \begin{bmatrix} v_1^e \\ \theta_1^e \\ v_2^e \\ \theta_2^e \end{bmatrix} \tag{3.8}$$

$$U^{se}_{rotational} = \frac{1}{2} [\theta_1 \quad \theta_2] \begin{bmatrix} k_\theta & -k_\theta \\ -k_\theta & k_\theta \end{bmatrix} \begin{bmatrix} \theta_1 \\ \theta_2 \end{bmatrix} \tag{3.9}$$

For a constant stiffness, the total strain energy is a quadratic function of the displacements. For a linear deformation model, the beam stiffness properties are constant, hence K_l and K_f are fixed, meanwhile, k_θ varies for each case as described in Section 2.1 with order epsilon and for the different cases defined by different integer powers p. For nonlinear analysis, torsional stiffness, k_θ is defined as a function of rotation as discussed later in Section 4.2.

3.1.2 Coordinate Transformation

For the frame elements, the element stiffness equation describes the behavior of the beams in their local coordinate axes. Since the orientation of beams in the frame model is different, we need to introduce a fixed global coordinate system to assemble the stiffness equations for all the frame elements in the connected lattice.

The transformation relations from global to local coordinates are as follows for any node:

$$\begin{bmatrix} u \\ v \\ \theta \end{bmatrix} = \begin{bmatrix} \cos(\alpha_e) & \sin(\alpha_e) & 0 \\ -\sin(\alpha_e) & \cos(\alpha_e) & 0 \\ 0 & 0 & 1 \end{bmatrix} \begin{bmatrix} u_x \\ v_y \\ \theta \end{bmatrix} \tag{3.10}$$

Where alpha is the rotation angle between local and global coordinates.

Symbolically, the above matrix equation can be expressed as, $D_{local} = RD_{global}$; R being an orthogonal matrix which implies $R^{-1} = R^T$

The slope of the beam bending curve, equivalent to the section rotation θ in the Bernoulli-Euler beam model is the same in local and global coordinates for the 2D frame. Here D_{local}, R, and D_{global} represent local coordinates, transformation matrix, and global coordinates. From above, it follows taking the inverse and using the orthogonality of the coordinate rotation:

$$D_{global} = R^T D_{local}$$

Combining the above for the two end nodes for an element,

$$\begin{bmatrix} \widehat{d_1^e} \\ \widehat{d_2^e} \end{bmatrix} = \begin{bmatrix} R_e & 0 \\ 0 & R_e \end{bmatrix} \begin{Bmatrix} d_1^e \\ {d_2}^e \end{Bmatrix}$$

$$\widehat{d_1^e} = T^e d^e$$

$$d^e = T_e^T \widehat{d_1^e}$$

as T_e is also an orthogonal matrix with $T^{-1} = T^T$

Similarly, for force vector global to local transformation follows

$$\widehat{f_e} = [T_e] f_e$$

and can be reversed to local coordinates using,

$$f_e = [T_e]^T \widehat{f_e}$$

For assembly in the Global Coordinate system, the frame stiffness equations become

$$[K_e] d^e = f_e$$

Here, $[K_e] = {T_e}^T \widehat{k_e} T^e$ and $f^e = {T_e}^T \widehat{f_e}$, transform stiffness matrices and force vectors from local to global coordinates.

In 2D, since the rotation in the global z and local z directions are the same, for rotational springs at the pivots, the torsional stiffness relations at the coincident nodes relating nodal rotations for the connected beams and nodal moments are the same in both the local and global coordinate system.

3.1.3 Pin connections via Lagrange Multipliers

To establish varying torsional resistance at the pivots, Lagrange multipliers are used to set up each lattice pivot as a constraint equation enforcing that the displacements at the connected nodes are the same, but rotations at nodes can be independent. In general, for N number of nodes participating in m number of constraint equations,

$$C_{ij}d_j - Q_i = 0 \qquad\qquad i \in [1, m] \;\&\; j \in [1, N]$$

where d_j are degrees of freedom associated with nodes. For all nodes, the constraint equations can be summarized as

$$C_{(m,N)}d_{(N,1)} = Q_{(m,1)} \tag{3.11}$$

In the above relation, C is the set of constraint equation coefficients and Q is a column vector of any constants appearing in the constraint equation relations. Introducing Lagrange multipliers λ for each constraint equation as a weighting factor, the below Lagrange equation to be minimized is

$$L = \frac{1}{2}d^T K d - d^T F + \lambda^T (Cd - Q) \tag{3.12}$$

Setting the first variation of the above equation to be zero with respect to d and λ gives two coupled equation systems for displacement and Lagrange multiplier unknowns

$$L.d = \delta d^T (Kd - F) + \lambda^T (C\delta d) = 0$$

$$L.\lambda = \delta\lambda^T (Cd - Q) = 0 \tag{3.13}$$

The coupled equations for d and λ can be set up to solve in a matrix the formulation.

$$\begin{bmatrix} K & C^T \\ C & 0 \end{bmatrix} \begin{bmatrix} d \\ \lambda \end{bmatrix} = \begin{bmatrix} F \\ Q \end{bmatrix} \tag{3.14}$$

Solving the above set of equations yields displacements for the deformed geometry of the lattice frame element model with the required constraints, together with the corresponding Lagrange multipliers. For the pantographic lattice, the constraint equations enforced by the Lagrange multipliers are that the displacements are equal at coincident nodes at the beam connections. The rotational spring stiffness of the pivots is modeled in the frame stiffness using the nodal moment to rotation relations for the coincident nodes at the pivot connections. A rigid connection can be modeled with a very large rotational stiffness, in the limit enforcing the coincident node beam rotations to match. Alternatively, a rigid connection can also be enforced using Lagrange multipliers to constrain the rotational degrees of freedom at the connection nodes to be equal. Furthermore, a rigid beam connection can also be modeled directly using standard finite element beam connections with a common connecting node and stiffness assembly which implicitly assumes beam displacements and rotations are the same for all beams connecting to the shared node.

3.1.4 Numerical Results

The lattice structure was subjected to displacement loads along the XY plane on the nodes containing the top-right edge of the lattice structure as discussed in Section 2.4. The lattice was subjected to a displacement of 0.5 mm along global X and Y directions,

resulting in a net longitudinal stretch of 0.7071 mm or 0.33% stretch along the long dimension of the lattice.

$$u_x = 0.5\,mm$$

$$u_y = 0.5\,mm$$

$$u_{stretch} = \sqrt{u_x^2 + u_y^2} = \sqrt{2} * 0.5 = 0.7071mm$$

The plots below show the stretched lattice and local deformation of the lattice structure in both undeformed and deformed shapes under small stretch.

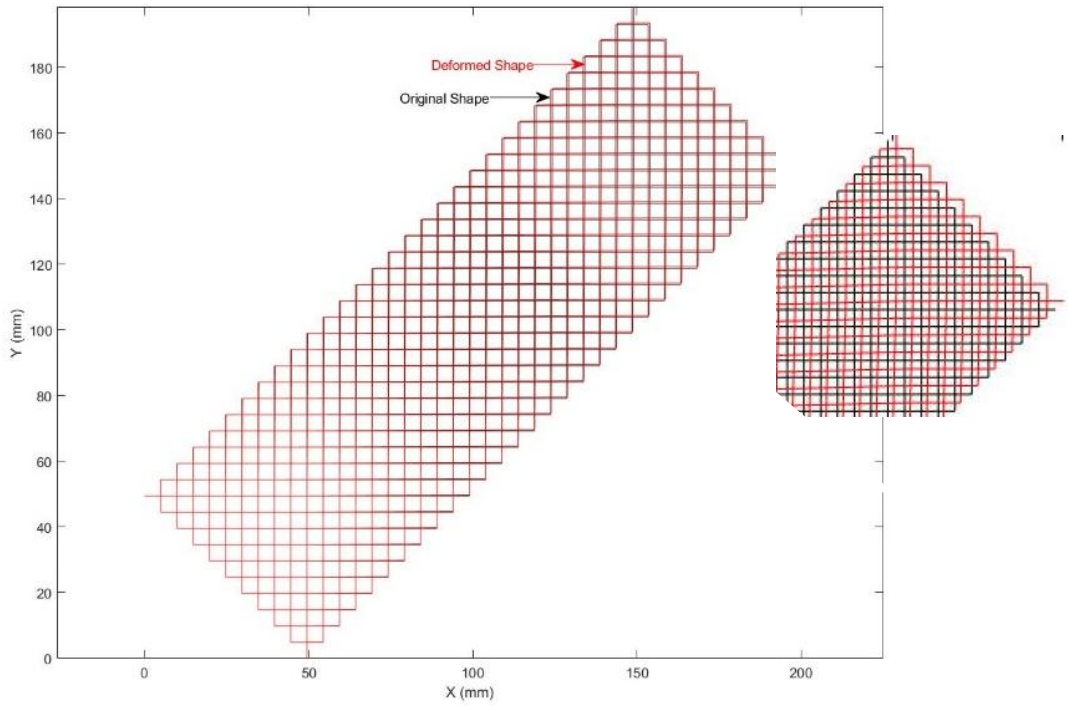

Figure 3-1 Deformed beam displacements compared to original lattice

The lattice pivots are restricted to a constant torsional resistance of different magnitude order as per the four cases previously discussed.

The deformation at each node helps to evaluate the strain energy for the lattice as formulated in Section 3.1.1. The strain energy of the beams in the lattice is plotted for the above-applied displacement for different orders of torsional resistance. The strain energy plotted in Figure 3-2 excludes the rotational strain energy and is plotted on the undeformed shape.

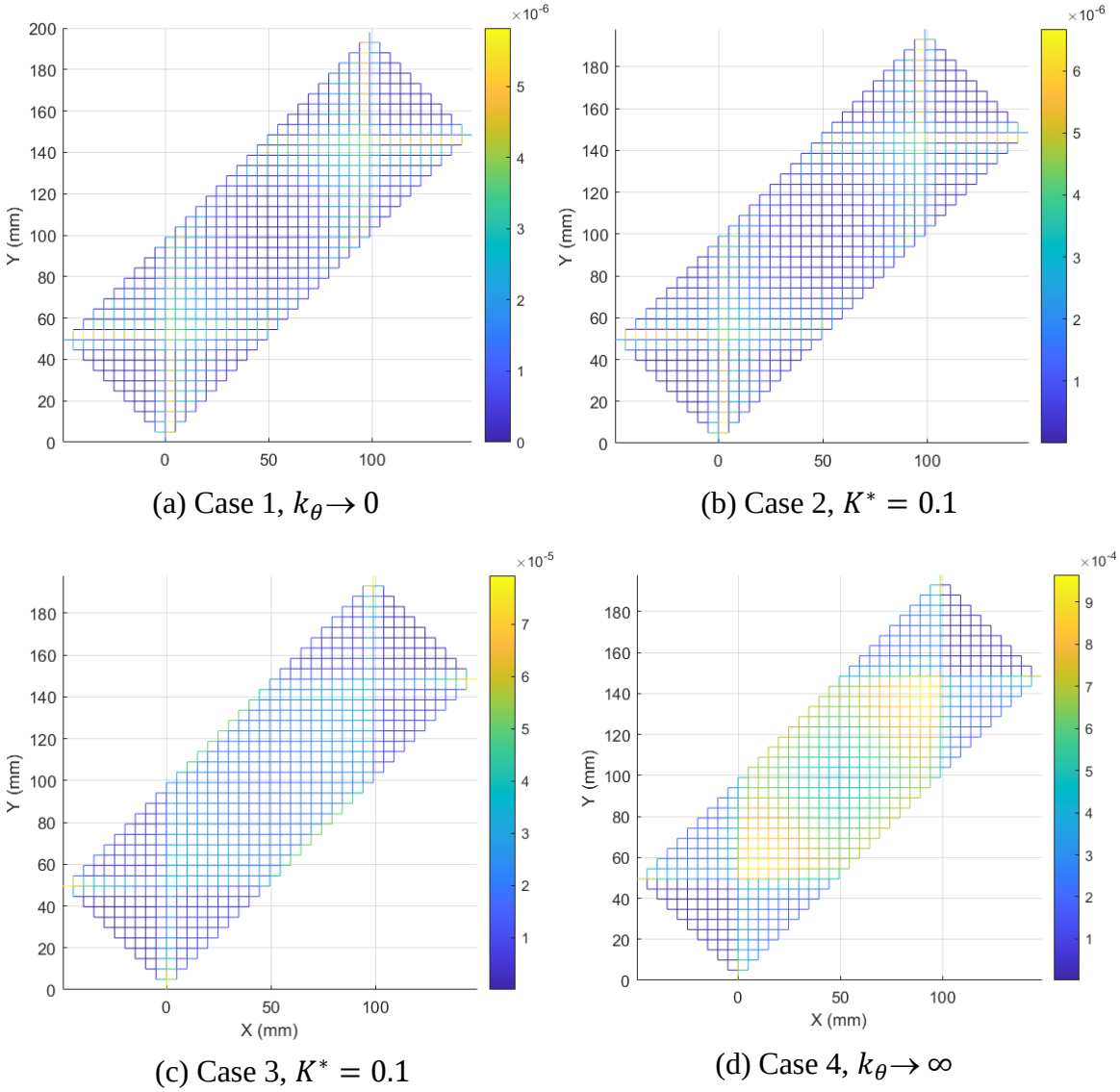

(a) Case 1, $k_\theta \to 0$ (b) Case 2, $K^* = 0.1$

(c) Case 3, $K^* = 0.1$ (d) Case 4, $k_\theta \to \infty$

Figure 3-2: Strain Energy distribution for planar extension test for the discrete MATLAB linear finite element beam lattice model (0.33% lattice stretch)

The order of torsional stiffness increases from (a) to (d) in Figure 3-2. The absolute value of torsional resistance can be calculated from equation (2.1) for Case 2 and Case 3. The torsional stiffness value for Case 1 is 0, while numerical order of 10^7 is used as torsional stiffness for Case 4 representing a near-infinite torsional resistance, corresponding to a rigid connection. The table below breaks the total strain energy into three components: beam axial and beam flexural strain energy and rotational deformation energy due to the rotational spring at the pivots.

Table 1: Total Strain Energy Components for the discrete model (0.33% lattice stretch)

	Strain Energy (mJ)			
Case	**Axial**	**Flexural**	**Rotational**	**Total**
1	4.1789e-05	0.0013	0	0.0014
2	5.3401e-05	0.0013	0.0013	0.0027
3	0.0017	0.0196	0.0774	0.0986
4	0.0210	0.5099	1.5446e-06	0.5309

The total strain energy calculated is a sum of the axial, flexural and rotational strain energy stored in the discrete lattice structure under load. These results match closely with [8] and confirm that the beam deformation energy is dominated by bending compared to axial. The rotational strain energy for Case 1 with a zero torsional stiffness is zero as $k_\theta = 0$. Both the axial and the flexural strain energy components grow with the torsional resistance. For Case 3, the rotational energy at the pivots is higher still than the

beam strain energies. For a very large stiffness value, we observed that the rotational degrees of freedom for the 2 nodes at the pivots are nearly the same as expected in a rigid connection. As a result, the rotational energy for Case 4 is nearly zero showing that the rotations of the two beams at connecting nodes are nearly the same. Figure 3-3 shows the total strain energy of the beams vs lattice stretch for Case 1. As expected for small deformation, the total strain energy is a quadratic function of the node displacements.

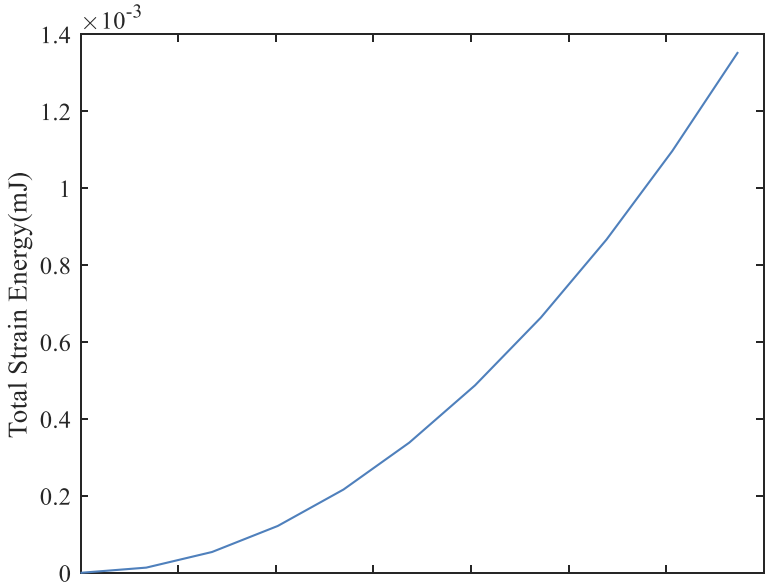

Figure 3-3 Total Strain Energy vs lattice stretch for Case 1 linear geometric model

3.2 Abaqus Model

The finite element model for the pantographic lattice is created in Abaqus Implicit 2D to validate the MATLAB discrete model. The same beam and material properties are used as discussed in Section 2.1. The figure below shows the beam profile orientation of the Euler-Bernoulli beam in the three-dimensional coordinate system.

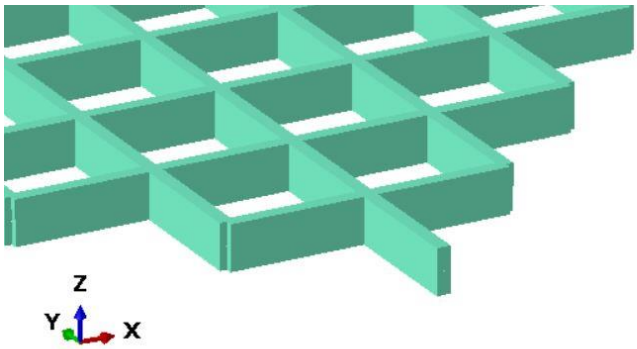

Figure 3-4 Beam profile for the 2D pantographic lattice model

The Abaqus model is developed using python scripting, while the boundary conditions are set-up in the CAE interface for the 2D model. The parametric study is conducted via python which makes it easier to study linear and nonlinear behavior of the pantographic sheets without starting simulations from the CAD model for every test. Abaqus has also been used for post-processing and visualization of the results along with MATLAB for graphing data. To construct the lattice in Abaqus CAE, two unidirectional beam arrays were created similar to Figure 2-1. Unlike MATLAB finite element program defining constraint equations and solving using Lagrange multipliers, Abaqus has convenient pre-predefined keywords for the user to establish the kinematic constraints between two overlapping nodes at a joint discussed in the next section.

Since we have not considered the effects of the transverse shear deformation and the beam's cross-sectional dimensions are small compared to the beam length, the Euler Bernoulli beam elements (B23) in Abaqus are used to be consistent with our MATLAB models [23].

3.2.1 Implementing Torsional Resistance in Abaqus

In Abaqus CAE, one can establish Pin constraints which are predefined in the graphical interface via two methods:

1) At the intersection, a *Basic* connector section in Abaqus can be used to implement a variety of combinations of predefined translatory and rotational constraints for two nodes. We have utilized the *join* type translational constraint and a *rotation* type rotational constraint. The *join* connection fixes the translational degree of freedom for the participating nodes by making the position of the second node equal to that of the first node. Meanwhile, the *rotation* connection provides a rotational connection between the two nodes. One can also define the behavior of the rotational degrees of stiffness in a Moment-rotation angle relationship within the *rotation* connection feature. The data can be input under the elasticity properties of the *rotation* connection in a table with a resolution of choice. If the relationship is not provided, the two nodes have unconstrained rotational degrees of freedom. This successfully replicates a Pin connection between two overlapping nodes with the flexibility to add rotational resistance as a relation for the *rotation* connection.

2) Similar to above, one can substitute the Basic connector with a direct Multipoint Constraint (MPC) – Pin connection which can serve the same purpose but requires a separate rotational spring definition.

   Using method 1, both a linear and nonlinear torsional spring can be implemented using the Abaqus GUI. We define a moment-rotation relationship assigned to the *rotation* connection in the basic connector pin model. The slope, K_{slope}, of the moment – rotation relation defines the rotational stiffness at the pivots and can be defined by a constant slope linear spring model or defined with a table relating moment to change in rotation angle with a nonlinear slope to model a nonlinear torsional spring. Setting up method 1 in Abaqus Python is slow. On the other hand, method 2 is time-efficient while setting up in Abaqus Python. Also, due to some computational constraints, it is time inefficient to alter the constant stiffness value of the numerous spring elements in Abaqus GUI, and hence it is advised to use spring elements only with Abaqus Python. Moreover, method 1 is easier to set up in Abaqus GUI for both linear and nonlinear torsional spring models. Considering the nature of the modeling and parametric tests eased by the use of Abaqus Python, method 2 is more convenient to model the kinematic constraints. However, method 1 yields the same results and can be used if it is more convenient based on the above discussion.

Linear and nonlinear spring can also be enacted using method 2 as previously discussed. The pin connection established via this method requires a spring element to constraint the independent rotational degrees of freedom at pivots. The *interaction*

module in Abaqus GUI allows us to implement linear springs with a definite spring constant. To attribute nonlinear behavior to the spring element, the moment-rotation relationship can be provided. However, Abaqus does not allow for nonlinear spring elements in the graphical user interface and hence, manual Abaqus input scripts have to be set up to generate nonlinear spring behavior. The Moment-rotation angle relationship used in the *rotation* connection in method 1 can be used for the spring elements in method 2 as well. For the rotational spring with a variable stiffness, Abaqus Python scripting is necessary to input the stiffness relationship.

The difference between the above two approaches is that by using a basic connector in method 1, one can easily manipulate the torsional resistance for Cases 2, 3, and 4. The kinematic equations below depict the constraints between the degree of freedom for the participating nodes.

Join Type Constraint for displacement at the pivots

$$u_1 - u_2 = 0 \qquad | \qquad v_1 - v_2 = 0$$

Rotation Type Constraint for the moment at the pivots

$$M_{rot} = K_{slope}(\theta_1 - \theta_2) = K_{slope}\Delta\theta$$

Here, the *rotation* connection is provided with a Moment – rotation ($M_{rot}\ vs\ \Delta\theta$) relationship. The slope, K_{slope}, of the relation is the rotational stiffness at the connection. Hence, we can manipulate the stiffness of the *rotation* connection to achieve the torsional resistance of different orders at the lattice pivots. For method 2, after we have established

a pin constraint between the node pairs, some definite value of torsional stiffness can be attributed to the node pairs by means of a separate spring element.

For linear analysis, the stiffness of the *rotation* connection or the spring element is constant throughout the analysis. Alternatively, to establish torsional resistance between the pivots we introduced linear spring elements with constant stiffness (k_θ) which can be varied to simulate a torsional resistance of varying orders. The linear spring can be connected to any available degree of freedom between the nodes. For the 2D pantographic lattice, the connection is made between the rotational degree of freedom for the overlapping nodes viz D.O.F. 6 in Abaqus local coordinate system.

The behavior of linear Spring Element with constant stiffness k_θ

$$M = k_\theta \Delta\theta$$

For $k_\theta = 0$, the free torsional spring model resembles Case 1, meanwhile a lattice with a very large k_θ approximates the infinite limit of Case 4.

Even though both the options are feasible, we have utilized method 1 for Abaqus simulations because of the easiness of setup Pin constraints and vary the torsional spring stiffness to achieve linear and nonlinear response at the pivots. For a 3D model, it is not feasible to create required connections manually hence Python has been extensively used. This makes any method more inclined towards scripting more feasible to make CAD, boundary conditions, and model lattice parameters.

3.2.2 Numerical Results

The MATLAB frame model was verified with the Abaqus model discussed in the previous sections of this chapter. The strain energy contours for small deformation for the linear geometric model are presented below. The contours presented in Figure 3-5 show the total strain energy in the elements. The finite element mesh has one Euler-Bernoulli beam element between each node along the fiber directions.

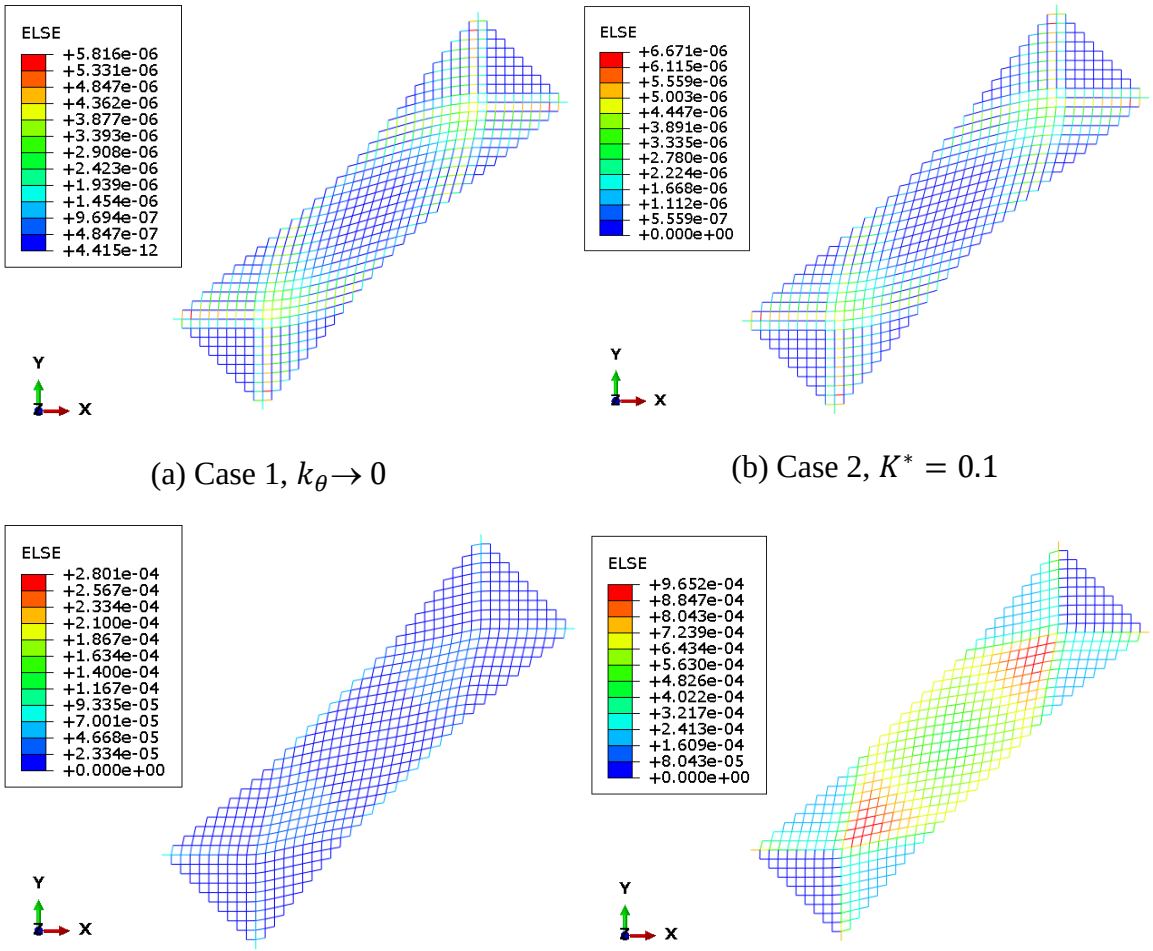

(a) Case 1, $k_\theta \to 0$

(b) Case 2, $K^* = 0.1$

(c) Case 3, $K^* = 0.1$

(d) Case 4, $k_\theta \to \infty$

Figure 3-5 Total Strain Energy Distribution for the bias extension test (small deformation)

The contours have a deformation amplification of 40 for better visualizations. The table below provides an overview of total strain energy as calculated from Abaqus Standard.

Table 2 Comparison of Total Strain Energy for the discrete models

	Total Strain Energy (mJ)	
Case	**Abaqus Model**	**MATLAB Model**
1	0.00135395	0.00135395
2	0.00268078	0.00268077
3	0.098635	0.098635
4	0.530872	0.530872

The total elastic strain energy calculated from both the models is very similar and matches up to the 7 decimal places. This validates the Abaqus model developed under a specific set of constraints as discussed in section 3.1.3 to replicate the pivots constituted by torsional springs. The outcome of both the methods in section 3.1.3 was verified to be the same. The strain energy contours show the strain energy of each element in the visualized deformed geometry with the necking behavior. It is evident that the necking behavior is less pronounced when the stiffness at the pivots increase and the lattice approaches the rigid case scenario. Figure 3-5a shows the presence of high strain energy concentration in a sequence of bands that develop around two foci. The maximum energy is found to be aligned along the diagonals of the lattice for low orders of torsional stiffness. As the strain energy of each element increases in magnitude, the energy bands

diffuse from strict boundaries to a more homogenized distribution of bands, Fig 3-5b. The larger order of torsional stiffness has elements with higher strain energy along the edges of the lattice where necking is dominant. Pockets of high strain energy region are amplified as the stiffness is further increased to achieve the case 4 rigid lattice. The strain energy distribution for case 3 and case 4 is similar but the varies a lot in magnitude. It is evident that even for the higher orders of stiffness, the total strain energy can be decreased significantly by introducing some rotational mobility to the rigid lattice.

Chapter 4 Nonlinear Static Analysis of Pantographic Sheets in 2D

For loads that produce large deformations, the stiffness of the beam lattice changes with changes in geometry. In this case, geometric nonlinear analysis is needed in which the beams undergo large strains. Materials tend to deviate from perfectly linear behavior because of inherent geometric and material responses. Hence, a nonlinear analysis is beneficial in describing the nonlinear force-displacement relations. A nonlinear analysis allows for the accommodation of smaller strains to be captured leading to more accurate models. In other terms, a nonlinear analysis accounts for a non-constant stiffness matrix for the material.

Necking in the pantographic lattice is a very common phenomenon significantly observable at higher strains. Such a geometric behavior can play a significant role in determining potential horizons for the application of similar models. Even based on the current applications of pantographic lattice models, a study of nonlinear deformation is needed to evaluate the changes in geometry and the strain energy bands. developed under large lattice stretch. In this Chapter, the nonlinear behavior of the pantographic lattice is analyzed in Abaqus Implicit.

4.1 Types of Nonlinearities

In general, there exist three major types of nonlinearities in mechanical systems: Geometric Nonlinearity, Material Nonlinearity, and Contact Nonlinearity. In this study, the pantographic sheet is studied for geometric and material nonlinearity of the beam joint connections through nonlinear rotational spring stiffness.

Geometric nonlinearity can be attributed to a nonlinear change in structure geometry during the application of load usually resulting from large deformations. This could be a result of large displacements or rotations. Material nonlinearity due to the nonlinear torsional spring at the pivot can be attributed to a nonlinear stress-strain relation from deformation history, physical factors, or a varying rate of deformation.

Geometric Nonlinearity can be established in Abaqus by toggling 'NLGEOM' (nonlinear geometry) ON for the required steps in Abaqus GUI. Material Nonlinearity from the torsional spring behavior in Abaqus can be implemented via a non-linear response to the moment-beam rotation relationship as discussed below. We have utilized a moment-theta relation to establishing the non-linear behavior. The tabular data of moment as a function of the difference in angle of rotation ($\Delta\theta = \theta_2 - \theta_1$), at the beam connection pivot is based on the following cubic function:

$$M = f(\Delta\theta) = k_\theta \Delta\theta + \gamma\Delta\theta^3 \tag{4.1}$$

In the above, k_θ, is the linear torsional spring constant, and γ is a parameter that controls the amount of nonlinearity for the torsional spring. For

$\gamma > 0$: Stiffening Behavior

$\gamma < 0$: Softening Behavior

Figure 4.1 shows an illustration of stiffening, $\gamma > 0$, and softening behavior, $\gamma < 0$. The above equation can also be rewritten as

$$M = k_\theta(\Delta\theta + \frac{\gamma}{K_\theta}\Delta\theta^3)$$

Here, we introduce the parameter β, a measure of nonlinearity of the torsional springs relative to the constant spring stiffness. Define,

$$\beta = \frac{\gamma}{k_\theta}$$

such that,

$$M = k_\theta \, (\Delta\theta + \beta\Delta\theta^3) \tag{4.2}$$

For a material following the above relation the stored strain energy for the nonlinear spring can be expressed in even powers in the relative beam node rotation at the joint

$$E = k_\theta \, (\frac{1}{2}\Delta\theta^2 + \frac{1}{4}\beta\Delta\theta^4) \tag{4.3}$$

Hence, using the above nonlinear spring model, the energy stored will always be positive for a positive β since $k_\theta \geq 0$ is also positive. This nature of the equation puts limitations on a minimum allowable value of β as energy has to be positive. Hence,

$$E \geq 0$$

$$\frac{E}{K_\theta} \geq 0$$

$$\Delta\theta^2(2 + \beta\Delta\theta^2) \geq 0$$

$$\beta \geq -\frac{2}{\Delta\theta^2} \tag{4.4}$$

Since $\Delta\theta^2 \geq 0$ for all positive numbers, β is limited for the softening case. Note that the magnitude of $\Delta\theta$ increases for increasing deformation, hence minimum β is directly constrained by the applied stretch in an inverse relation to $\Delta\theta^2$.

For $\beta = 0$, the original equation defining the linear relationship between moment and change in angle of rotation is retrieved for the case of constant torsional spring constant k_θ.

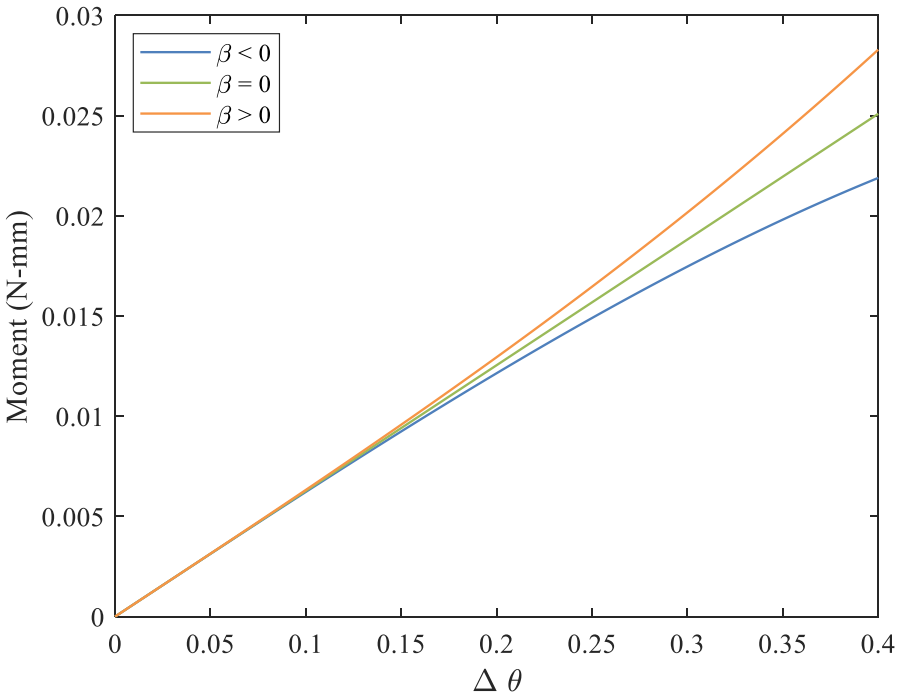

Figure 4-1 Stiffening and softening of rotational spring

The torsional spring model is implemented in Abaqus using method 1 discusses in Section 3.2.1. The Moment-rotation relation is utilized to provide nonlinear spring behavior at the pivots. It is to be noted that nonlinear spring behavior cannot be implemented from Abaqus GUI and hence Abaqus Python is used to achieve the nonlinear spring behavior. In Abaqus Python, type Spring2 is used with the Moment - rotation relationship table generated via MATLAB using the equation (4.2).

4.2 Nonlinearity and Cases Studied

The parameter β plays an important role in determining the non-linear behavior of the lattice pivots relative to the spring constant k_θ. As discussed earlier, depending upon the permissible $\Delta\theta$, the lower limit of β is restricted in each case, while the upper limit is unconstrained. This limits our exploration for softening cases to only small lattice stretch.

In the previous chapters, the deformations for small lattice stretch with linear geometry were studied. In this chapter, using the same lattice geometry and boundary condition setup, large displacement loads are applied to produce large lattice stretch and compared with linear and nonlinear geometry models. First, the lattice model with a low order of torsional resistance, or order ε^2 and high order of torsional resistance, or order ε^{-2}, respectively labeled as Case 2 and Case 3, with a non-dimensional torsional resistance of $K^* = 0.1$ are subjected to a displacement load of 40 mm for large lattice deformation. The nonlinear geometry is toggled in Abaqus Standard to test both, linear small strain beam deformation assumptions, compared to nonlinear geometric

assumptions with large beam strain assumptions. With the displacement load of 40 mm, the lattice reaches a maximum 19% stretch along the loaded edge under the same set of boundary conditions as discussed in Section 2.4.

The linear and nonlinear geometric models are studied for the response to the elongation bias test for stiffening, $\beta > 0$, and softening, $\beta < 0$, responses when the material nonlinearity of the pivot torsional stiffness is introduced. Results will also be compared with the torsional spring model with $\beta = 0$, where the moment-rotation relationship becomes linear with constant stiffness and such that the lattice is devoid of material nonlinearity. These conditions for the torsional spring are established within Abaqus using a Pin connection in combination with a rotational spring element of varying stiffness k_θ which varies as per equation 4.2.

4.2.1 Cases Studied

The different combinations of geometric and torsion spring material nonlinearity studied are summarized in the following. The simulations are carried out for the combinations of geometric and material nonlinearity outlined in Table 3. Case 2 and Case 3 represent the small and large orders of torsional resistance respectively. Case 1 and Case 4 are the limits for the small and large order torsional resistance respectively.

Table 3 Test cases for combinations of geometric and torsional spring material nonlinearity

Combination		Geometric Nonlinearity	Pivot Torsional Spring Material Nonlinearity
1	Case 1, 2, 3, and 4	No	No
2	Case 1, 2, 3, and 4	Yes	No
3	Case 2 and Case 3	No	Yes
4	Case 2 and Case 3	Yes	Yes

Same as in the previous chapter, tests performed for Case 2 and Case 3 have the nondimensional torsional resistance, K^* = 0.1 with the beam parameters defining the torsional stiffness k_θ. Combination 1 in table 3 is studied in Chapter 3 for small lattice stretch while combination 2 is presented in section 4.4. For Cases 2 and 3, nonlinear behavior due the material nonlinearity is defined by the nonlinear Moment-Rotational Displacement relation of the torsional springs which can also be expressed in terms of a nonlinear spring function,

$$M = K(\Delta\theta) * \Delta\theta = (k_\theta + \gamma\Delta\theta^2) * \Delta\theta \tag{4.5}$$

Here, $K(\Delta\theta)$ is the nonlinear function of $\Delta\theta$.

For Case 1 and Case 4, the torsional stiffness limits to, $k_\theta \to 0$ and $k_\theta \to \infty$, respectively.

4.3 Magnitude of Stretch Studied

The numerical results below discuss the strain energy contours for large deformation comparing analysis with linear and nonlinear geometry. A series of tests were performed for total longitudinal displacements of

$$u_{stretch} = [\frac{1}{\sqrt{2}}, \quad 5, \quad 10, \quad 20, \quad 40]$$

The displacements are presented in mm.

To observe the small stretch, $u_{stretch} = \frac{1}{\sqrt{2}}$ mm is used which corresponds to 0.33% lattice stretch, same as discussed in the previous chapter. To observe the pronounced large deformation effects the longitudinal strain is chosen to be around 19%. The lattice was subjected to a displacement of $20\sqrt{2}$ mm along global X and Y directions, resulting in a net longitudinal displacement of around 40 mm or19% stretch.

$$u_x = 20\sqrt{2}\, mm$$

$$u_y = 20\sqrt{2}\, mm$$

$$u_{stretch} = \sqrt{u_x^2 + u_y^2} = 40mm$$

The physical beam parameters used for large deformation elongation tests are the same as those used for small deformation.

4.4 Linear Spring with Large Stretch

In this section, results are presented for the linear and nonlinear geometry tests for 19% lattice stretch performed with linear rotational springs connected at the lattice pivots.

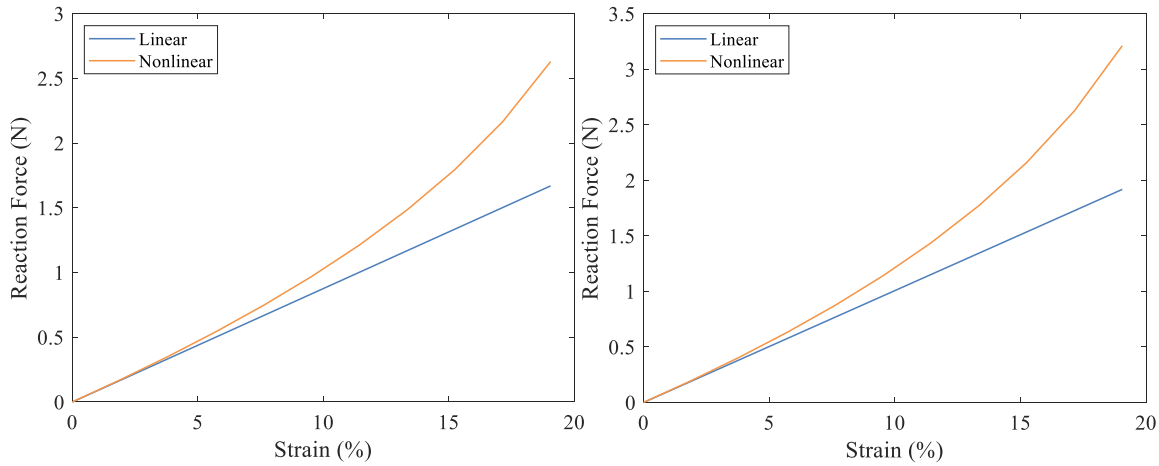

(a) Case 1, $k_\theta \rightarrow 0$ (b) Case 2, K* =0.1

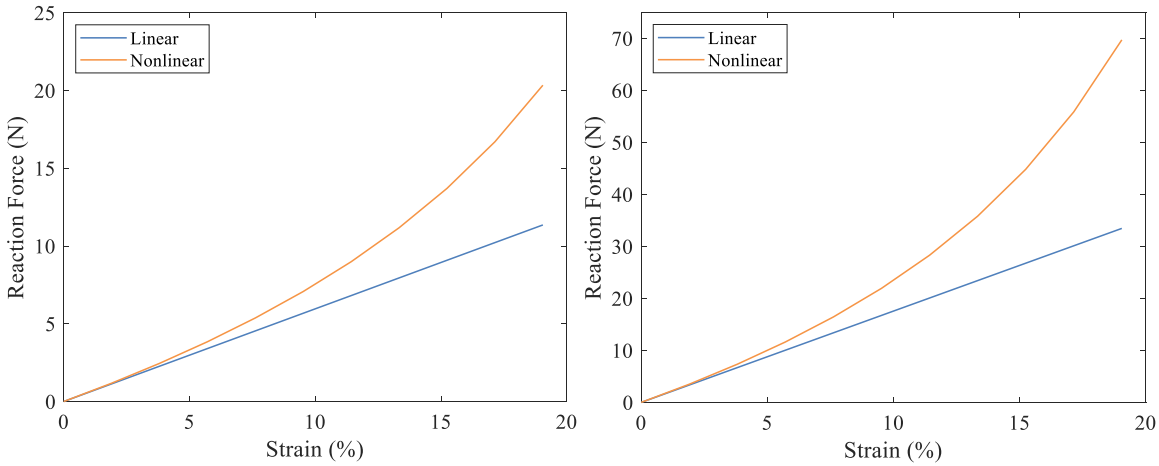

(c) Case 3, K* =0.1 (d) Case 4, $k_\theta \rightarrow \infty$

Figure 4-2 Comparison of Reaction Force vs lattice stretch (19%) for with linear torsional springs, large stretch linear vs nonlinear geometry

Figure 4-2 visualizes the nonlinear analysis through the force-displacement curve for Case 1 with large deformation. The linear model follows is a result of equilibrium equations with constant stiffness. As discussed, for the nonlinear model $F \neq KU$ and

hence finite element steps can show very high divergence from linear model especially for large stretch which can produce large beam strains. Later, in section 4.4.1, the same tests are performed with nonlinear rotational springs to compare the difference in the deformation and strain energy distribution across the lattice. For better visualization during large deformations, the deformed lattice plots are represented at an amplification factor of 0.7 that can be controlled in Abaqus.

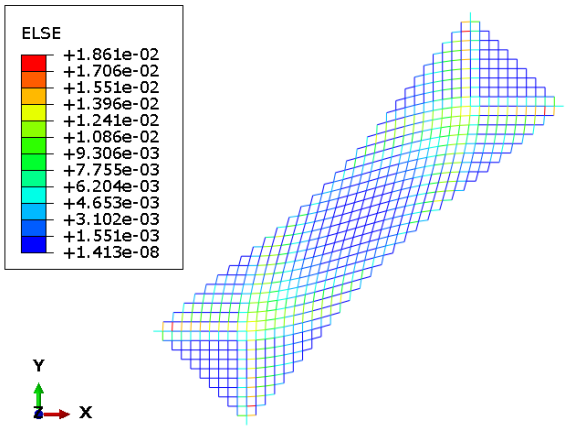

(a) Case 1, $k_\theta \rightarrow 0$, Linear Geometry

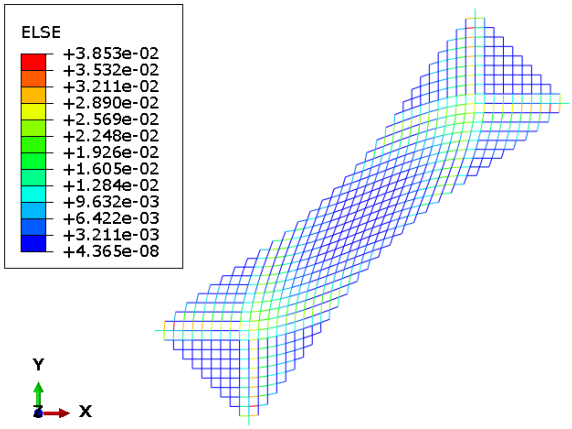

(b) Case 1, K* = 0, Nonlinear Geometry

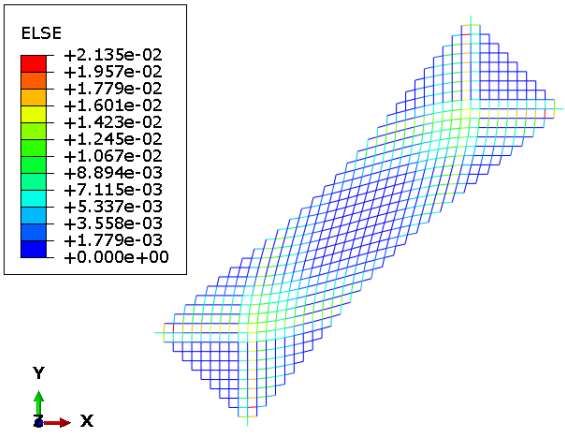

(c) Case 2, K* = 0.1, Linear Geometry

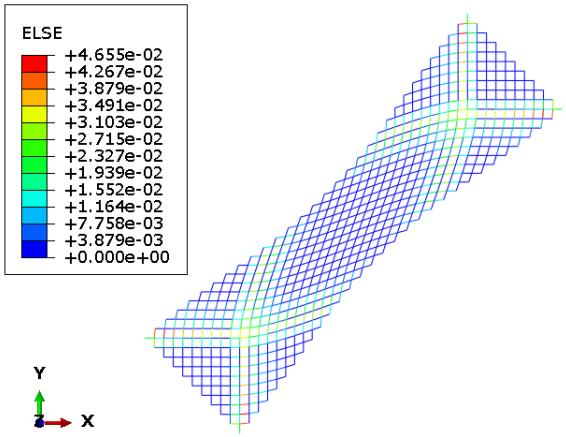

(d) Case 2, K* = 0.1, Nonlinear Geometry

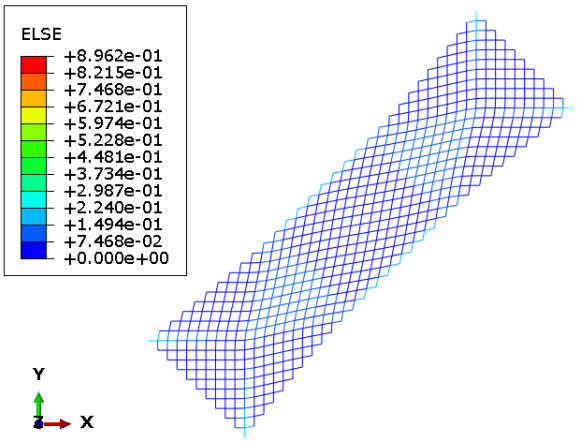

(e) Case 3, K* = 0.1, Linear Geometry

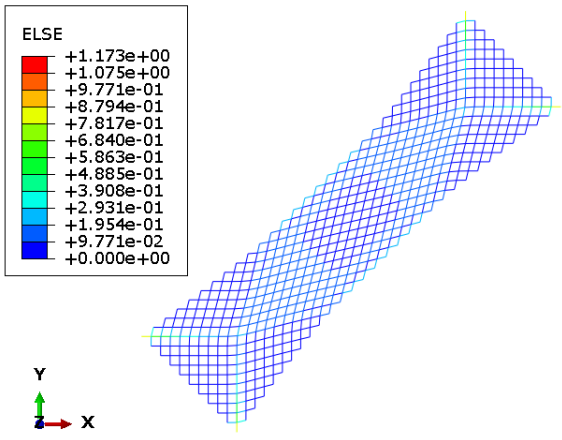

(f) Case 3, K* = 0.1, Nonlinear Geometry

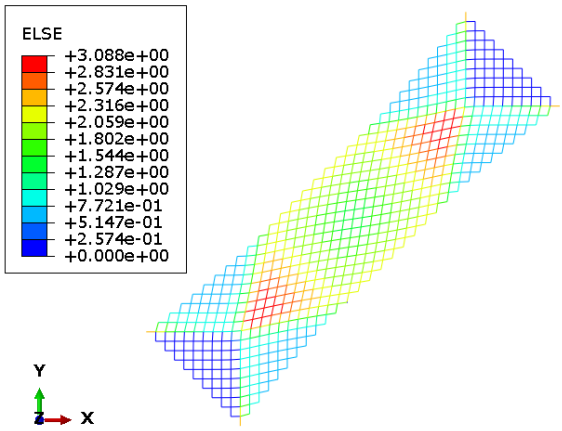

(g) Case 4, $k_\theta \to \infty$, Linear Geometry

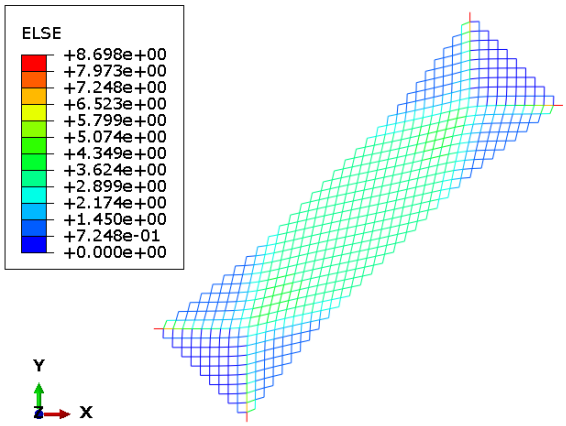

(h) Case 4, $k_\theta \to \infty$, Nonlinear Geometry

Figure 4-3 Total Strain Energy Distribution for the bias extension test implemented with linear spring (large stretch, 19%)

The results are presented for the four cases which define different orders of torsional stiffness at the lattice pivots. All four cases are presented for both, linear and nonlinear geometry for the large displacement load. The strain energy distribution for large deformation is similar to the distribution noticed for small deformation for linear

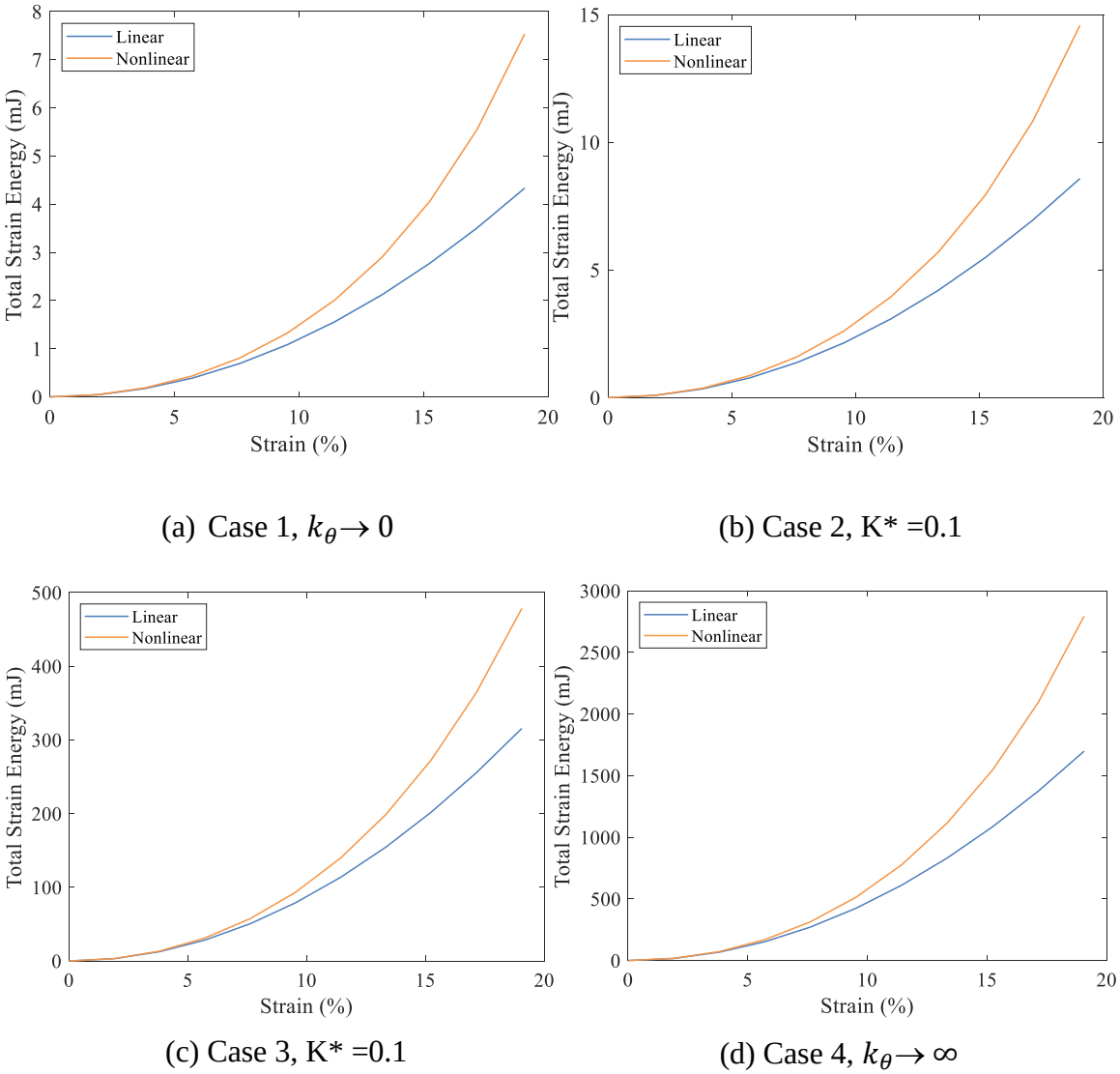

(a) Case 1, $k_\theta \rightarrow 0$

(b) Case 2, K* =0.1

(c) Case 3, K* =0.1

(d) Case 4, $k_\theta \rightarrow \infty$

Figure 4-4 Total Strain Energy vs lattice stretch (19%) for with linear torsional springs, linear vs nonlinear geometry

geometric model. However, we observe the necking is highly exaggerated when the large deformation is accounted for the geometric nonlinear model. Figures 4-3 (e) and (f) highlight the difference in the energy distribution which is amplified as the torsional stiffness is increased to reach a maximum value at case 4. The segregated bands of high strain energy diffuse entirely to a large area of necking dominated geometry with strain energy constituted by a constant order of magnitude, unlike the linear geometry model. The total strain energy as represented in Figure 4-4 shows the relative difference between the linear and nonlinear model widen aggressively past 3% lattice stretch.

Axial bias test was also performed with small deformation (0.33% lattice stretch) loads with the linear and nonlinear geometric model. The linear geometry small stretch results are discussed in section 3.2.2. The strain energy distribution contours for the small stretch with nonlinear geometry are presented in Appendix 7.1.

4.4 Torsional Spring Material Nonlinearity

The previous section only discussed the effects of only geometric nonlinearity for all four cases. Now, we introduce nonlinear springs at the pivots of the pantographic lattice which introduce nonlinear material behavior. Material nonlinearity introduced at pivot springs is a function of the parameter, β which is unconstrained for positive values as discussed previously. For a small lattice stretch, as approached here, β is varied to a wider range for linear and nonlinear geometry. A positive β signifies stiffening of the beam model while negative β values represent softening of the model. For both stiffening

and softening cases, the total strain energy is calculated for the deformed lattice. The model is invalidated if the total strain energy is negative. Graphically, extended decrement in the magnitude of β flattens out the strain energy curve below to a point where our model invalidates. By varying β from positive to negative values the nature of curve changes from concave up to convex. Hence, there is a mathematical limit on achieving the maximum softening behavior with the nonlinearity relation we have utilized.

For numerical results, β of order 10^3 is used to visualize significant nonlinear spring behavior. For the following numerical results, we define

$$\beta^* = \frac{\beta}{10^3}$$

where β^* is of order 1.

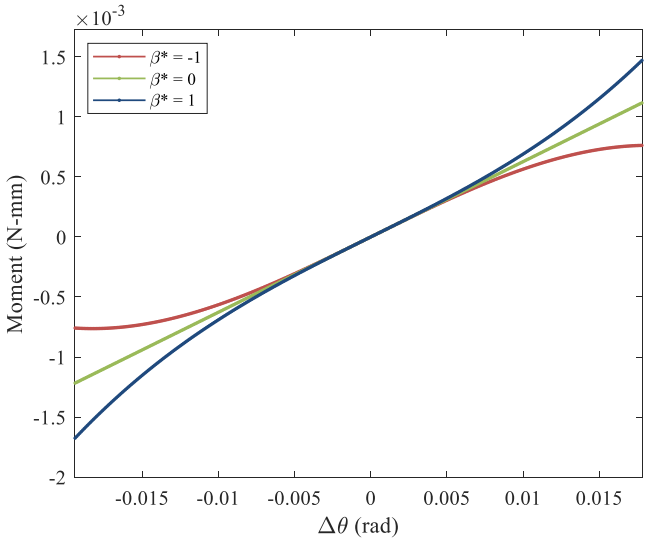

Figure 4-5 Moment-rotation relationship utilized in Abaqus to generate nonlinear spring behavior for Case 2, K =0.1*

Figure 4-5 visualizes the moment-rotation relationship that is utilized in Abaqus constraints to generate nonlinear torsional spring behavior. The plot shows three curves for different β^*. The same relationship is used for case 2 with K* =0.1. The curve is steeper for the larger magnitude of β^*.

4.4.1 Nonlinear Torsional Springs with Small Stretch

Small stretch extension tests are performed for pantographic lattice with small and large torsional resistance, viz. respectively Case 2 and Case 3. The study uses a small stretch of 0.33%. For both cases, the nondimensional torsional resistance, $K^* = 0.1$ and the parameter β^* is varied from -2 to 2 in 4 incremental steps. This allows us to study both the stiffening and softening behavior of the lattice due to the introduced nonlinear torsional springs. $\beta = 0$ reflects to the Case 2 and Case 3 with no material nonlinearity as studied in section 4.4.1.

With the relatively small stretch of 0.33%, the strain energy distribution is compared with the introduction of nonlinear springs. For small stretch with nonlinear rotational spring behavior, the nonlinear geometry does not introduce any significant difference. Hence, the total strain energy is plotted against lattice stretch (%) for the geometric linear model only. For both case 2 and case 3, it is observed that the total strain energy increases with the spring stiffness. The total strain energy is a quadratic function of the strain. However, as the softening behavior is amplified, the total strain energy detracts and starts decreasing which is impossible and hence is a limit to our model.

Case 2, K*=0.1, β^* = [-2, -1, 0, 1, 2]

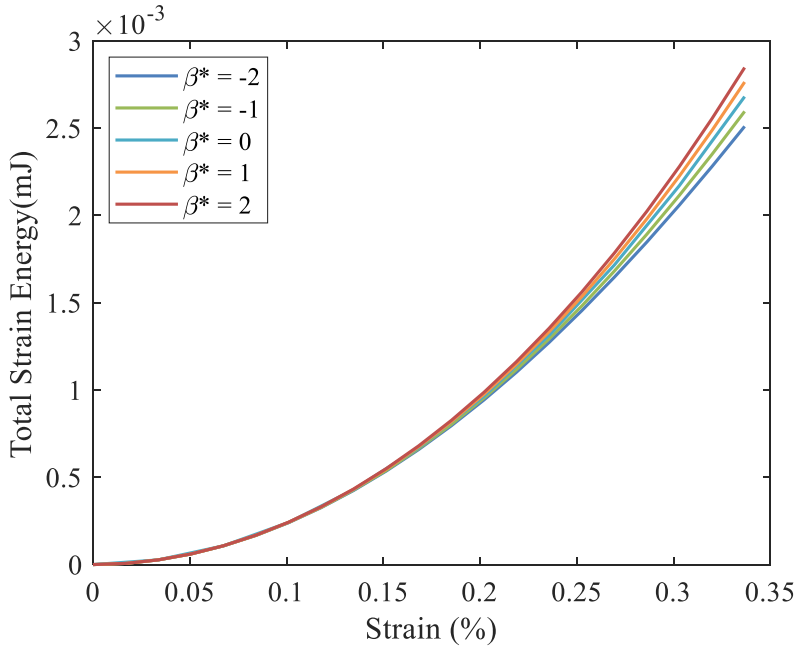

(a)

Case 3, K*=0.1, $\beta^* = [-2, -1, 0, 1, 2]$

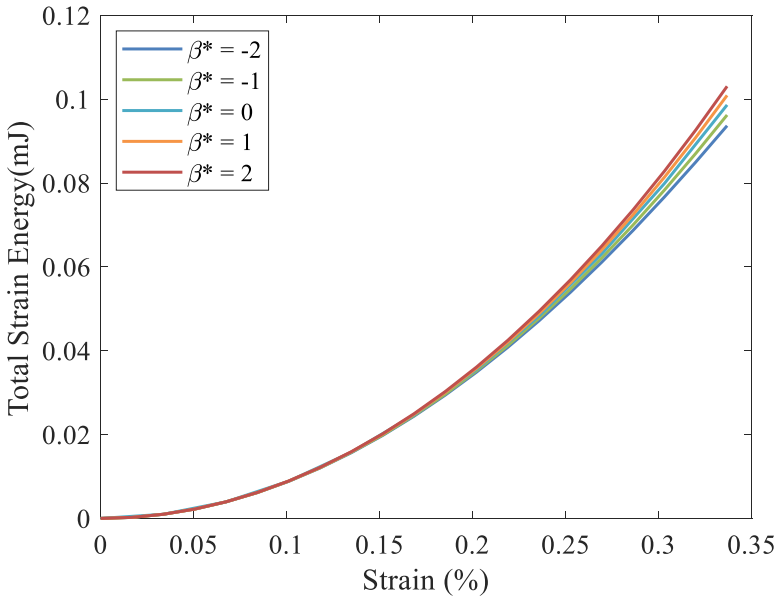

(b)

Figure 4-6 Total Strain Energy with introduced nonlinear springs for Case 2 (a) and Case 3 (b) with small lattice stretch, K=0.1, linear geometric model*

The bar graphs below compare the total strain energy for the linear geometry model with nonlinear geometry.

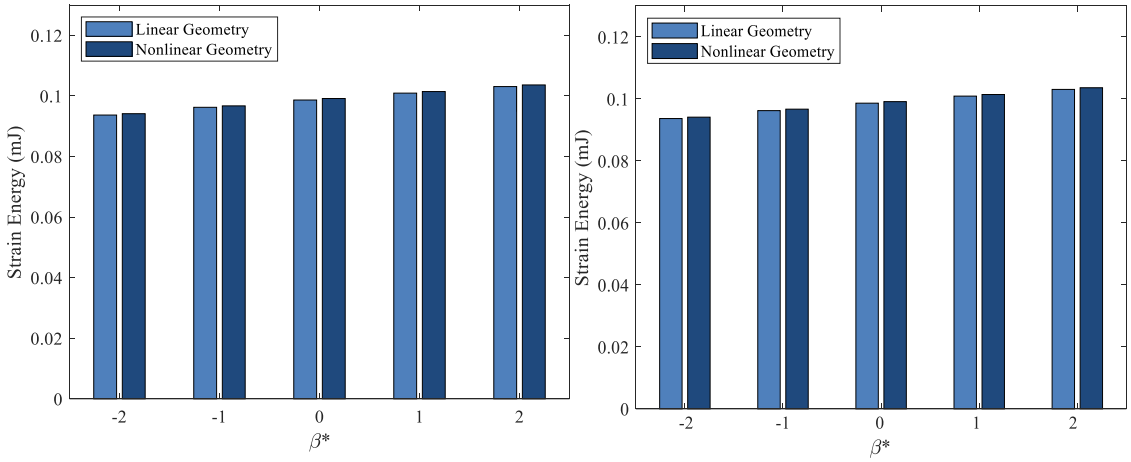

Figure 4-7 Strain Energy for Linear vs Nonlinear Geometry, Case 2 (a) and Case 3 (b) for small lattice stretch (0.33%)

The total strain energy increases slightly for the transformation from linear to nonlinear model for both the cases. Fig 4-7 (a) and (b) show that any changes in the torsional stiffness are more varied for low orders of torsional stiffness in comparison to the higher orders. In Fig 4-8 contours representing the total strain energy for $\beta^* = [-2, 0, 2]$ are compared for Case 2 and Case 3. $\beta^* = 0$ reflects the constant spring stiffness. The plots presented have a deformation amplification of 40. While only minute differences are observed for Case 2, Case 3 strain energy distribution varies from focused high energy bands surrounding a homogeneous low energy region in the middle of the lattice which decreases as the lattice is stiffened.

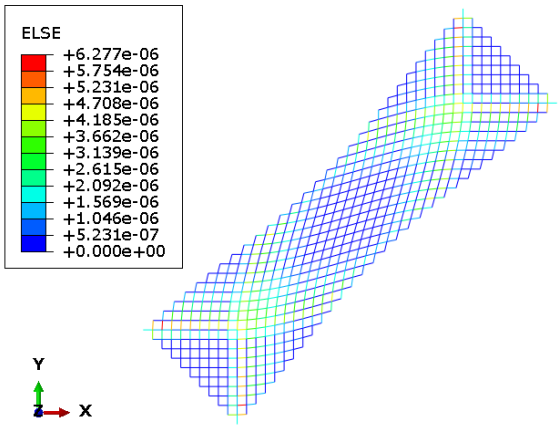

(a) β^*= -2, Case 2

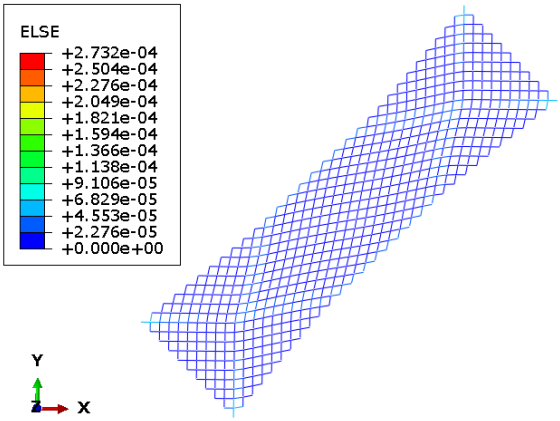

(b) β^*= -2, Case 3

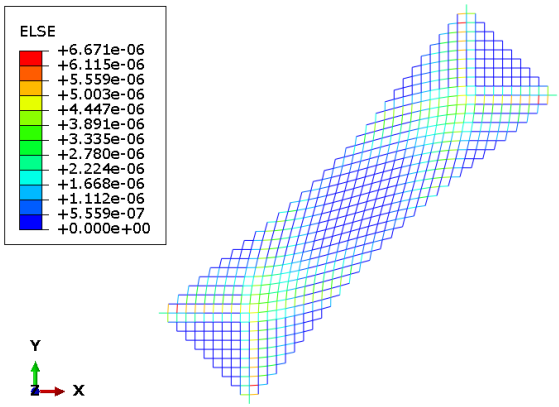

(c) β^* = 0, Case 2

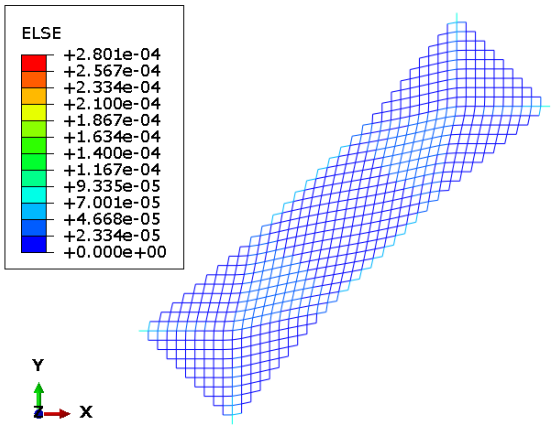

(d) β^* = 0, Case 3

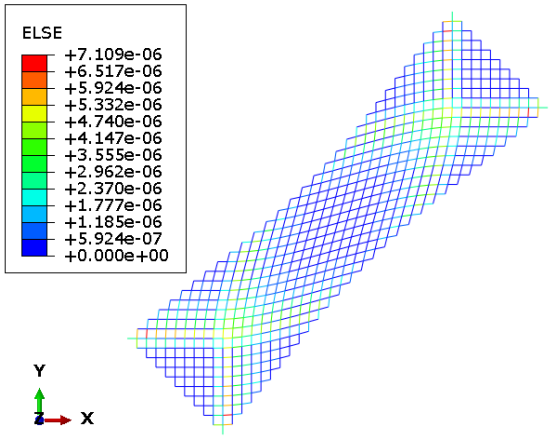

(e) β^* = 2, Case 2

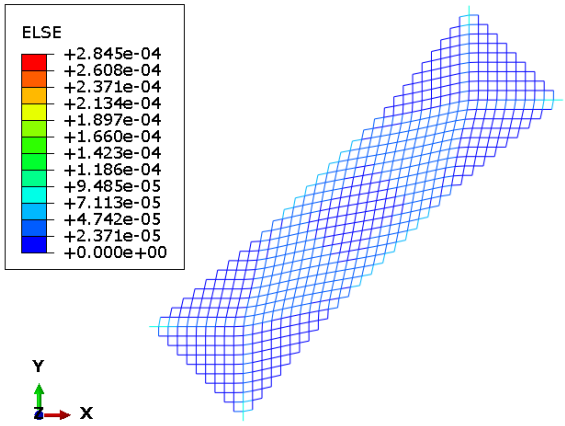

(f) β^* = 2, Case 3

Figure 4-8 Total Strain Energy Distribution for Case 2 (left) and Case 3 (right), K =0.1 with nonlinear springs and linear geometry model (small lattice stretch, 0.33%)*

4.4.1 Nonlinear Torsional Springs with Large Stretch

The small stretch test performed in section 4.4.1 is extended to study the large deformation for the linear geometric model keeping the remaining parameters the same. For a large stretch of 19%, we can see that the nonlinear spring behavior when coupled with the nonlinear geometry model produces highly varied strain energy distribution. The total strain energy of the lattice is also orders of magnitude larger for the nonlinear geometry model. Fig 4-11 shows the total strain energy of the model for stiffening cases. Since the order of stiffness is large, any variation in β^* largely amplifies the total strain energy as a result. For large stretch, a limited softening behavior can be observed. Figure 4-9 shows the difference in magnitude of the total strain energy for low order of torsional resistance with integrated softening and stiffening behavior.

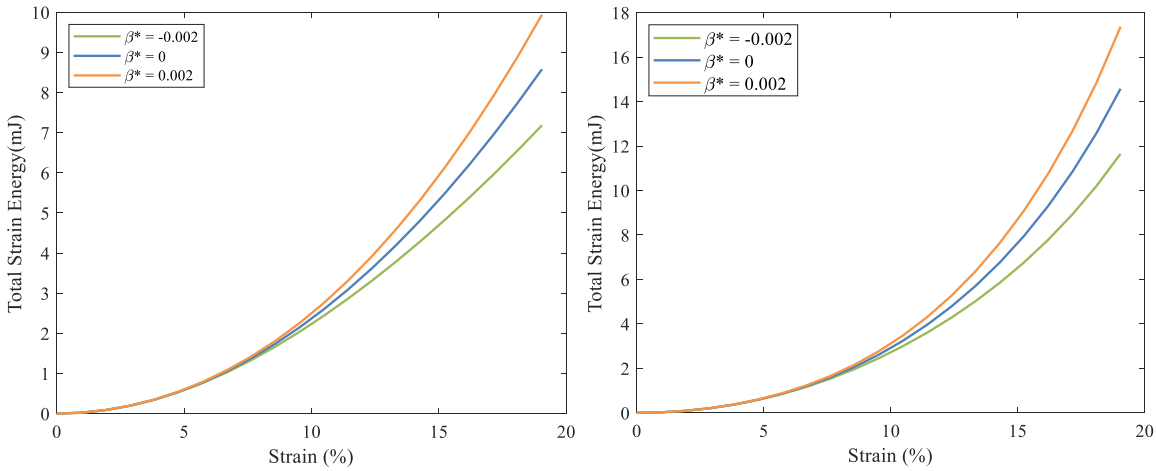

Figure 4-9 Total Strain Energy for Case 2 K=0.1, linear(left) vs nonlinear geometry(right) with large lattice stretch, (19%)*

The reaction force for Case 2 softening and stiffening is shown in Figure 4-10.

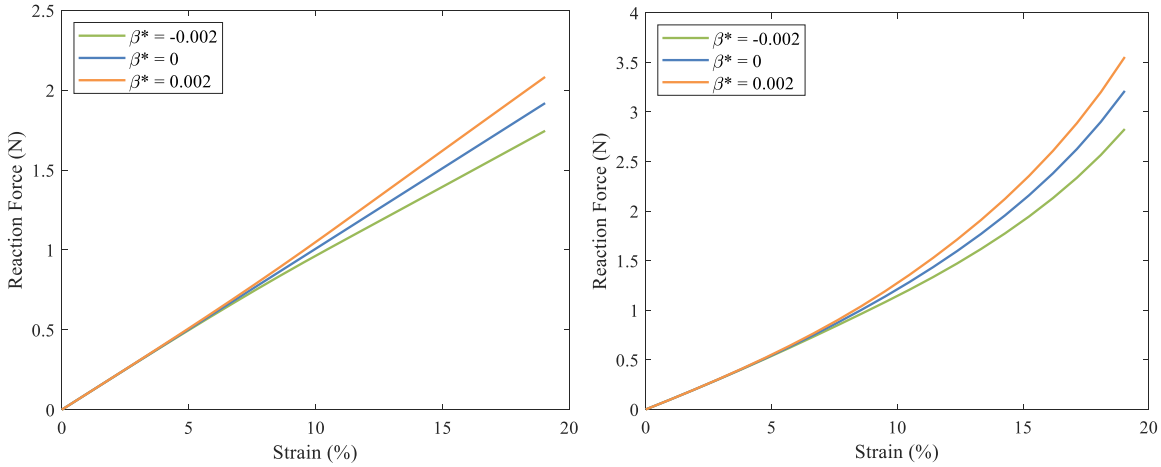

Figure 4-10 Comparison of Reaction Force vs lattice stretch Case 2 K=0.1, linear (left) vs nonlinear geometry (right) with large lattice stretch, (19%)*

Case 2, K*=0.1, β^*= [1, 2]

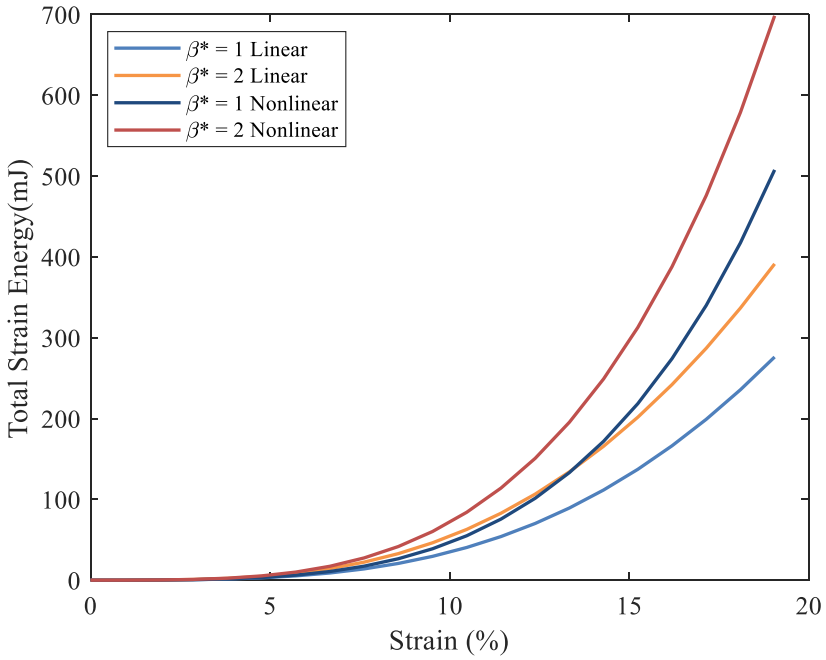

Figure 4-11 Total Strain Energy with introduced nonlinear springs for Case 2 (large stretch, 19%), K=0.1*

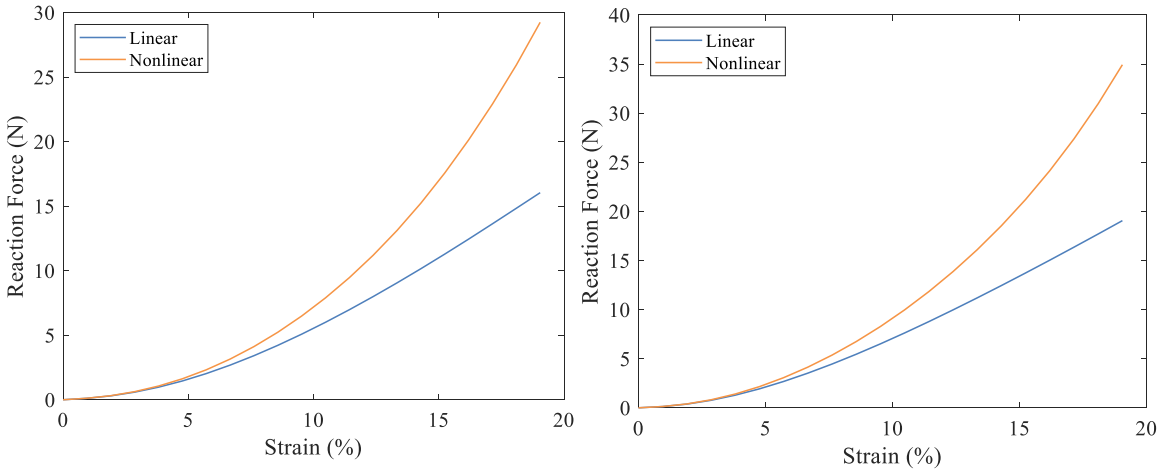

Figure 4-12 Comparison of Reaction Force vs lattice stretch for with nonlinear torsional springs for Case 2 with $\beta^* = 1$ and 2 (large stretch, 19%)

In Figure 4-12, the reaction force at the loaded lattice edge is plotted against the lattice stretch. Figure 4-13 shows the importance of nonlinear models for studying large deformations in the pantographic lattice. As in Figure 4-13d, the increased stiffening of the pivots results in a highly stretched zone of high strain energy is observed, while the linear model in Figure 4-13c suggests a comparatively larger pocket of less energy.

It is evident that the strain energy is better captured by the nonlinear models. Figure 4-16 shows that for the higher orders of stiffness, the bandgap between the linear and nonlinear models are significant. Unlike Case 2, the strain energy distribution does not differ significantly for $\beta^* = 1$ and $\beta^* = 2$ for both the linear and nonlinear models as evident from Figure 4-18.

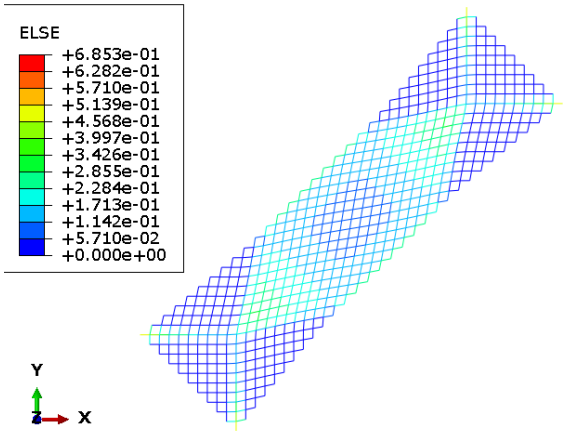

(a) $\beta^* = 1$, Case 2, Linear Geometry

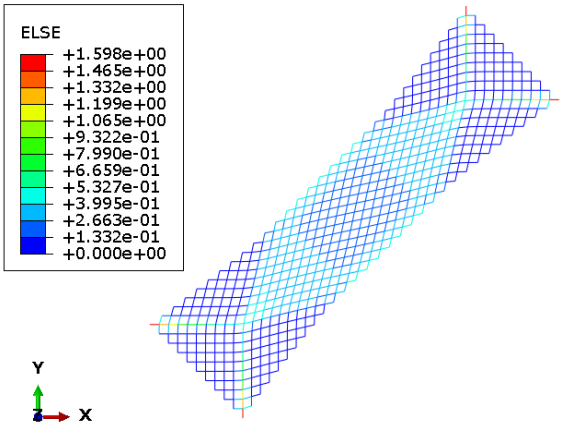

(b) $\beta^* = 1$, Case 2, Nonlinear Geometry

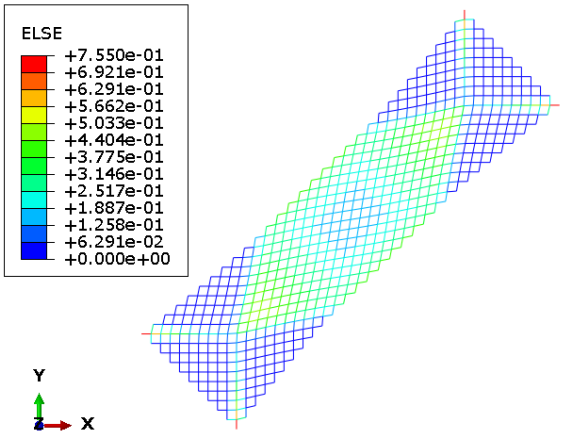

(c) $\beta^* = 2$, Case 2, Linear Geometry

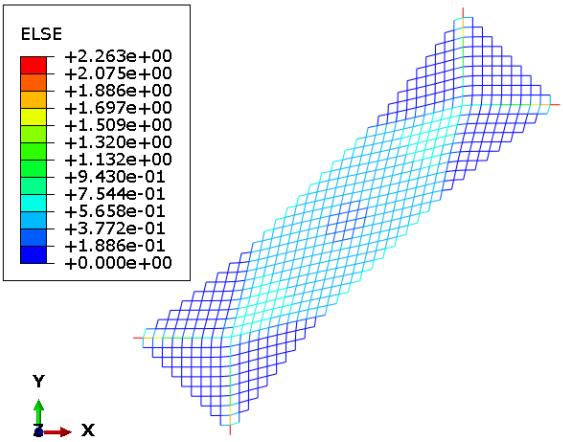

(d) $\beta^* = 2$, Case 2, Nonlinear Geometry

Figure 4-13 Total Strain Energy Distribution for Case 2, K =0.1 with Linear (left) and Nonlinear (right) Geometry (large stretch, 19%)*

Case 3, K*=0.1, β^* = [1, 2]

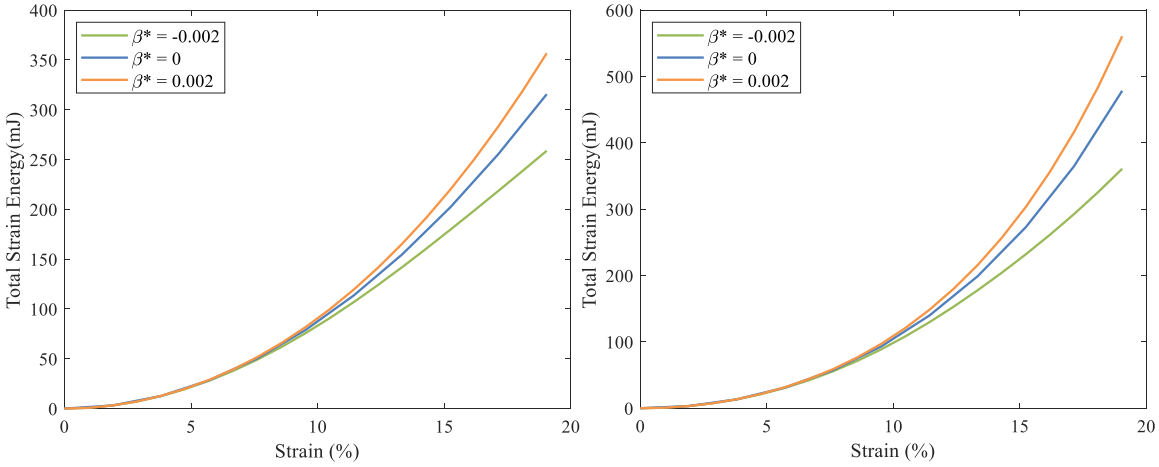

Figure 4-14 Total Strain Energy with introduced nonlinear springs for Case 3 (large stretch, 19%), K=0.1*

Figures 4-14 and 4-15 show the difference in the mechanical behavior of linear and nonlinear geometric models for Case 3 order of torsional resistance. Contrary to the nonlinear geometry model, the reaction force developed for softening cases in the linear model flattens out with increasing stretch.

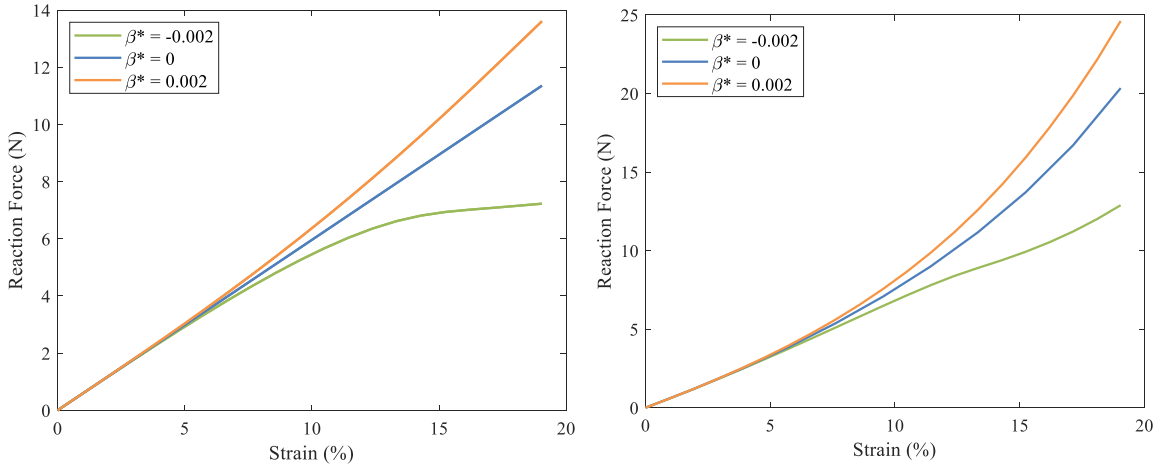

Figure 4-15 Comparison of Reaction Force vs lattice stretch Case 3 K=0.1, linear (left) vs nonlinear geometry (right) with large lattice stretch, (19%)*

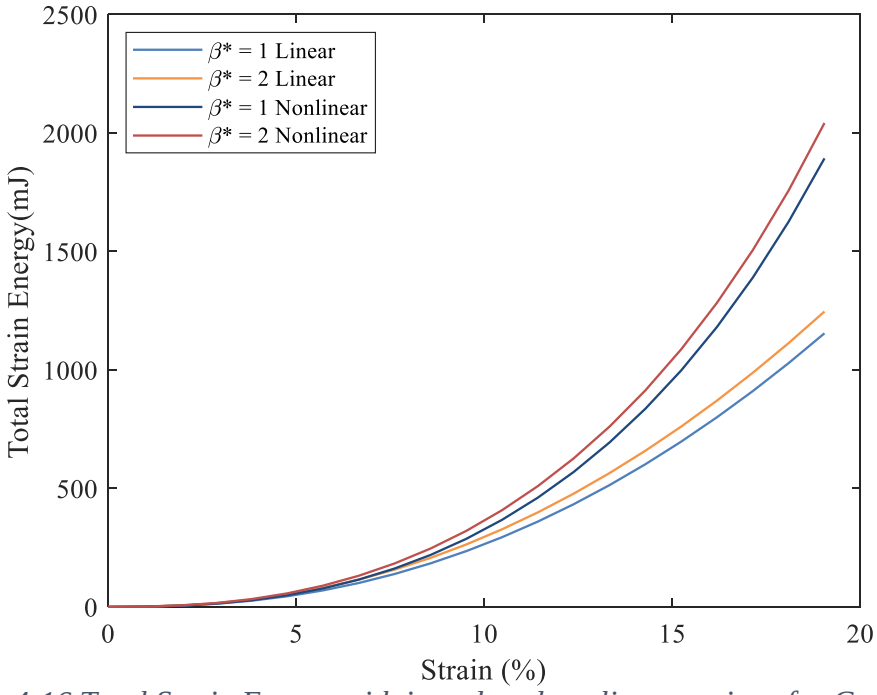

Figure 4-16 Total Strain Energy with introduced nonlinear springs for Case 3 (large deformation), K=0.1*

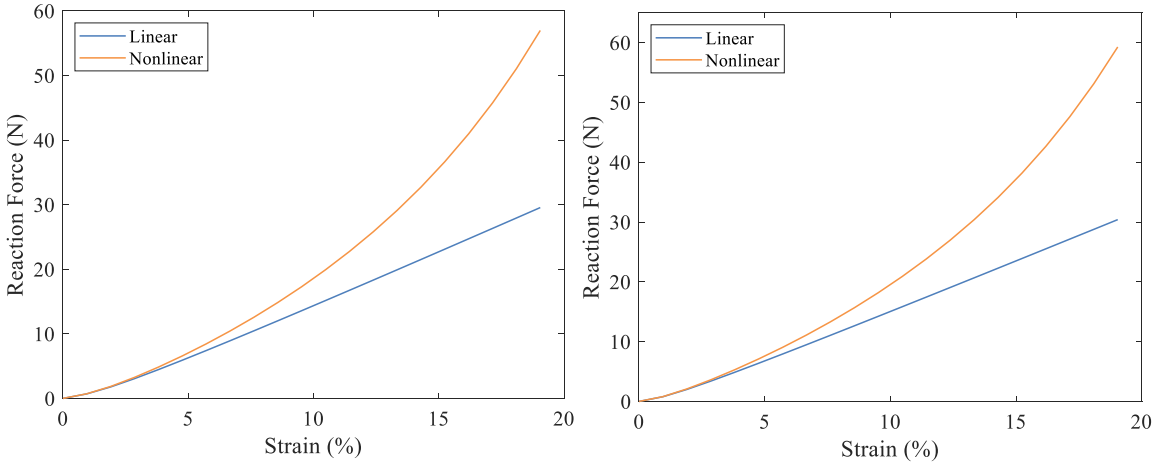

Figure 4-17 Comparison of Reaction Force vs Strain for with nonlinear torsional springs for case 3 with $\beta^* = 1$ and 2

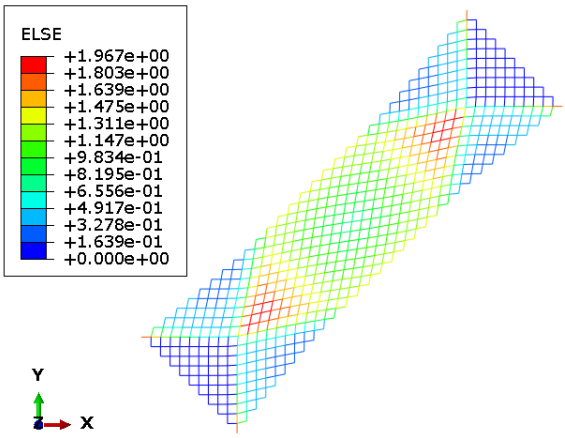

β^*= 1, Case 3, Linear Geometry

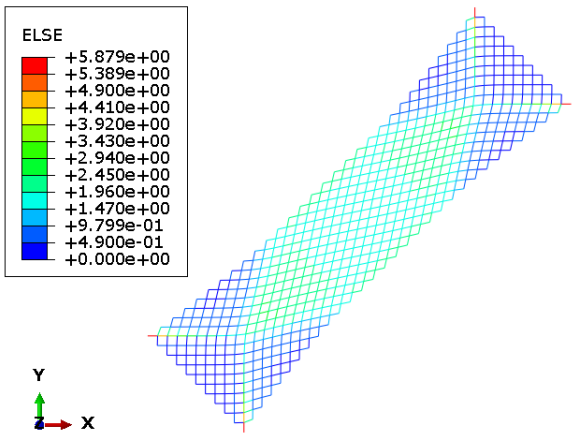

β^* = 1, Case 3, Nonlinear Geometry

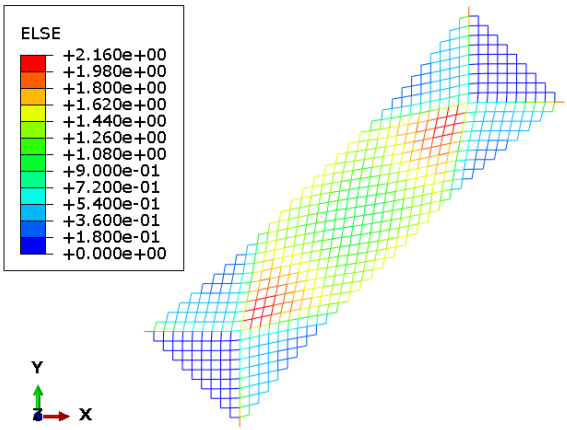

β^*= 2, Case 3, Linear Geometry

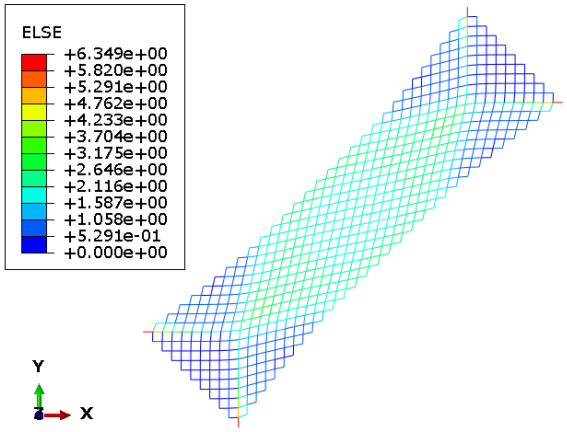

β^*= 2, Case 3, Nonlinear Geometry

Figure 4-18 Total Strain Energy Distribution for Case 3, K =0.1 with Linear (left) and Nonlinear (right) Geometry*

4.5 Quantification of Nonlinearity for Lattice Energy

This chapter discusses the comparative effects of engaging a nonlinear spring stiffness to a constant spring stiffness. The strain energy for the torsional spring elements can be calculated as

$$E_{spring} = k_\theta \left(\frac{1}{2}\Delta\theta^2 + \frac{1}{4}\beta\Delta\theta^4\right) \tag{4.6}$$

We can consider a similar relation between the total energy for the lattice and the total strain in the lattice to observe the effect of β on the total strain energy of the lattice. Hence, we assume the total strain energy of the lattice as

$$E_{lattice} = A \left(\frac{1}{2}\Delta x^2 + \frac{1}{4}B\Delta x^4\right) \tag{4.7}$$

And utilize curve fitting techniques to study the parameter relating nonlinearity, B by equating the total lattice strain energy to the above-assumed relation. Here, Δx is the axial displacement along the direction of the applied load. The coefficients evaluated were in a 95% confidence interval for the R-square values calculated in MATLAB curve fitting toolbox, *cftool* [24].

The R-squared values are calculated using a linear regression model that indicates a proportionate amount of variation in the dependent variable *y* explained by the independent variable *x*. For our mode, $E_{lattice}$ is the dependent variable and Δx is the independent variable. R-square is a measure of the success of fit in accommodating the variation in the data sets. R-square can vary from 0 representing a poor fit to a maximum

of 1 for a good fit. For small stretch loading, with a nonlinear spring with Case 2 or Case 3, using K* = 0.1, the coefficients A and B, the R-square was found to be 0.999 or greater suggesting a very good fit. The plots below relate the parameters B and β^* for small strain.

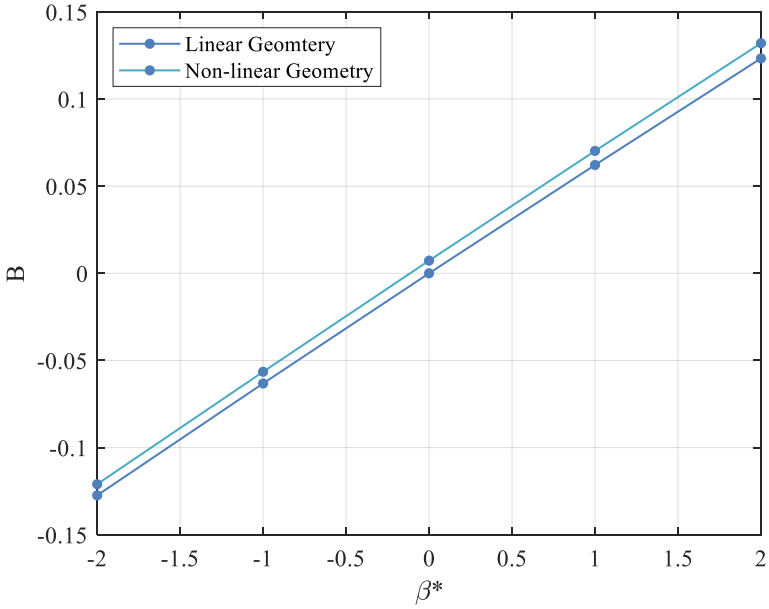

Figure 4-19 Nonlinearity parameter B vs β^*, small deformation (0.33%), Case 2, K =0.1*

The parameters obtained for the curve fit model show a high degree of coherence as can be inferred from the R-square values. The model is shown to be accurate for the overall lattice energy for small beam deformations with nonlinear spring behavior. This is very useful to predict the behavior of lattice for a finite range of β. However, for large geometric beam deformations, the confidence levels obtained for the curve fitting are not appropriate which makes this model not useful for predicting large stretch behavior. Figures 4-19 and 4-20 show the relationship between the nonlinear parameter β and the curve-fit parameter for equation 4.7. For both cases, the curve closely follows a linear relation for small strain for linear and nonlinear models. When $\beta^* = 0$, the lattice model

has no torsional spring material nonlinearity. However, the model still predicts some nonlinearity which is introduced due to the geometric nonlinearity even at small deformations. This is observed for both Case 2 and 3. However, for large deformations, no concrete trend is observed in the relations between the computed parameters as can be observed in Figure 4-21.

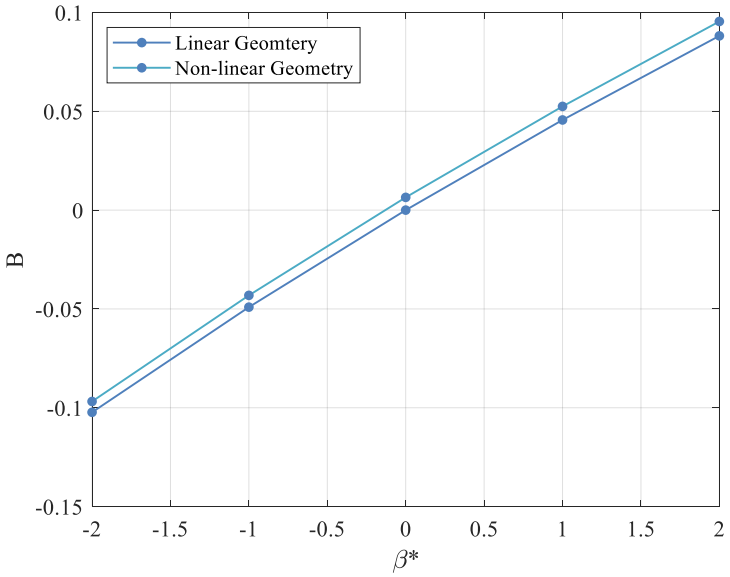

Figure 4-20 Nonlinearity parameter B vs β^*,small deformation (0.33%), Case 3, K =0.1*

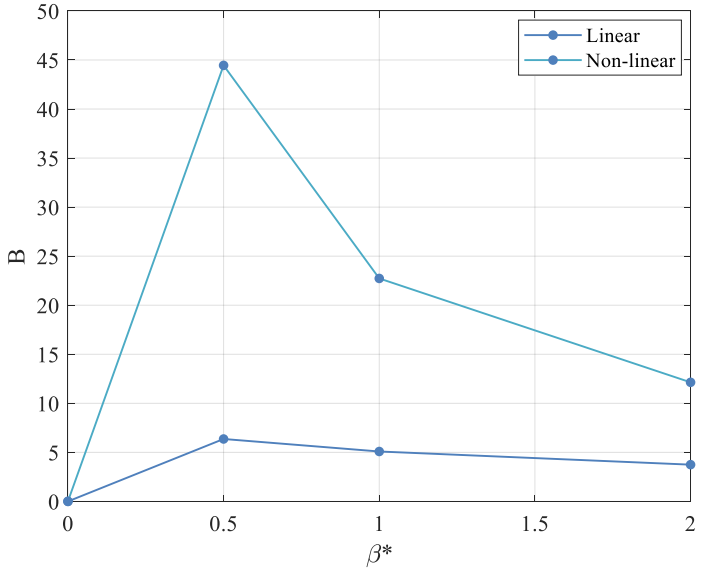

Figure 4-21 Nonlinearity parameter B vs β^*, large deformation (19%), Case 3, K =0.1*

Chapter 5 3D pantographic Lattice

The 2D pantographic sheets can be extended to the third dimension by the inclusion of a third continuous beam fiber array that runs perpendicular to the plane of the existing pantographic sheet. Since our pantographic sheet is modeled in an x-y plane, the array of perpendicular fiber runs in the $+z$ direction connecting the parallel planar sheets. The beam profile for the 3D pantographic lattice is considered to be a square prism with the existing beam length as in the 2D model.

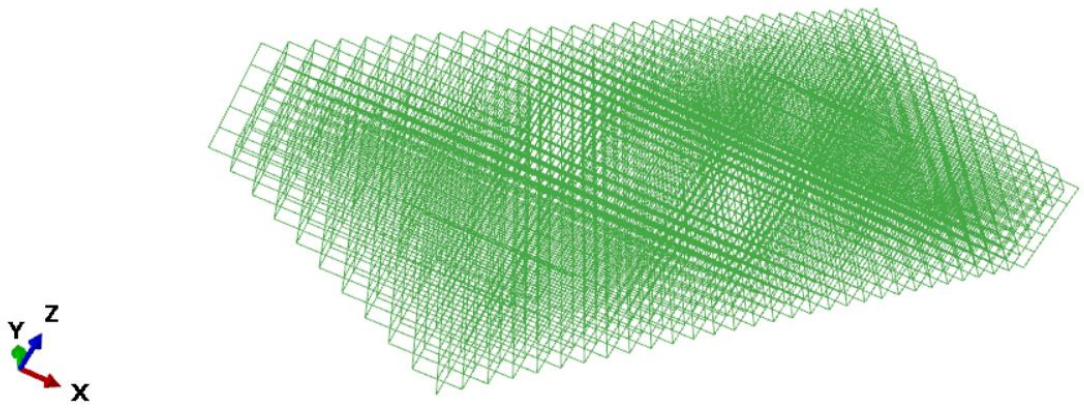

Figure 5-1 3D Pantographic beam lattice model in Abaqus Standard

Pivots at the intersection are now constituted by 3 discrete spring connections which can be created to be independent of each other. Similar to the 2D pantographic lattice, the participating nodes of fibers at a pivot at all times are constrained in the translatory degree of freedom. The rotational degrees of freedom of these nodes behave

as per the spring stiffness and the constraints established as per the four cases discussed previously.

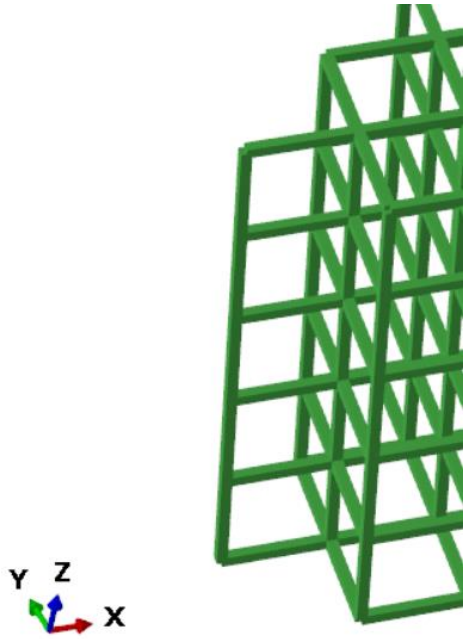

Figure 5-2 Square beam profile for the 3D pantographic lattice

In this study, the 3D lattice model is constituted by six layers of 2D pantographic sheets interconnected by vertical beam fibers. The beam material properties for the 3D pantographic lattice are the same as discussed in section 2.1. However, the beam profile in 3D is assumed to be a square prism of dimensions b = 0.495 mm, l = 4.95 mm, h = 0.495 mm. Hence, the slenderness ratio, n = $\frac{h}{l}$ = 0.1 is the same as for the 2D pantographic lattice model.

5.1 Degrees of freedom in three dimensions

For a point *j* in 3D space, there exist three translational degrees of freedom, each along the three axes in the coordinate system i.e., *x*, *y*, and *z*-axis. Correspondingly, there exist three rotational degrees of freedom which can be visualized as below:

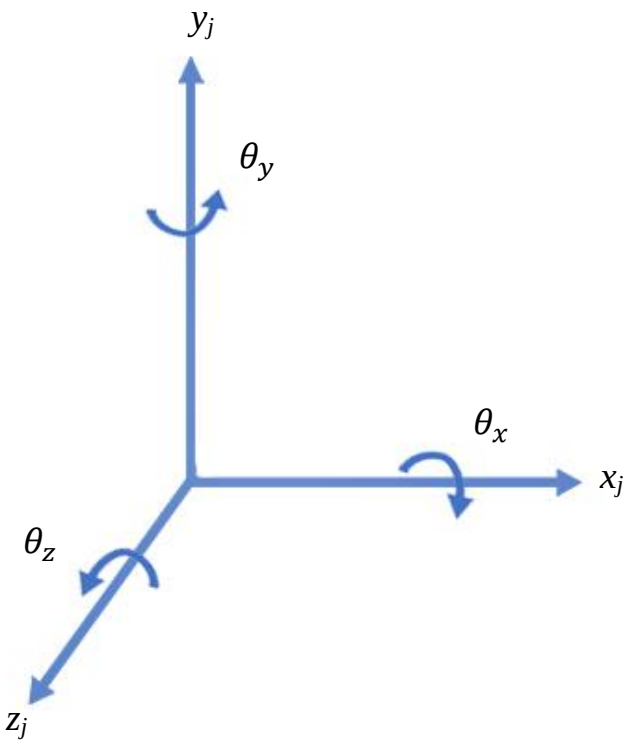

Figure 5-3 Degrees of freedom for a point in 3D space

The direction of rotation can be found using the right-hand curl rule. The depicted directions of rotations in the above figure are positive.

Our frame elements comprise of two nodes, each with six degrees of freedom as understood above. For a two-node 3D frame element the nodal displacements and rotations can be represented as below.

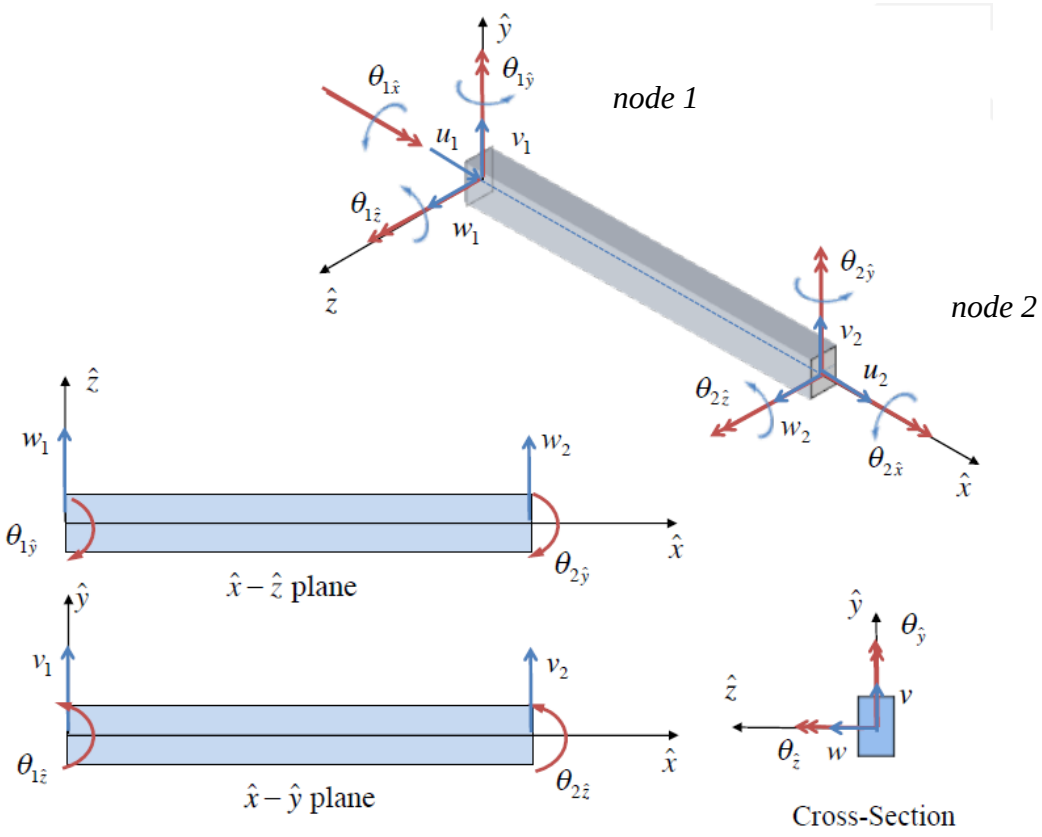

Figure 5-4 Representation of local displacements and rotations for a 3D frame element

Here *u*, *v*, and *w* are the displacements along the local *x*, *y*, and *z* directions for the frame with nodes 1 and 2.

5.2 Kinematic Constraints at the pivots in the 3D lattice model

The beam connections in 2D pantographic sheets employed only one pivot across the two participating nodes of different beams. In 3D, the kinematic constraints are applied to 3 pivots at every beam connection. The set of kinematic constraints are the same as the previous. To recall, to achieve the generalized rotational stiffness at the joints of the pantographic lattice we have the following primary requirements:

1) The pivots at a beam connection should share the same translatory motions i.e., the displacement across the nodes should be equal.
2) The rotational degrees of freedom should be allowed to have some finite value of positive torsional resistance. The varying order of magnitude of torsional resistance at these pivots can be achieved as discussed in the 2D model.

In 2D, the beam connections are comprised of 2 nodes from different beam fibers. Similarly in 3D, the beam connections comprise of 3 pivots each from a different fiber. The MPC Pin connection in Abaqus allows for equal displacements for the connected nodes while leaving the rotational degree of freedom independent if they exist. Hence, an MPC Pin connection is sufficient to replicate Case 1 in 3D lattice too. To implement a finite torsional resistance between the pivots, a torsional spring is a setup connecting the degree of freedom we are interested in. The 3 pivot Pin setup and the torsional spring are explained in detail in the next section.

This section discusses the Abaqus implementation of the beam connections and the kinematic constraints employed to achieve torsional springs at the pivots.

5.2.1 Multi-point Constraint Pin

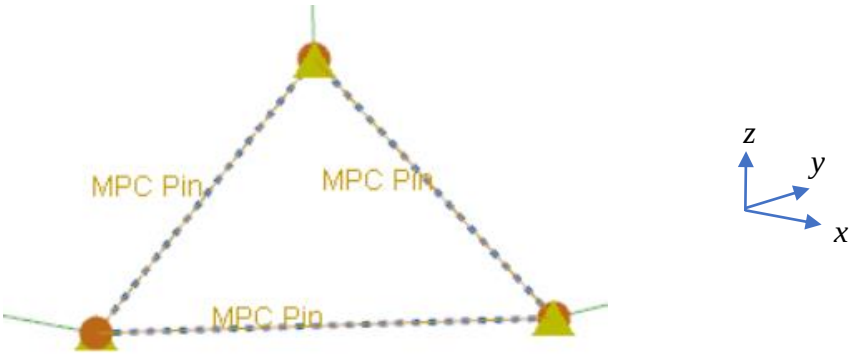

Figure 5-5 Representation of Multipoint constraints setup at a pivot constituted by three nodes in 3D space

Figure 5-5b depicts the three PIN constraints for visual understanding as produced in Abaqus. While implementing the constraints in Abaqus only 2 are necessary as the third is followed automatically by Abaqus because of the nature of the constraint.

Although the pivots constitute of 3 pairs of node-set [(1,2),(2,3),(3,1)], the driving constraints for a PIN joint can be conveyed via establishing relations between any two as

$$\Delta\theta_{12} = \theta_2 - \theta_1$$

$$\Delta\theta_{23} = \theta_3 - \theta_2$$

Hence from the above two relations,

$$\Delta\theta_{31} = \theta_3 - \theta_1 = \Delta\theta_{23} + \Delta\theta_{12} \tag{5.1}$$

where θ_i is the rotation of fiber *i* at the joint of concern.

Hence the third pair is dependent on the relations between the first two pairs. This can be utilized by constraining only 2 pairs of nodes of a joint in Abaqus using python scripts.

5.2.2 Torsional Springs

The Moment for a pair can be defined as

$$M_{ij} = K_{ij}\Delta\theta_{ij} \tag{5.2}$$

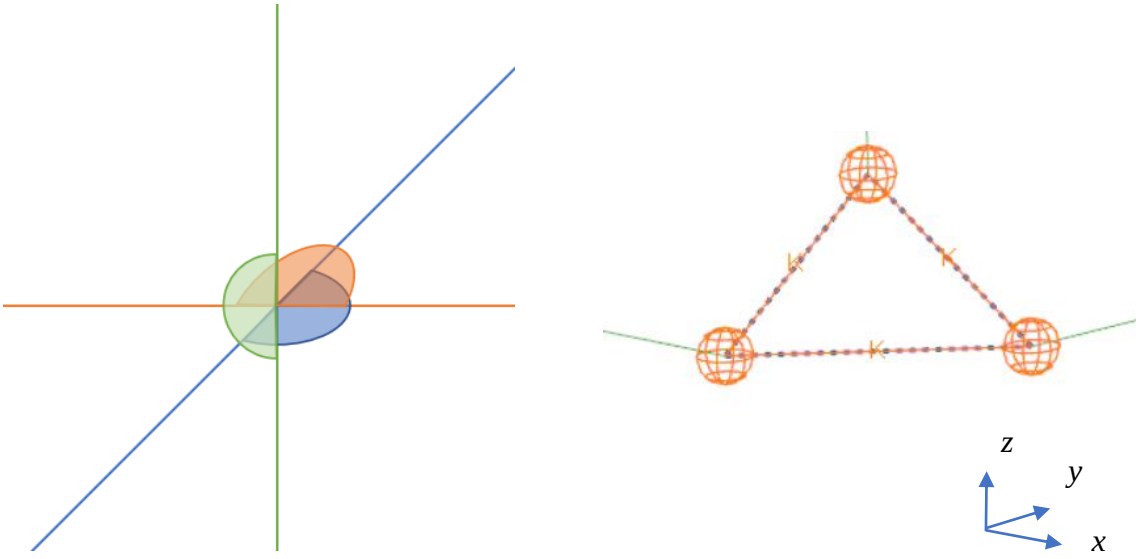

(a) (b)

Figure 5-6 Representation of three torsional springs of stiffness k at a pivot constituted by three node pairs in 3D space

The PIN connections at a pivot are represented in figure 5-6a. The colored axes represent the corresponding rotational degrees of freedom that are constrained in the global coordinate system. The 3 linear springs created for 3 node pairs at a joint employs different degrees of freedom for each pair. For the beam fibers oriented along the x and y-axis, the torsional spring is set up along the global z-direction. Similarly, the torsional spring along the x-axis engages the beam fibers oriented along global y and z directions. Finally, the torsional spring along the y-axis is created in a similar manner between beam fibers oriented along global x and z directions. The linear torsional springs at all joints have the same spring stiffness. The spring stiffness is k_θ is the same for every spring similar to the assumption used for the 2D model. Hence for case 1, only the MPC Pin constraints are active throughout the lattice, meanwhile, for cases 2, 3, and 4, the springs are also activated along with the MPC Pin constraint.

The 4 cases differentiating the different orders of torsional resistance are implemented in the 3D model as well. For the 2D pantographic lattice model, all degrees of freedom for nodes are constrained. However, if the kinematic constraints for the 2D model are replicated in the 3D model, nodes that do not lie on the longitudinal ends of the lattice remain with free degrees of freedom. To overcome this uniqueness problem, the nodes are set to have zero rotation along the longitudinal axis of the beam element to remove twisting as described in section 5.3. For all the cases the twisting deformation is neglected by implementing constraint equations.

In 2D, we approached case 4 by incrementing the stiffness of the rotational springs from case 3 to a very large magnitude. Case 4 in 2D reflects rigid joints at the

intersection of the beam fibers. In 3D, as twisting of the beams is homogenized using essential boundary conditions, Case 4 obtained via raising spring stiffness of Case 3 to a large magnitude does not exactly resemble the rigid pivots at the beam intersections, which equates both bending rotation and twist at the beam intersection node. A rigid connection can be set up by modeling only one node at the fiber intersections, with constraints that all three displacement components and all three rotation components are shared for all three beams at the connected nodes. The rigid model does not require any additional constraints to be set up to achieve rigid connection, all displacements and all rotations are the same at the beam connections and are implemented directly in the beam finite stiffness assembly process.

5.3 Boundary Conditions

Similar to the 2D model, the 3D pantographic lattice is loaded along the bisector of planar arrays and perpendicular to the z-axis. The lattice is constrained to 3 sets of boundary conditions. The southwest end (red) of the lattice is rigidly constrained by fixing all 6 degrees of freedom. Meanwhile, the loaded end (blue) is subjected to a series of linearly ramped displacement loads along the longer edge of the lattice as depicted in Figure 5-7.

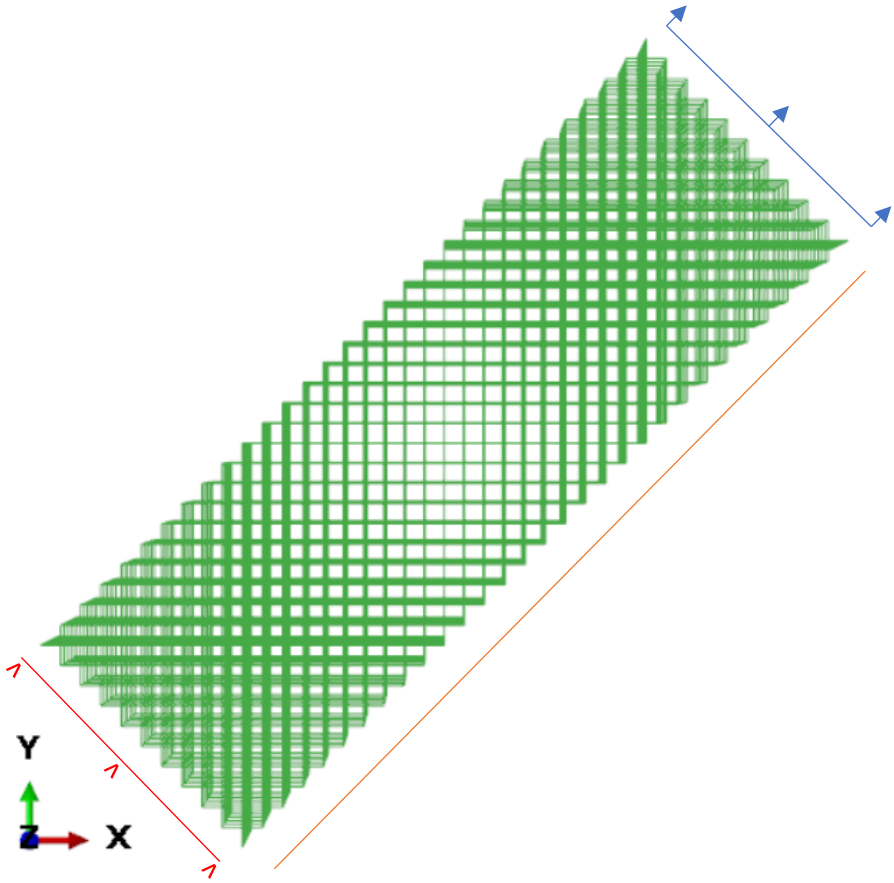

Figure 5-7 Essential Boundary conditions on the loaded edges of the lattice

The essential boundary conditions are defined at the loaded edge,

$$u_x = d$$

$$u_y = d$$

$$u_z = 0$$

$$\theta_x = \theta_y = \theta_z = 0$$

The essential boundary conditions at the rigid end are defined as

$$u_x = u_y = u_z = 0$$

$$\theta_x = \theta_y = \theta_z = 0$$

To avoid the twisting of beams, the 3D pantographic beam model also has a constrained rotational degree of freedom along the beam axis. The beam fiber oriented along the global x-axis has a fixed rotational degree of freedom along the x-axis. Similarly, fixed rotations are applied along the y and z-axis for lattice fibers that are oriented in the y and z-axis respectively. The remaining 2 degrees of freedom for each node are bound by the rotational springs as discussed in the previous section.

For all nodes on fibers oriented along *i* axis:

$$\theta_i = 0$$

By constraining one rotational degree of freedom for case 4, the twisting deformation energy is removed. This is the contrast between case 4 and the rigid lattice model. The

rigid lattice model allows for twisting of the beams accounting for some small twisting deformation energy presented in the numerical results in section 5.4.

For displacement component magnitude, d, along fiber directions in the x-y plane, the total displacement load (elongation stretch) along the bisector of the beam arrays is

$$u_{disp} = \sqrt{u_x^2 + u_y^2} = \sqrt{2d^2} = d\sqrt{2}$$

For a small stretch,

$$d = \frac{1}{2}mm, \qquad u_{stretch} = \frac{1}{\sqrt{2}}mm \ \ (0.33\%\ stretch)$$

For a large stretch,

$$d = 20\sqrt{2}mm, \qquad u_{stretch} = 40mm \ \ (19\%\ stretch)$$

The amplitude of stretch along the bisector of the lattice beam fibers is varied according to the small and large deformation tests. For the geometric linear and nonlinear analysis of 3D pantographic lattice, the stretch is varied from 0.33% to 19% to observe the response of the lattice joints via beam strain energy distribution contour plots.

In summary, each pivot in the 3D lattice is constituted by 3 coincident nodes from different combinations of fiber pairs. A pivot is attributed by 18 degrees of freedom, 6 from each node; 3 translational, and 3 rotational degrees of freedom. The translatory degrees of freedom are rigidly connected in the global coordinate system while beam bending rotational degrees of freedom are connected by pivots with torsional springs. For unique solutions to the 3D pantographic model, rotational degrees of freedom, about the

beam fiber axis, are set to zero. The remaining 6 rotational degrees of freedom are connected by 3 spring pairs at the 3 nodes at the beam intersection.

5.4 Numerical Results

5.4.1 Linear Torsional Spring

A bias extension test is performed for the 3D pantographic lattice to observe the deformations for small and large displacement loads. The results are presented as strain energy distribution contours for the linear model in Figure 5-8. The side view enables observation of the strain energy distribution along the edges of the lattice.

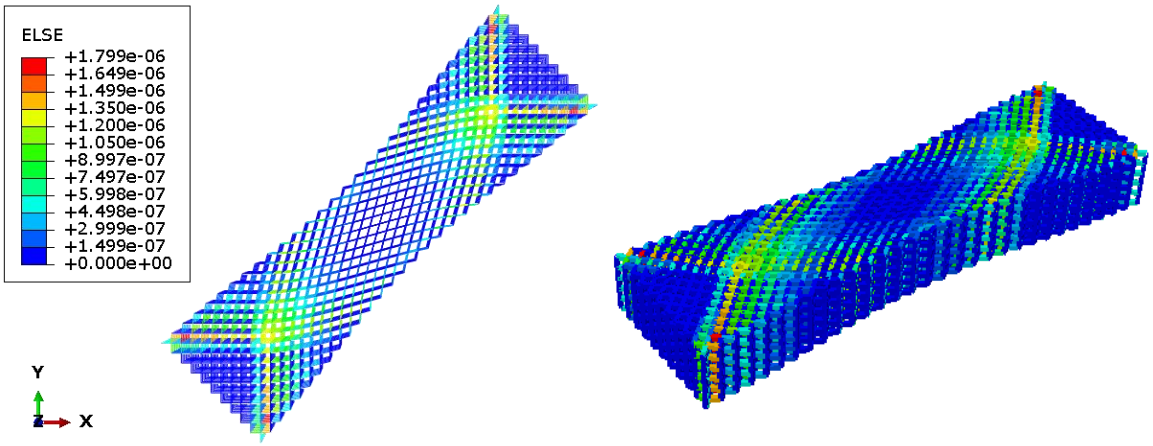

(a) Case 1, $k_\theta \to 0$

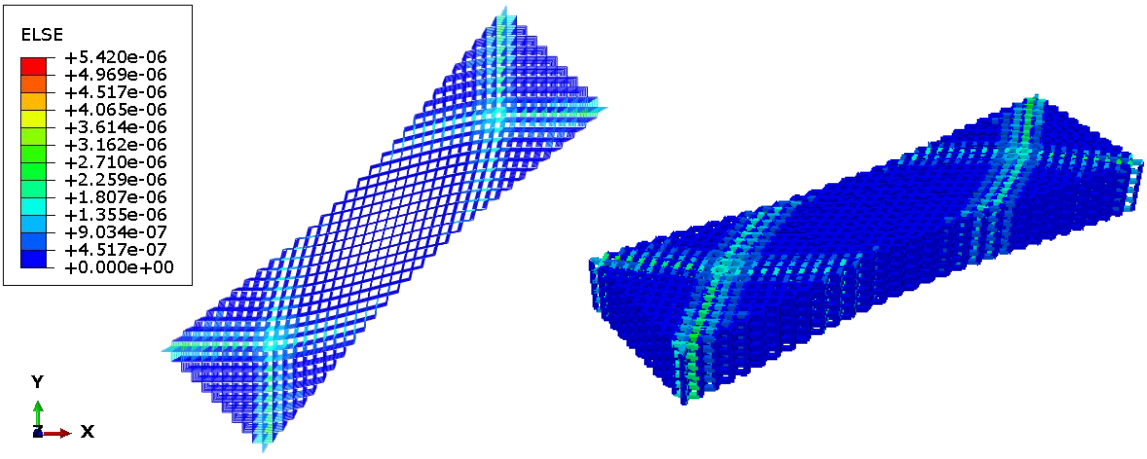

(b) Case 2, K* =0.1

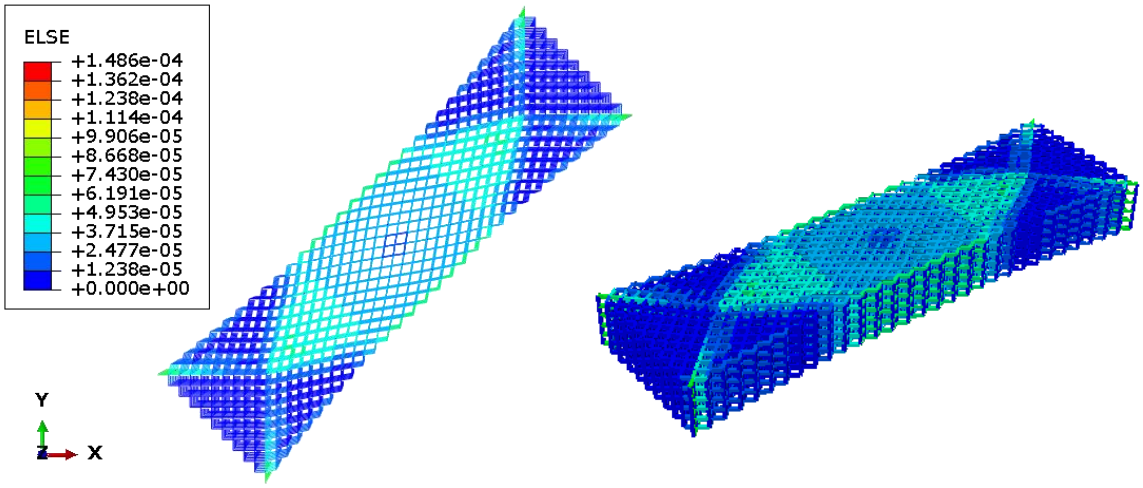

(c) Case 3, K* =0.1

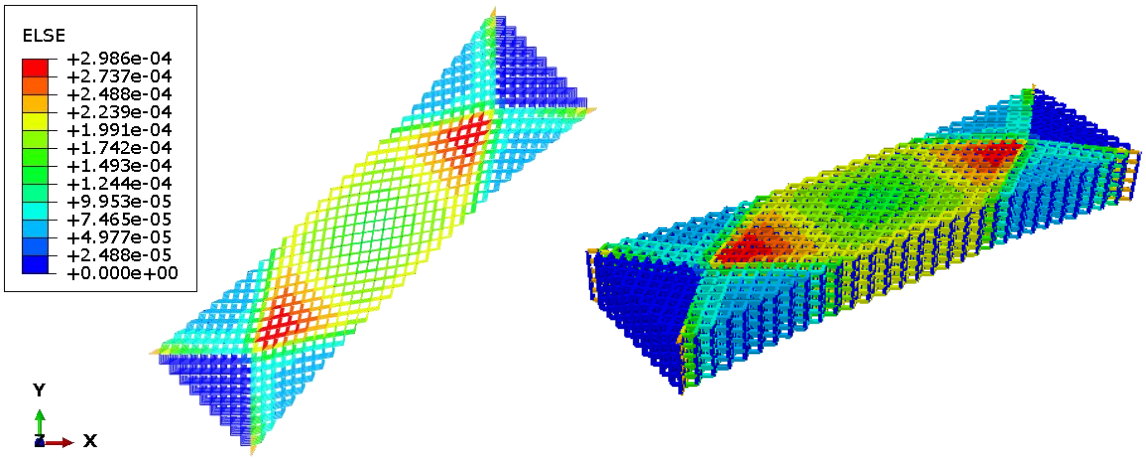

(d) Case 4, $k_\theta \to \infty$

Figure 5-8 Total Strain Energy distribution for varying orders of torsional stiffness at pivots for small lattice stretch (0.33%), linear geometry

The strain energy distribution is similar to the results obtained for the 2D pantographic lattice. However, the total strain energy for the combined six-layered 3D lattice model with the same load as applied in 2D is lower for all orders of torsional resistance, indicating the 3D pantographic lattice has a global stiffness smaller than the

corresponding 2D lattice when the same beam parameters are used, refer Table 4. The behavior is observed for all ranges of lattice stretch studied in this research. Figure 5-9 illustrates one such case with the development of reaction force for Case 2 for the 2D and the 3D model with small lattice stretch. The larger slope of the curve for the reaction force for the 2D model suggests larger global stiffness.

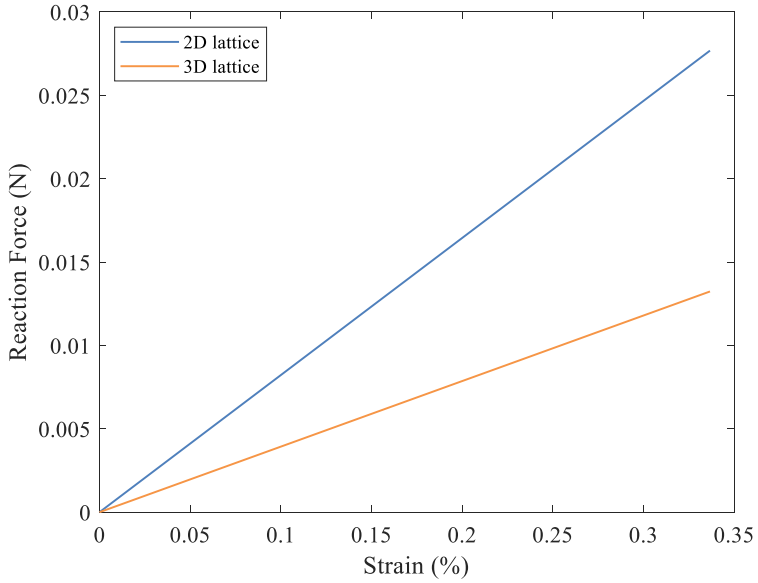

Figure 5-9 Comparison of Reaction Force vs lattice stretch for with linear torsional springs for Case 2 with $K^* = 0.1$ (small stretch, 0.33%)

Figure 5-8c shows that for Case 3 the beam strain is concentrated within local bands of the lattice. Unlike the 2D model, the low-energy region present in the center of the lattice has grown proportionately very small. When $k_\theta \to \infty$, the 2D pantographic model reflects rigid pivots, however, as discussed in Section 5.3, Case 4 does not represent a rigid connection for the 3D pantographic lattice model. The difference is small, attributed mostly to the negligible beam twist energy in the 3D pantographic lattice compared to the 3D rigid connection lattice which includes beam twist energy.

For small strain, the linear model is sufficiently accurate compared with the model that accounts for nonlinear strains, as can be observed from Table 4. The relative difference is significantly less considering nonlinear models are computationally expensive. The total strain energy attributed to twisting deformation in a rigid model is comparatively very less.

Table 4 Total Strain Energy comparison for the linear and nonlinear geometric model for small stretch (0.33%)

Case	Total Strain Energy (mJ)		Relative Difference (%)
	Linear Geometry	Nonlinear Geometry	
1	0.002513	0.002528	0.593
2	0.010333	0.01039	0.548
3	0.410627	0.412675	0.496
4	0.985433	0.99086	0.547
Rigid	0.985434	0.990861	0.547

The bias extension test is extended to large strain with the respective strain energy distribution is presented in Figure 5-9. The nonlinear model for all the cases shows very high necking particularly around the middle of the lattice. Figure 5.9c shows a high strain at the corner elements of the lattice visible in the nonlinearly deformed model. In Figure 5.9d, the nonlinearly deformed lattice is relived of the high strain regions that are dominant in the linear pantographic model.

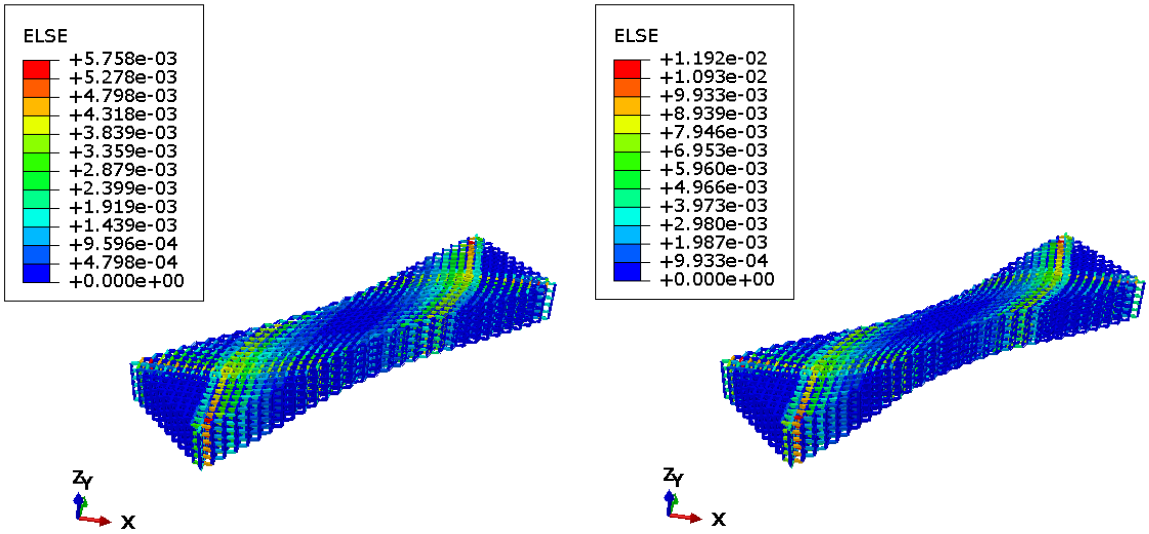

(a) Case 1, $k_\theta \to 0$, Linear Geometry vs Nonlinear Geometry

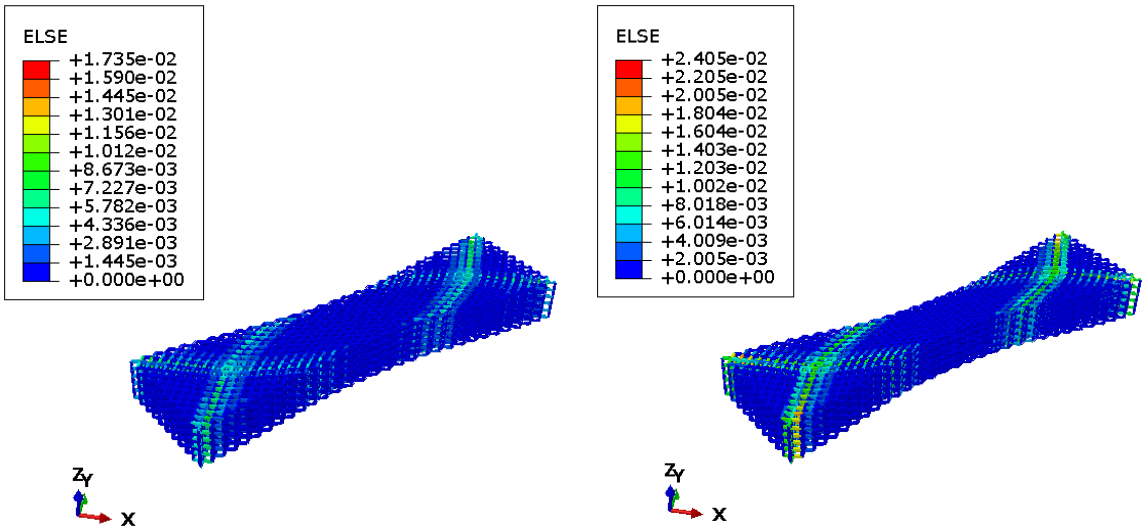

(b) Case 2, K* =0.1, Linear Geometry vs Nonlinear Geometry

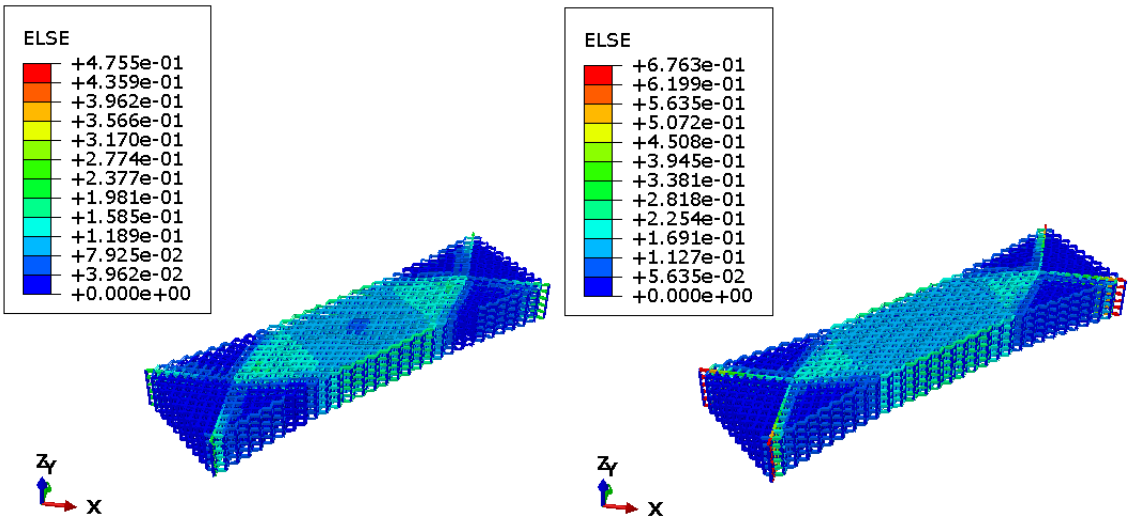

(c) Case 3, K* =0.1, Linear Geometry vs Nonlinear Geometry

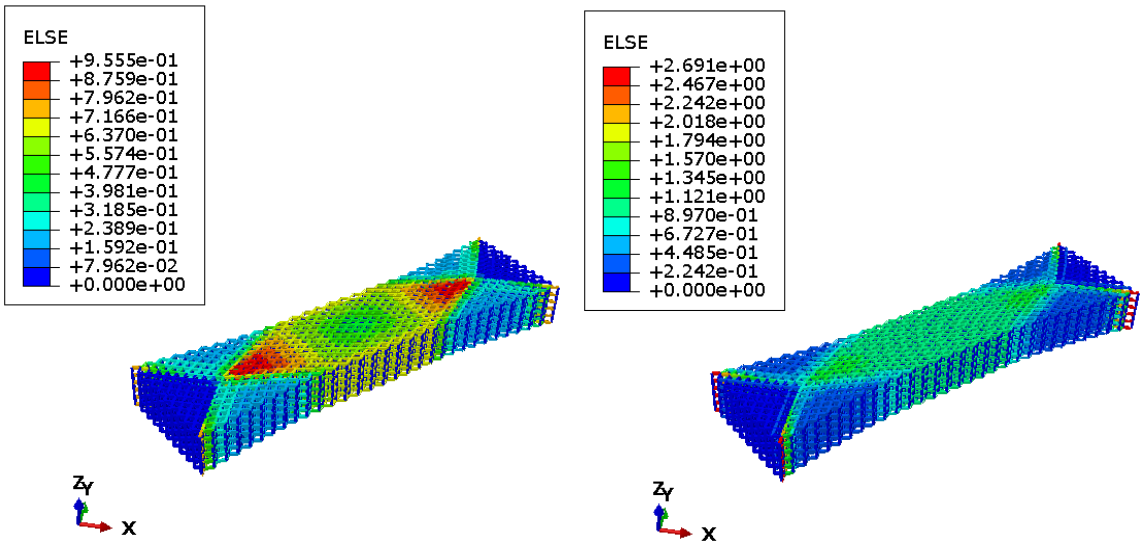

(d) Case 4, $k_\theta \rightarrow \infty$, Linear Geometry vs Nonlinear Geometry

Figure 5-10 Total Strain Energy distribution for varying orders of torsional stiffness at pivots for large lattice stretch (19%)

The total strain energy for the large strain model is presented in Table 5. The total strain energy obtained for Case 4 corresponds up to two decimal places for the rigid 3D pantographic model. The difference can be attributed to the small twisting deformation energy in the rigid model. Similarly, the difference obtained in the strain energy distribution for the rigid pivots and Case 4 model is negligible.

Table 5 Total Strain Energy comparison for the linear and nonlinear geometric model for large deformations (19%)

Case	**Total Strain Energy (mJ)**	
	Linear Geometry	**Nonlinear Geometry**
1	8.042334	13.98481
2	33.06401	54.47921
3	1313.98	1977.69
4	3153.327	5187.027
Rigid	3153.33	5187.03

Figure 5-10 shows the total strain energy against the lattice stretch for the linear and nonlinear geometric model. For small orders of torsional resistance, the relative difference between the total strain energy for the linear and nonlinear model is largest for Case 1 which represents lattice pivots with zero torsional resistance. The total strain energy for linear and nonlinear geometry varies by more than 3% even for lattice stretch as small as 3% signifying the importance of studying the more accurate nonlinear geometry models.

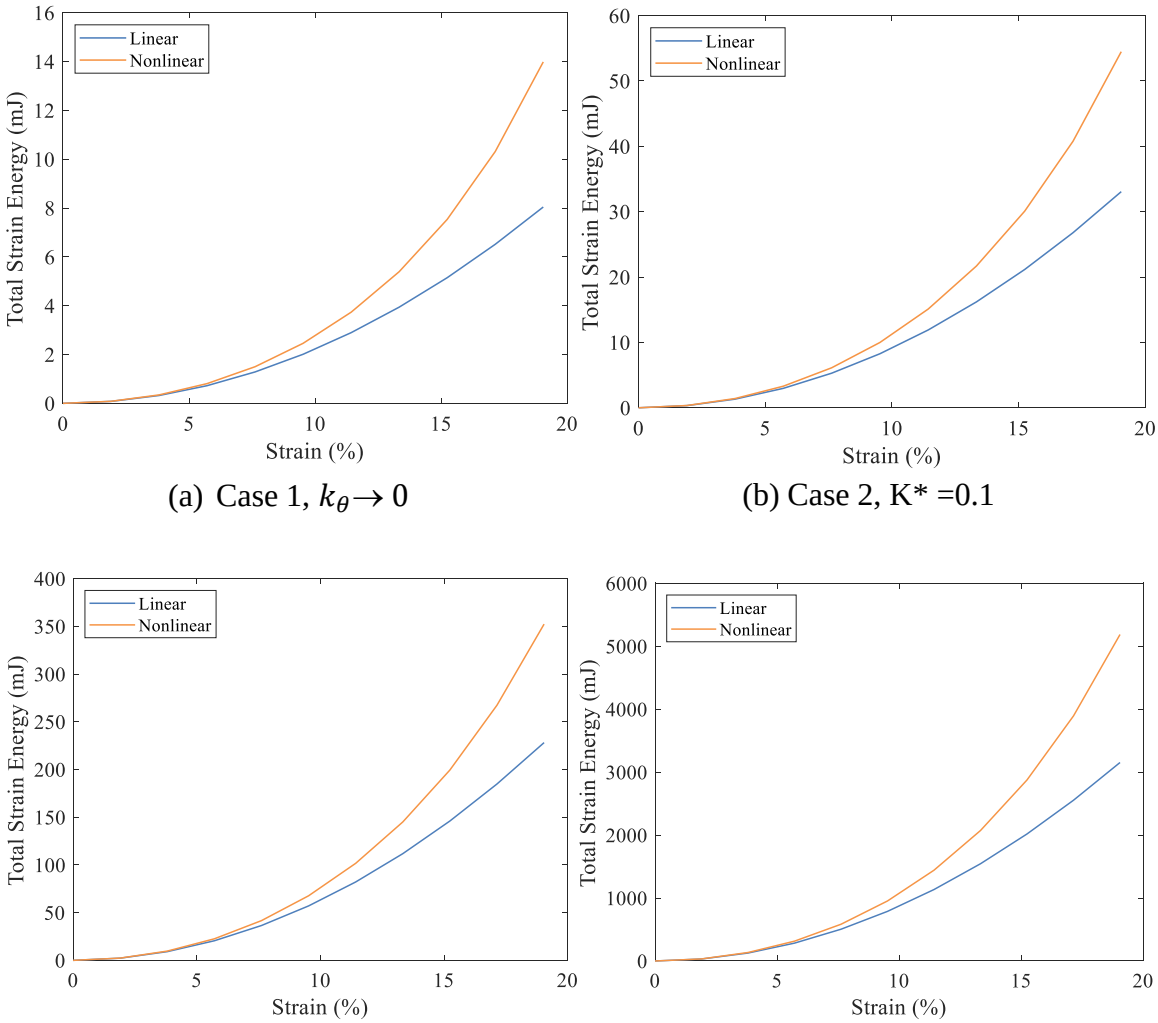

(a) Case 1, $k_\theta \to 0$

(b) Case 2, K* =0.1

(c) Case 3, K* =0.1

(d) Case 4, $k_\theta \to \infty$

Figure 5-11 Total Strain Energy vs lattice stretch for varying orders of nonlinear torsional stiffness at pivots for large deformation load (19%)

5.4.2 Nonlinear Torsional Spring

A nonlinear torsional spring is implemented similar to one utilized in the 2D pantographic model. The results are presented for a large lattice stretch of 19%. Figures below compare the total strain energy vs lattice stretch for linear and nonlinear geometry models. The β^* is ranged from -0.001 to 0.001. The results are presented for the softening and stiffening of the lattice and compared with a constant torsional spring model. The difference in total strain energy widens for the nonlinear geometry model. Similar behavior is also observed in the 2D nonlinear geometry-lattice model.

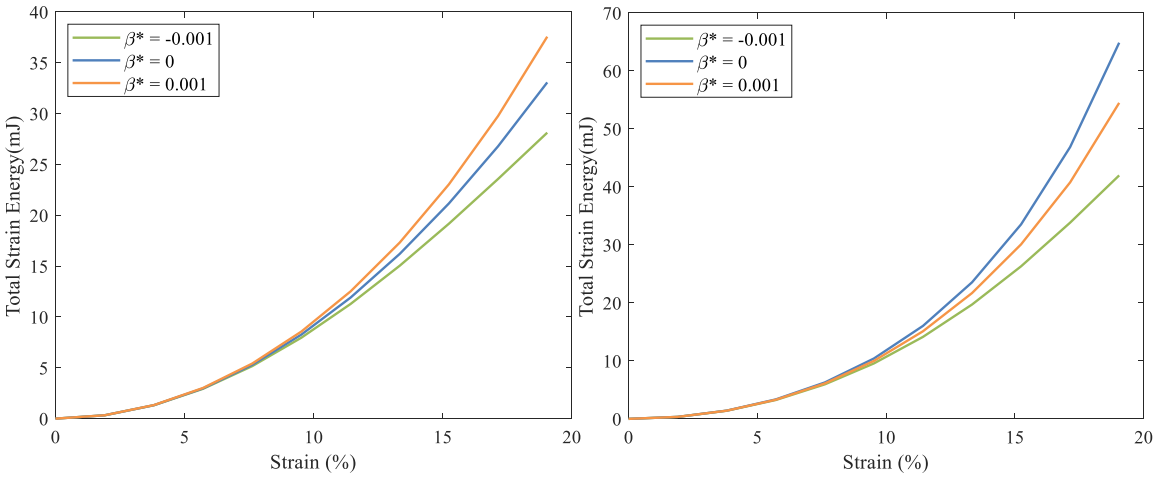

Figure 5-12 Total Strain Energy vs lattice stretch for Case 2 K=0.1, linear(left) vs nonlinear geometry(right), large lattice stretch (19%)*

The reaction force for both linear and nonlinear geometry model flattens for the softening torsional spring model as observed in Figure 5-13.

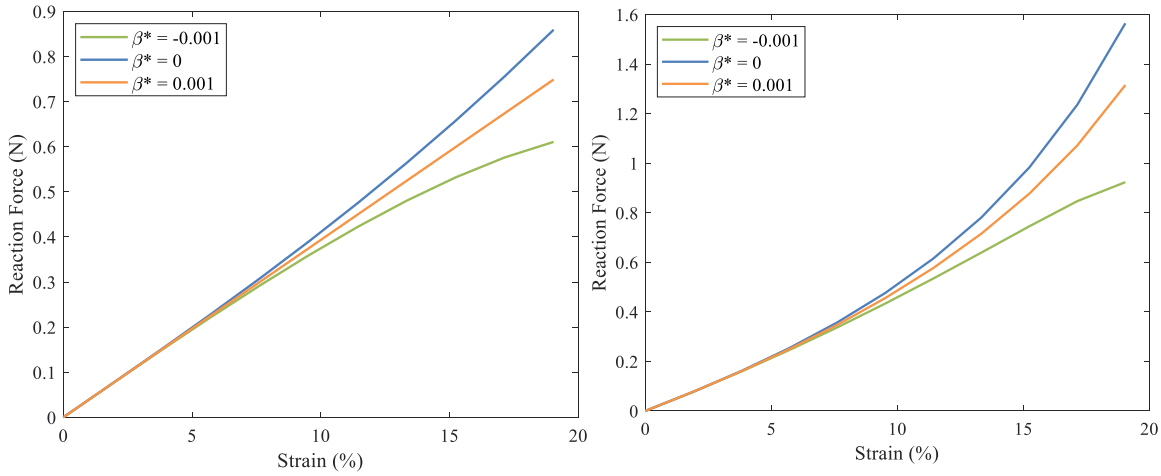

Figure 5-13 Comparison of Reaction Force vs lattice stretch Case 2 K=0.1, linear (left) vs nonlinear geometry (right) with large lattice stretch, (19%)*

For Case 3 order of torsional stiffness, the total strain energy is close-knit for both softening and stiffening cases. The reaction forces for the Case 3 model are larger compared to Case 2 for both linear and nonlinear geometry.

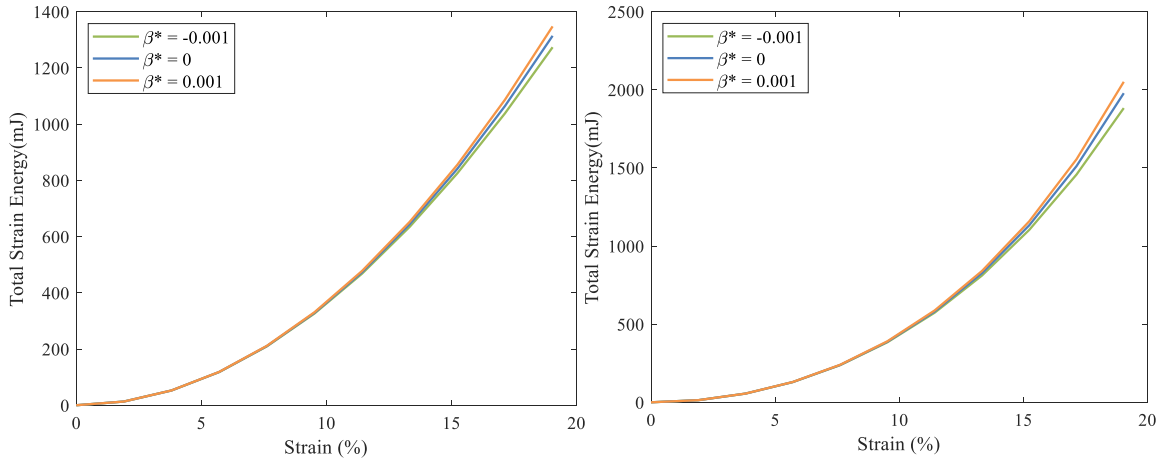

Figure 5-14 Total Strain Energy vs lattice stretch for Case 3 K=0.1, linear(left) vs nonlinear geometry(right), large lattice stretch (19%)*

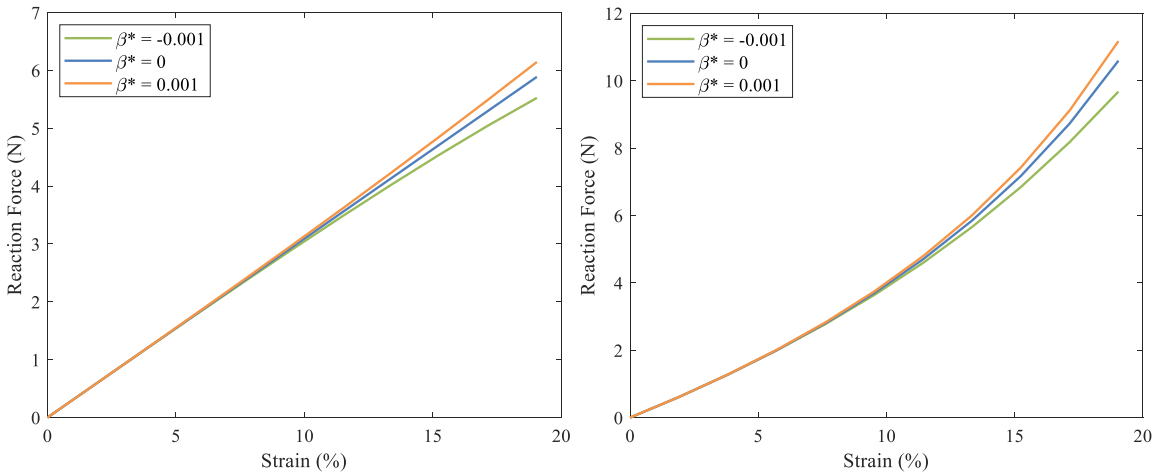

Figure 5-15 Comparison of Reaction Force vs lattice stretch Case 3 K=0.1, linear (left) vs nonlinear geometry (right) with large lattice stretch, (19%)*

Unlike Case 2, the reaction forces at higher orders of torsional stiffness do not vary with softening or stiffening of the lattice as can be observed in Figure 5-15. The amplitude flattening observed for the Case 2 softening model is also absent for Case 3.

The strain energy distribution presented in Figures 5-16 and 5-17 shows the prevalent difference in softening and stiffening cases prevalent only for high orders of torsional stiffness.

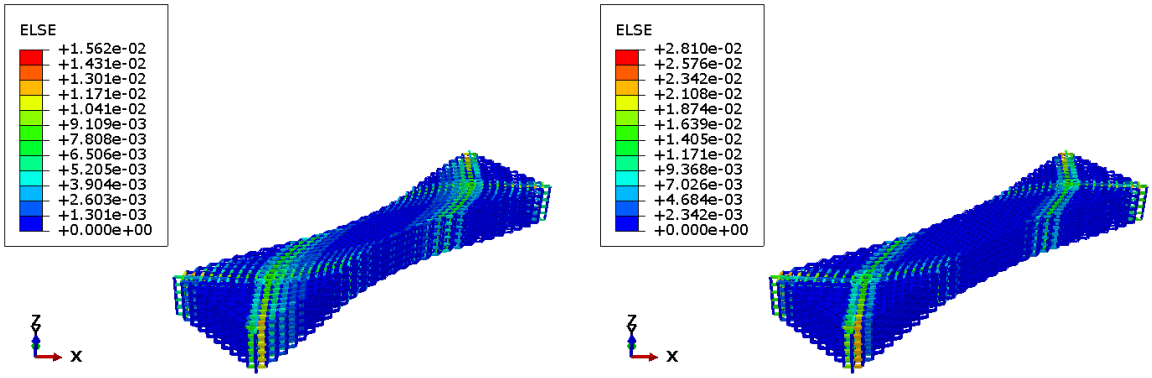

Figure 5-156 Total Strain Energy distribution for nonlinear geometry Case 2 model with large lattice stretch (19%), $\beta^* = -0.001$ (left) vs $\beta^* = 0.001$ (right)

The high strain energy is also more varied in Case 3 around the center of the lattice where necking is more prevalent. In Case 2, the distribution of strain energy is more uniform around the center.

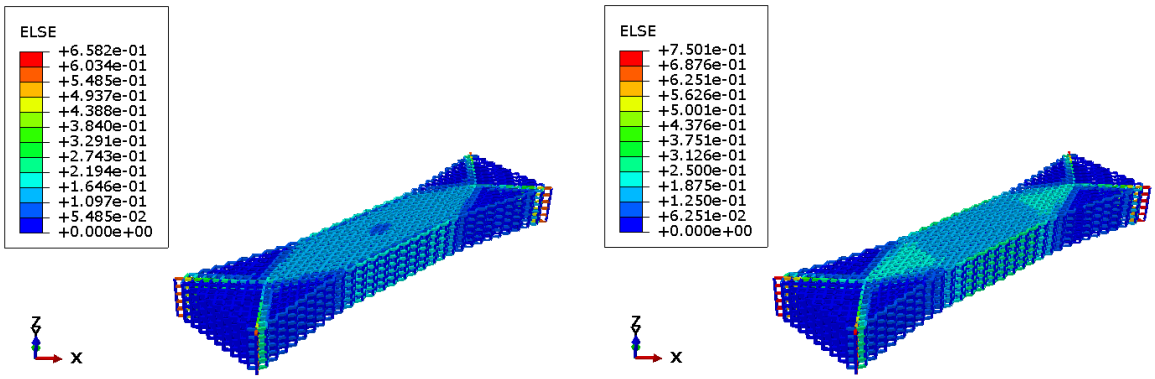

Figure 5-16 Total Strain Energy distribution for nonlinear geometry Case 3 model with large lattice stretch (19%), $\beta^* = -0.001$ (left) vs $\beta^* = 0.001$ (right)

Chapter 6 Conclusion

Discrete finite element frame models of pantographic lattice are developed in MATLAB and Abaqus Standard. The beam model developed in this study validates the homogenized continuum model developed by [8] for torsional springs exhibiting linear behavior undergoing small strains. The parametric study is automated using Python to obtain better computation performance. Different order of torsional stiffness at the lattice pivots are defined relative to the beam length and section properties in relation with a small scaling parameter ε defined as the ratio of cell size to overall lattice size.

Numerical results are also presented for standard elongation tests performed for different orders of torsional resistance in combination with a nonlinear geometry model using Abaqus. The tests are performed for a range of displacement loadings. The results are presented for a small lattice stretch of 0.33% and a large lattice stretch of 19%. The linear geometric model is developed in MATLAB and Abaqus for small deformation loads to validate the results presented in [8]. The results for nonlinear geometry start to show increasingly large deviations from the linear model beyond 3% lattice stretch during the elongation test. The total strain energy is found to be distributed over a wide region at the middle of the lattice as compared to localized bands of high energy as seen in the linear model. The torsional spring is also set up to reproduce nonlinear behavior at the lattice joints using the specific set of constraints available in Abaqus GUI and Abaqus Python. The resulting nonlinear stiffness is studied for both stiffenings and softening under increased deformation and also analyzed for its effects in combination with the

including of nonlinear geometry of the beam deformation. For small lattice stretch, a very small relative difference in the total strain energy is observed for both case 2 and case 3 orders of torsional stiffness. For stiffness softening, both case 2 and case 3 models show enhanced necking at the middle of the lattice. Case 3 shows a more evenly distributed strain energy for a softened lattice model. For large lattice stretch, only a small amount of softening behavior can be replicated for both cases, case 2 and case 3, due to limitations of requiring positive energy. The strain energy distribution for the nonlinear geometry with nonlinear torsional springs shows high strain energy distributed more evenly than the linear geometry model.

The research also presents an analytical model for the total strain energy for the lattice to capture the nonlinear behavior due to geometry and torsional spring introduced material nonlinearity. The model captures the small stretch nonlinear behavior and nonlinear spring as a predictive model for case 2 and case 3, however, for large stretch, this model is not accurate and cannot be used as a predictor of total lattice energy under stretch.

The 3D pantographic model is developed in Abaqus Standard to study the strain energy distribution for standard elongation tests. The model is studied for small and large deformations. All four cases of torsional resistance from the 2D analysis are carried in 3D. In order to obtain unique solutions under the constraints of three pivots for the 3 beam bending rotation pairs at the intersection of the three beams, the models set beam twisting to zero and thus do not include deformation energy in the beams due to beam torsion; however, for the orthogonal beam lattice, the energy due to local beam twist is very small compared to bending and axial strain energies. For the same elongation load

and beam profile, the total strain energy for each layer of the 3D pantographic lattice model is found to be lesser when compared to the 2D pantographic model, indicating that the in-plane global stiffness for the 3D pantographic lattice is smaller when compared to the 2D pantographic lattice. The Case 4 limit of infinite torsional stiffness at the pivot nodes is compared with a rigid connection pantographic lattice to observe the small twisting deformation energy present for the rigid lattice, not present in the pantographic model.

Based on the results obtained, some related future research is suggested:

- In the present work, the loadings are applied along the bisectors of orthogonal beam fibers. The automated python models can help toggle the in-plane directions for the boundary condition loadings. The direction and type of loadings to the beam fibers can be studied in more depth. In addition, the research only focuses on pantographic lattices with orthogonally oriented beam fibers which can be expanded to a variety of lattice cell topologies, including skewed and triangulated lattices.
- The nonlinear spring behavior at pivots presented with different strain energy distributions for the lattice can be optimized by modeling the torsional stiffness of each pivot independently.
- Design and manufacturing of pivot joints with variable torsional stiffness for experimental testing and application are needed.

- The 3D pantographic lattice model could also be introduced with nonlinear torsional springs to further investigate the behavior of the pantographic lattices under both small and large strain beam kinematic assumptions.
- Further work is needed to generalize the asymptotic homogenization models for pantographic lattice with variable pivot stiffness to include large beam kinematics in geometric nonlinear analysis and also to include nonlinear torsional springs at the pivots.
- Experimental testing is needed to help validate both the discrete frame and corresponding homogenized models for large deformation. To date, there has been no experimental testing of the 3D pantographic model.
- Comparisons of this linear material assumption with nonlinear stress-strain material for beams, such as hyper-elastic (neo-Hookean) region could be made for the case of large strain.

Chapter 7 Appendix

7.1 Strain Energy Distribution (Small Stretch, Nonlinear Geometry)

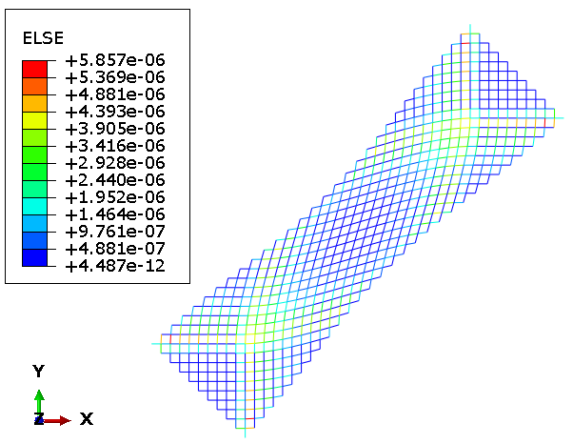

(a) Case 1, $k_\theta \to 0$

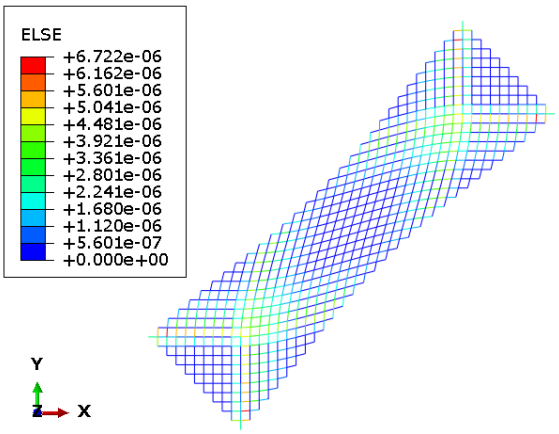

(b) Case 2, K* = 0.1

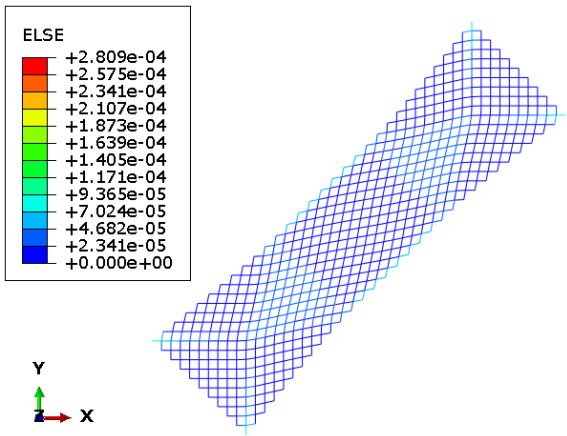

(c) Case 2, K* = 0.1

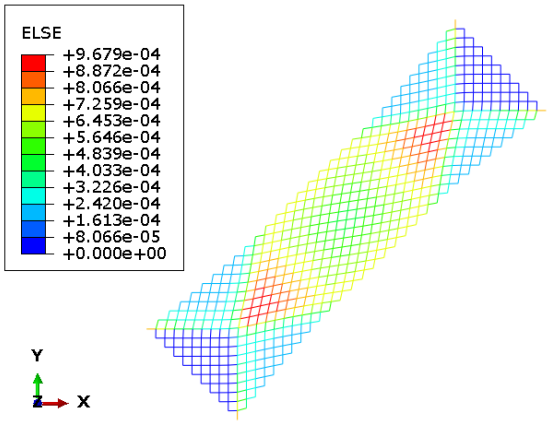

(d) Case 4, $k_\theta \to \infty$

Figure 7-1 Total Strain Energy Distribution for a small lattice stretch of 0.33% for 2D nonlinear geomtric model.

7.2 Strain Energy Distribution (Small Stretch, Linear Geometry)

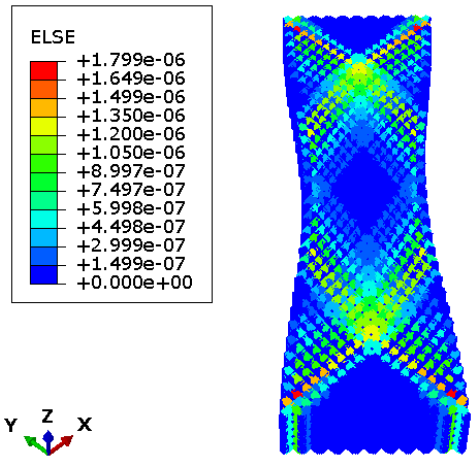

(a) Case 1, $k_\theta \to 0$

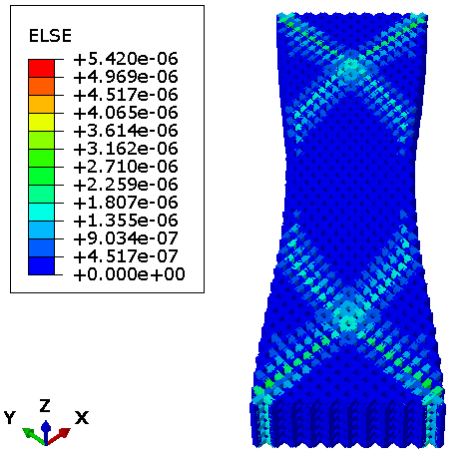

(b) Case 2, K* =0.1

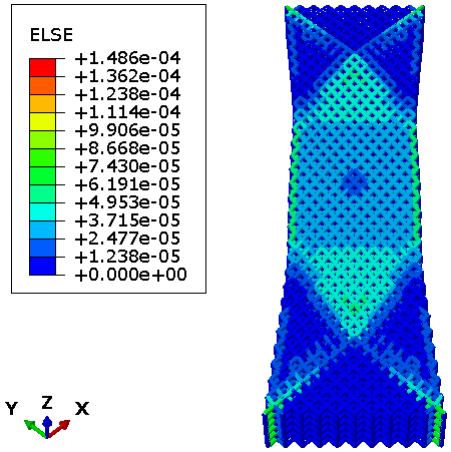

(c) Case 3, K* =0.1

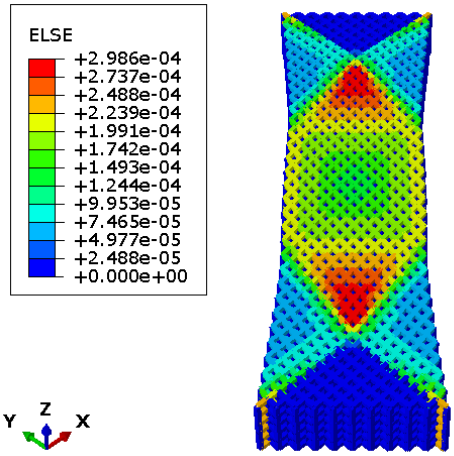

(d) Case 4, $k_\theta \to \infty$

Figure 7-2 Total Strain Energy distribution for varying orders of torsional stiffness at pivots for a small lattice stretch of 0.33% for the linear model (vertical view)

7.3 Strain Energy Distribution (Large Stretch)

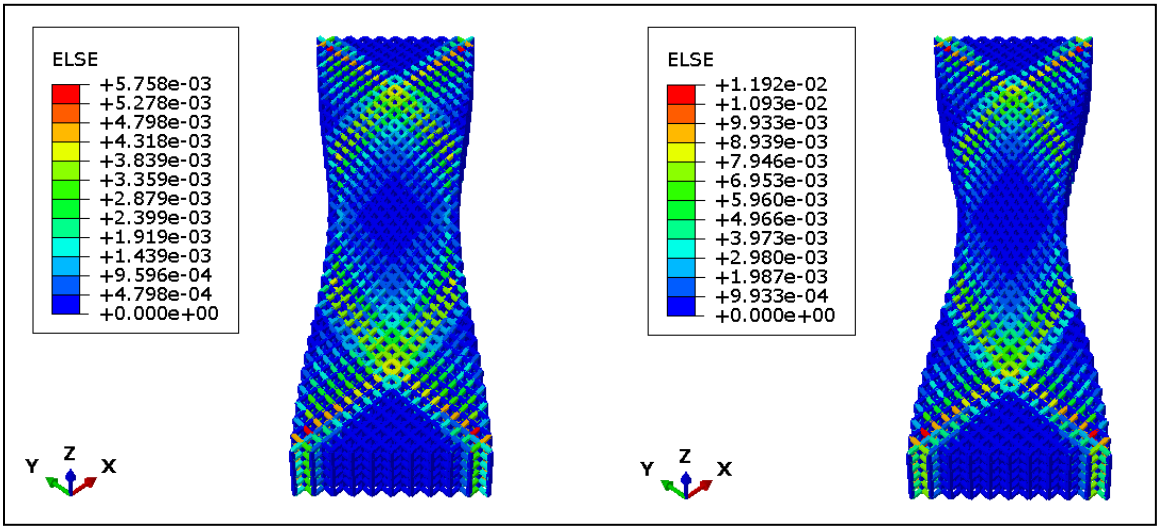

(a) Case 1, $k_\theta \rightarrow 0$

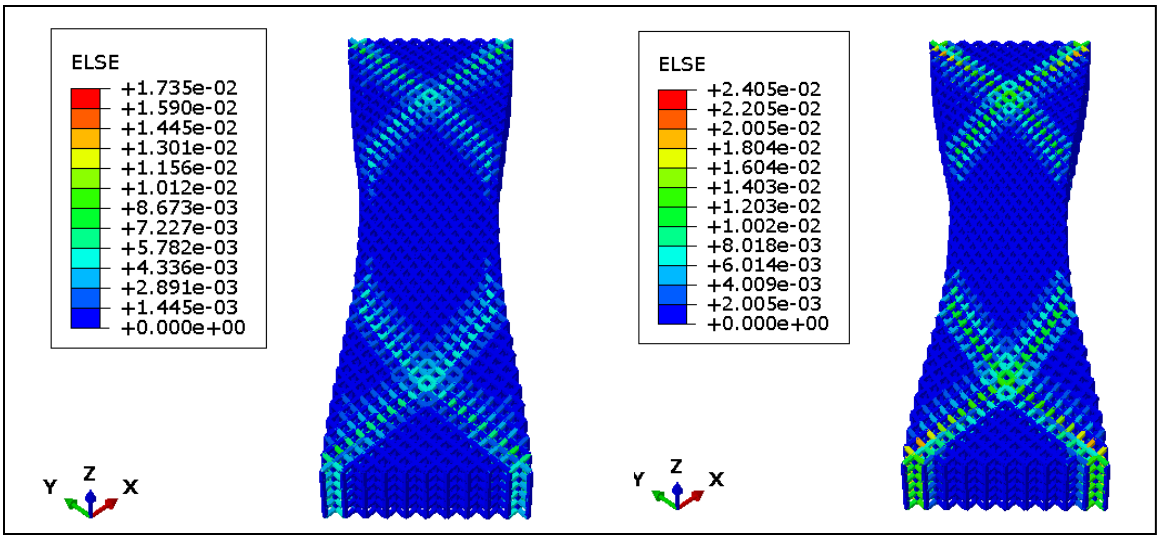

(b) Case 2, K* =0.1

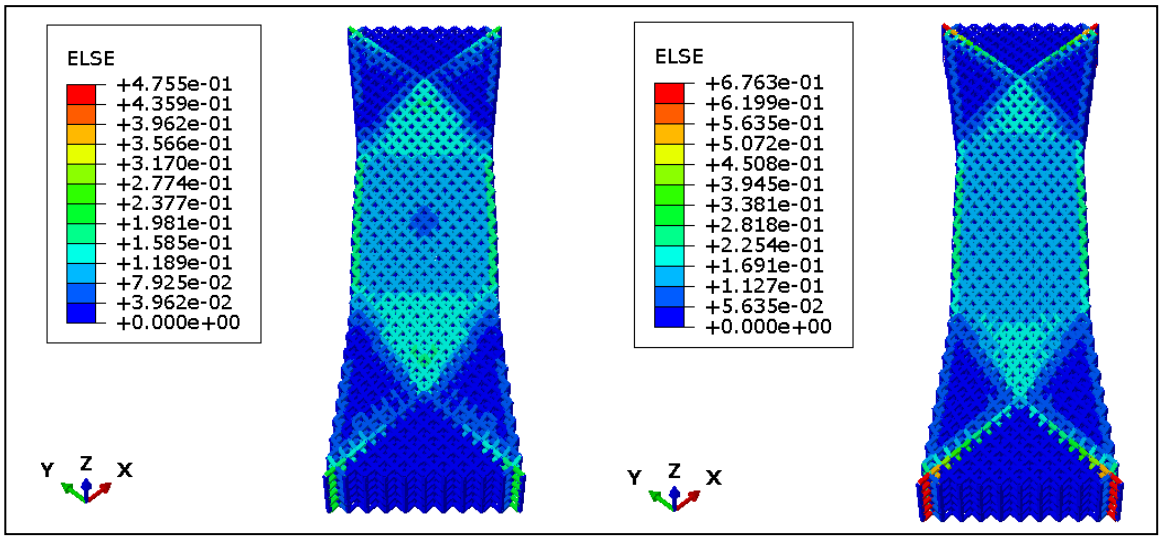

(c) Case 3, K* =0.1

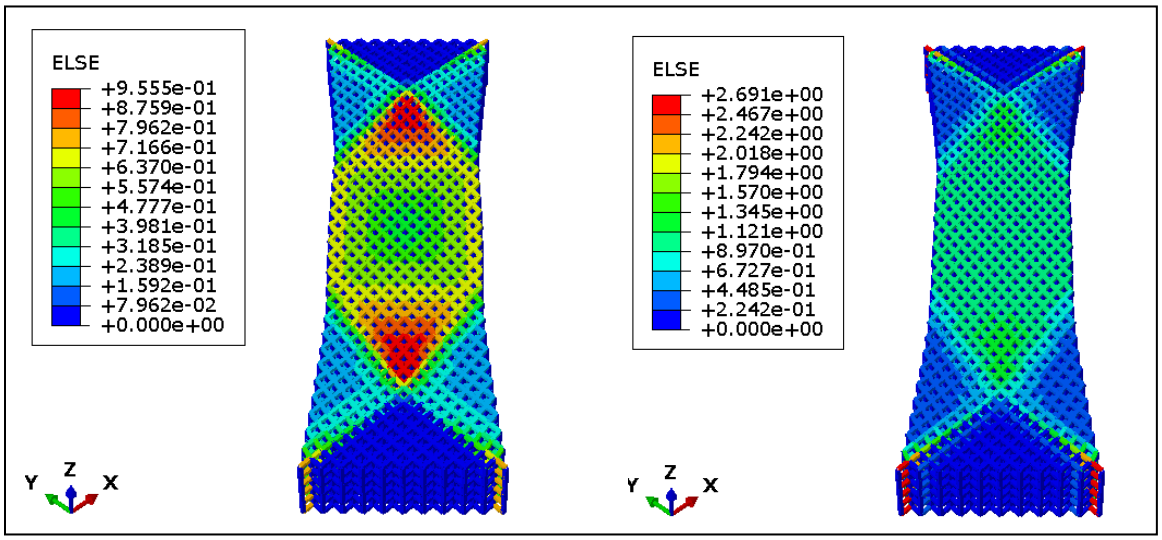

(d) Case 4, $k_\theta \rightarrow \infty$

Figure 7-3 Total Strain Energy distribution comparison for linear and nonlinear geometry model for a large lattice stretch of 19% (vertical view)

References

[1] H. Bahaloo and Y. Li, “Micropolar Modeling of Auxetic Chiral Lattices with Tunable Internal Rotation,” *J. Appl. Mech. Trans. ASME*, vol. 86, no. 4, pp. 1–11, 2019, doi: 10.1115/1.4042428.

[2] A. Bacigalupo and L. Gambarotta, “Homogenization of periodic hexa- and tetrachiral cellular solids,” *Compos. Struct.*, vol. 116, no. 1, pp. 461–476, 2014, doi: 10.1016/j.compstruct.2014.05.033.

[3] S. Hans, C. Boutin, and S. H. And, “Mechanics of Materials and Structures DYNAMICS OF DISCRETE FRAMED STRUCTURES: A UNIFIED HOMOGENIZED DESCRIPTION,” *J. Mech. Mater. Struct.*, vol. 3, no. 9, 2008.

[4] J. Ju and J. D. Summers, “Compliant hexagonal periodic lattice structures having both high shear strength and high shear strain,” *Mater. Des.*, vol. 32, no. 2, pp. 512–524, 2011, doi: 10.1016/j.matdes.2010.08.029.

[5] S. Arabnejad and D. Pasini, “Mechanical properties of lattice materials via asymptotic homogenization and comparison with alternative homogenization methods,” *Int. J. Mech. Sci.*, vol. 77, pp. 249–262, 2013, doi: 10.1016/j.ijmecsci.2013.10.003.

[6] R. S. Kumar and D. L. McDowell, “Generalized continuum modeling of 2-D periodic cellular solids,” *Int. J. Solids Struct.*, vol. 41, no. 26, pp. 7399–7422, 2004, doi: 10.1016/j.ijsolstr.2004.06.038.

[7] E. Masoumi Khalil Abad, S. Arabnejad Khanoki, and D. Pasini, “Fatigue design of lattice materials via computational mechanics: Application to lattices with smooth transitions in cell geometry,” *Int. J. Fatigue*, vol. 47, pp. 126–136, 2013, doi: 10.1016/j.ijfatigue.2012.08.003.

[8] N. Coutris, L. L. Thompson, and S. Kosaraju, “Asymptotic homogenization models for pantographic lattices with variable order rotational resistance at pivots,” *J. Mech. Phys. Solids*, vol. 134, p. 103718, 2020, doi: 10.1016/j.jmps.2019.103718.

[9] C. Boutin, F. Dell’Isola, I. Giorgio, and L. Placidi, “Linear pantographic sheets: Asymptotic micro-macro models identification,” *Math. Mech. Complex Syst.*, vol. 5, no. 2, pp. 127–162, 2017, doi: 10.2140/memocs.2017.5.127.

[10] F. Ongaro, “Estimation of the effective properties of two-dimensional cellular materials: a review,” *Theor. Appl. Mech. Lett.*, vol. 8, no. 4, pp. 209–230, 2018, doi: 10.1016/j.taml.2018.04.010.

[11] S. Liu and W. Su, “Effective couple-stress continuum model of cellular solids and size effects analysis,” *Int. J. Solids Struct.*, vol. 46, no. 14–15, pp. 2787–2799, 2009, doi: 10.1016/j.ijsolstr.2009.03.007.

[12] F. Dos Reis and J. F. Ganghoffer, “Construction of micropolar continua from the asymptotic homogenization of beam lattices,” *Comput. Struct.*, vol. 112–113, pp. 354–363, 2012, doi: 10.1016/j.compstruc.2012.08.006.

[13] H. Yang and W. H. Müller, “Size effects of mechanical metamaterials: a computational study based on a second-order asymptotic homogenization method,” *Arch. Appl. Mech.*, vol. 91, no. 3, pp. 1037–1053, 2021, doi: 10.1007/s00419-020-01808-x.

[14] R. G. Hutchinson and N. A. Fleck, “The structural performance of the periodic truss,” *J. Mech. Phys. Solids*, vol. 54, no. 4, pp. 756–782, 2006, doi: 10.1016/j.jmps.2005.10.008.

[15] G. Carta, D. J. Colquitt, A. B. Movchan, N. V. Movchan, and I. S. Jones, “Chiral flexural waves in structured plates: Directional localisation and control,” *J. Mech. Phys. Solids*, vol. 137, 2020, doi: 10.1016/j.jmps.2020.103866.

[16] S. Gonella and M. Ruzzene, “Homogenization and equivalent in-plane properties of two-dimensional periodic lattices,” *Int. J. Solids Struct.*, vol. 45, no. 10, pp. 2897–2915, 2008, doi: 10.1016/j.ijsolstr.2008.01.002.

[17] F. Dell’Isola, I. Giorgio, M. Pawlikowski, and N. L. Rizzi, “Large deformations of planar extensible beams and pantographic lattices: Heuristic homogenization, experimental and numerical examples of equilibrium,” *Proc. R. Soc. A Math. Phys. Eng. Sci.*, vol. 472, no. 2185, 2016, doi: 10.1098/rspa.2015.0790.

[18] I. Giorgio, N. L. Rizzi, and E. Turco, “Continuum modeling of pantographic sheets for out-of-plane bifurcation and vibrational analysis,” *Proc. R. Soc. A Math. Phys. Eng. Sci.*, vol. 473, no. 2207, 2017, doi: 10.1098/rspa.2017.0636.

[19] E. Turco, F. dell'Isola, A. Cazzani, and N. L. Rizzi, "Hencky-type discrete model for pantographic structures: numerical comparison with second gradient continuum models," *Zeitschrift fur Angew. Math. und Phys.*, vol. 67, no. 4, pp. 1–28, 2016, doi: 10.1007/s00033-016-0681-8.

[20] https://www.highlandwoodworking.com/woodworking-tips-1104apr/pantograph.html. Accessed: 8/20/2021

[21] S. H. Kosaraju, "Asymptotic homogenization and wave analysis of pantographic lattices with variable order rotational resistance at pivots," no. August, 2021.

[22] L. L. Thompson, *Advanced Finite Element Methods. Class Notes.* 2020.

[23] ABAQUS Documenation: Beam Element Types " https://abaqus-docs.mit.edu/2017/English/SIMACAEELMRefMap/simaelm-c-beamelem.htm.

[24] Various, "Curve Fitting Toolbox™: User's Guide," *MATLAB Man.*, pp. 1–657, 2011, [Online]. Available: papers2://publication/uuid/1AB1E427-49D2-43BA-BE5C-B64EE88F3947.